

Interparticle forces and stress transfer in saturated and unsaturated granular systems

Thesis by
Zichen Gu

In Partial Fulfillment of the Requirements for the
Degree of
Doctor of Philosophy in Mechanical Engineering

The logo for the California Institute of Technology (Caltech), featuring the word "Caltech" in a bold, orange, sans-serif font.

CALIFORNIA INSTITUTE OF TECHNOLOGY
Pasadena, California

2023
Defended April 25, 2023

© 2023

Zichen Gu

ORCID: 0000-0002-6345-0178

All rights reserved

ACKNOWLEDGEMENTS

The pursuit of a Ph.D. degree is a challenging journey that one can not accomplish alone. During the past several years, many people have supported me in my life and research. In the following several paragraphs, I will try my best to express gratitude to some of them for making this journey possible.

First and foremost, I would like to say thank you to my advisor Guruswami Ravichandran for all his support and encouragement. Ravi has always been very inspiring in our many discussions of research work. Through the two-year covid pandemic, he has been very patient and understanding while giving me a lot of freedom in doing research. I am also very grateful to my co-advisor Jose E. Andrade for all the valuable insights and suggestions. Ravi and Jose guided me in understanding the physical and mechanical nature of granular systems and helped me uncover the potential of my research. Also, I want to say thank you to Nadia Lapusta and Daniel Rittel for agreeing to serve on the committee and providing valuable feedback on my thesis.

I would like to say thank you to Kimberley Ann Mac Donald for mentoring me through the first term in the Ravichandran group. I greatly appreciate all the time and effort in teaching me the usage of experimental apparatus and the granular element method code. I also appreciate the help and guidance from Siavash Monfared. Siavash taught me a lot about the mechanics of granular systems and helped me solve several theoretical problems.

I am grateful to Jose E. Andrade, Ryan Hurley, Eloïse Marteau, and many other people for developing and modifying the granular element method. The works in this thesis would not be achieved without the novel approach they proposed. I also need to thank Petros Arakelian and Ali Kiani. Their expertise makes the one-dimensional consolidation experiments possible.

I would like to thank Kaushik Bhattacharya, Guruswami Ravichandran, and all other current and previous members of the Ravi and Kaushik research groups. The presentations, discussions, and other feedback greatly broadened my horizon of different research topics and helped me understand the underlying physics of many mechanical systems and phenomena.

I want to thank Chiara Daraio for providing me with the opportunity to study at Caltech MCE and for all the valuable guidance and suggestions. I also sincerely

appreciate Nadia Lapusta for all the help in my finding a suitable research group.

For all these years at Caltech, I have been very fortunate to be able to make friends with many great people. Thank you to Yida Li, Bowen Yang, Jagannadh Boddapati, and many others for their support and making my life at Caltech more memorable. I would like to thank Vatsa Gandhi, Prithvi Akella, John S. Weeks, and all other excellent colleagues. I also greatly appreciate the constant support from my family. I would not be able to achieve this without their understanding and encouragement.

As for funding other support, I gratefully acknowledge the funding from the Army Research Laboratory through the Multidisciplinary University Research Initiative (MURI) Grant No. W911NF-19-1-0245. Finally, I would like to thank Caltech Mechanical and Civil Engineering Department for all the resources and support they provided.

ABSTRACT

Granular systems are ubiquitous in nature and engineering applications. The macroscopic behavior of such systems is governed by the behavior at the grain-scale, including force transfer between adjacent grains. The correlation between continuum behavior and interparticle forces in granular systems is yet to be fully understood. For a saturated or unsaturated granular system under external load, it is important to decode stress partition and transfer in the solid, fluid, and gas phases. In the meantime, the presence of the fluid phase and gas phase greatly increases the difficulty of measuring interparticle forces in opaque granular systems. This thesis describes the theoretical and experimental works on interparticle forces and effective stresses in two types of granular systems: *i*) fully saturated granular media, and *ii*) unsaturated granular media.

The first part of the thesis focuses on the direct measurement of interparticle forces and the experimental validation of the concept of effective stress introduced by Karl Terzaghi. The grain-scale expression of Terzaghi's effective stress for saturated granular media under small deformation and quasi-static state is derived using stress decomposition and balance of forces and moments. For the experimental validation of the analytical solution, an experimental setup was designed to study 2D saturated rubber rod packing under classic 1D consolidation. A hybrid optical-mechanical method based on the Granular element method (GEM) and Digital image correlation (DIC) is applied. The interparticle forces are directly computed from 2D strain distribution of the grains, and the effective stress is calculated using the grain-scale forces. With pore water pressure measured by a pressure sensor, the summation of the effective stress and the pore water pressure is then compared with the external load applied in the 1D consolidation experiment, which is the core of Terzaghi's principle. The 1D consolidation experiment is also compared with the 1D consolidation model and matches the results from Discrete element simulations (DEM).

The second part of the thesis investigates the measurement of interparticle forces in more complex unsaturated granular systems consisting of solid, pore fluid, and pore air phases. In the case of quasi-static, point contact, and low saturation, an expression for the partition of stress is derived as a function of interparticle forces. To simplify the expression of the stress partition equation, capillary bridges, which are integral parts of unsaturated systems under low saturation condition, are sim-

ulated numerically using 2D finite element method (FEM) to further understand the influence of gravity on pore fluid clusters. As the original GEM for fully saturated systems focuses on interparticle interactions, the GEM is further developed for unsaturated systems based on the original GEM and considering capillary forces. Finally, a hybrid optical-mechanical approach combined with the granular element method (GEM) is developed to extract interparticle forces in a classic 1D consolidation experiment. The partition of stresses is determined by experimental results and compared with the analytical results.

The major contributions of this thesis are the theoretical derivation and experimental validation of the link between the grain-scale properties (interparticle forces, branch vectors, etc.) and the stress transfer in fully saturated and unsaturated systems. The theoretical and experimental methodology employed in the thesis could pave the way for exploring the mechanics and physics behind the constitutive behaviors of a variety of poromechanical systems.

PUBLISHED CONTENT AND CONTRIBUTIONS

- [1] Z. Gu, J.E. Andrade, and G. Ravichandran. “Interparticle forces and effective stress in unsaturated granular media”. Under preparation. 2023.
G.Z participated in the conception of the project, conducted the experiments, analyzed the data, and wrote the manuscript.
- [2] J.E. Andrade, Z. Gu, S. Monfared, K.A. Mac Donald, and G. Ravichandran. “Measuring Terzaghi’s effective stress by decoding force transmission in fluid-saturated granular media”. In: *Journal of the Mechanics and Physics of Solids* 165 (2022), p. 104912. DOI: [10.1016/j.jmps.2022.104912](https://doi.org/10.1016/j.jmps.2022.104912).
G.Z participated in the conception of the project, conducted the experiments, analyzed the data, and wrote part of the manuscript.

TABLE OF CONTENTS

Acknowledgements	iii
Abstract	v
Published Content and Contributions	vii
Table of Contents	vii
List of Illustrations	x
Nomenclature	xvi
Chapter I: Introduction	1
1.1 Motivation	1
1.2 Granular Systems	2
Saturated granular media	4
Unsaturated granular media	4
1.3 Mechanics	5
Continuum granular mechanics	6
Discrete granular mechanics	8
1.4 Numerical Simulations	9
Finite element analysis	9
Discrete element analysis	9
1.5 Experimental Methods	10
Digital image correlation	10
Granular element method	11
1.6 Thesis Outline	12
Chapter II: Measuring Terzaghi's effective stress by decoding force transmission in fluid-saturated granular media	19
Abstract	20
2.1 Introduction	21
2.2 Methods	23
Derivation of effective stress as a function of intergranular forces	24
Analytical solution of one-dimensional consolidation	29
Experimental setup for fully saturated consolidation experiments	30
2.3 Results	31
2.4 Discussion	35
Bibliography	39
Chapter III: Interparticle forces and effective stress in unsaturated granular media	42
Abstract	43
3.1 Introduction	44
3.2 Theory and Analysis	46
Effective stress in partially saturated systems	46
Numerical simulation of 2D capillary bridges	52

Granular element method for partially saturated granular media . . .	54
Theory of the classic 1D consolidation	57
3.3 Experiments	60
Experimental setup	60
Tracking and analysis of fluid clusters	62
3.4 Results and Discussion	63
3.5 Conclusion	68
Bibliography	71
Chapter IV: Summary and Future Work	74
4.1 Summary	74
4.2 Future Work	75
The effect of granular fabric on stress transfer	75
Matric suction and stress partition of granular systems with different saturation	75
Stress transfer in 3D granular systems	76
Bibliography	77
Appendix A: Results for Saturated Granular Media	78
Appendix B: Effective Modulus of Granular Assembly using Discrete Element Simulation	81

LIST OF ILLUSTRATIONS

<i>Number</i>	<i>Page</i>
1.1 Granular materials with different grain sizes, granular jamming, and granular flow. a) Concrete tetrapods in a stone dam can be considered as structured particles with a diameter near 1 m [30]. b) Sand samples with an average grain size near 1 mm [31]. c) Schematic plot of a cell cluster with the diameter of each cell near 10 μm . d) Schematic of the working principle of a jamming gripper. The red particle resembles the object being held by the jammed particles [32]. e) Numerical simulation of granular flow over a single blade. The short arrows represent the flow direction and different color shows the distribution of flow velocity [33].	3
1.2 A graphical representation of effective stress concept for saturated granular systems. The grey area represents the solid phase, and the white area represents the fluid phase.	7
1.3 Photoelastic picture of a granular assembly highlighting force chains [19].	8
1.4 The GEM methodology for inferring inter-particle forces. Experimental imaging techniques provide rich data sets for extracting intra-particle strain fields and material fabric. These ingredients are input into a mathematical framework that yields inter-particle forces by solving an inverse problem [27].	12
2.1 The Metropolitan Cathedral in Mexico City furnishes a classic example of consolidation phenomena where the effective stress plays a central role. Since the erection of the cathedral in 1573, the total stress σ from the cathedral's structure has been shifting from the pore fluid pressure P to the effective stress σ' carried by the solid skeleton. Inset shows a schematic of fully saturated granular mixture occupying a total volume V and withstanding a total stress σ which at any given time is split between the solid and the fluid phases occupying volumes V_s and V_f , respectively.	22

- 2.2 Hybrid optical-mechanical approach to establish the relation between effective stress and inter-particle forces. A) The experimental cell (quasi-2D) where a total vertical stress σ_{yy} is imposed. The drainage process is controlled via a valve and the fluid pore pressure P is measured with a pressure sensor located at the bottom right corner of the cell. B) An example of the developed force chains (black lines, whose thickness relates to magnitude and direction is coaxial to inter-particle forces) for a given configuration utilizing the Granular Element Method (GEM) based on strains obtained from Digital Image Correlation (DIC) analysis. This allows measurement of the inter-particle forces in the solid phase and, consequently, effective stress tensor via Eq. (2.15), previously inaccessible in saturated granular systems. C) Theoretical backbone of the framework linking inter-particle forces f^α , at the α -contact point, and branch vector ℓ^α to the effective stress in the solid [21], averaging over a volume V 25
- 2.3 (a) Experimental setup: 1. Loading frame, 2. Camera, 3. Fiber optic illuminator, 4. Pressure sensor, 5. Container, 6. Valve (not shown in the large picture, shown in the inset). (b) Exploded view of the container: 1. #6-32 screws and washers, 2. Window bracket, 3. Transparent window, 4. Sidewalls, 5. #10-32 screws and washers, 6. Piston chamber, 7. Piston cap, 8. Piston, 9. Box, 10. Branch tube fitting. 30

- 2.4 Experimental results with the shaded region capturing the range of results for various granular configurations. A) Evolution of total vertical stress $\bar{\sigma}_{yy}$, fluid pressure \bar{p} , and effective vertical stress $\bar{\sigma}'_{yy}$ as a function of consolidation ratio \bar{c} . In contrast to previous studies, the evolution of effective stresses is measured directly from the inter-particle forces (see Eq. (2.16) and Fig. 2.2). Shaded region of imposed stress represents standard deviation from desired stress level. B), C) Comparison between the measured pore pressure \bar{p} and the settlement s , respectively, with their counterparts of the analytical solution (Eq.(2.17) and (2.19)) as a function of the consolidation ratio \bar{c} ($E_s = 3.49$ MPa and $c_v = 304 \times 10^{-6}$ m²/s). Results serve as validation of the effective stress measurements and the experimental setup: in A) the total stress is approximately constant and additively decomposed between effective stress (measured) and pore pressure (measured); in B) the evolution of pore pressure \bar{P} measured at the bottom of the specimen corresponds to the pore pressure evaluated using Eq. (2.17); in C) the evolution of settlement measured in the specimens matches the settlement evaluated using Eq. (2.19). 33
- 2.5 Mechanism controlling the evolution of forces and effective stress with time (consolidation) in a fully saturated granular system. A) Evolution of pore pressure countered by the work rate done by the vertical forces in three different experiments. B) Scatter plot of force magnitude and contact orientation relative to the direction of load application, showing clear increases in magnitude of force as consolidation evolves, especially in the direction of loading ($\theta = 0$). 36
- 3.1 The Leaning Tower of Pisa is a world-famous tourist attraction due to its severe tilt caused by uneven settling of the building's foundation. As the weight of the tower transfers through the soil beneath it, consolidation occurs in different soil layers. The schematic of unsaturated granular soil of a total volume V and saturation S_r is shown on the right. Different from dry soil and saturated soil, the unsaturated soil layer contains both pore water (V_f) and pore air (V_a), increasing the complexity of force and stress transmission during the consolidation process. 44
- 3.2 Schematic plot of forces acting on a solid grain i in a partially saturated granular packing. 47

- 3.3 2D finite element simulation (FEM) of capillary bridges between two disks. (a) Schematic of a 2D capillary bridge between two disks. (b) FEM simulation result of the geometry of a static capillary bridge in the absence of gravity. The colormap represents the area fraction of water (red for the water phase, blue for the air phase). (c) FEM simulation result of the geometry of a static capillary bridge in the presence of gravity. (d) The average pressure difference $\bar{\Delta P} = P_a - \bar{P}_f^j$ with and without the influence of gravity as a function of normalized water volume \bar{A} . (e) The filling angle of the upper disk θ_u with and without the influence of gravity as a function of normalized water volume \bar{A} 53
- 3.4 Schematic of a soil element with volume V and length dy under 1D consolidation. 58
- 3.5 The experimental setup to validate the stress partition equation Eq. (3.10). (a) The container for partially saturated granular packing: 1. piston cap, 2. piston, 3. transparent window, 4. U-shaped sidewall, 5. support, 6. nylon screws, washers, and hex nuts. (b) EVA plastic tubing fixed in the gap on the side wall for pressurization and depressurization. (c) Pressure sensor to measure the pore air pressure. (d) CCD cameras to track the deformation of the grain skeleton and the geometry of pore water clusters. (e) Custom made valve for the depressurization process. (f) A simple illustration of the 1D consolidation experiment during which an external load σ_0 is applied to the granular system through the piston. The pore air depressurization is controlled with a custom made valve, while a pressure sensor is used to measure pore air pressure in real-time. . . . 61
- 3.6 Schematic of finding the average curvature H_f , average normal vector $\bar{\mathbf{n}}$, and fluid-gas pressure difference ΔP^β at a fluid-gas contact surface of fluid cluster ω_j 63

- 3.7 The position and geometry of water clusters, matric suction, and force chains measured in 1D consolidation experiments. (a) Water clusters (blue regions) tracked with CCD camera and the color threshold program of a granular packing at the beginning of the consolidation process, $\bar{c} = 0$, where \bar{c} is the consolidation ratio. (b) Water clusters of the same granular packing at the end of the consolidation process, $\bar{c} = 1$. (c) Average matric suction \bar{s} as a function of the consolidation ratio \bar{c} . The result is calculated from three different configurations with an average saturation S_r near 0.2. (d) Inter-particle force chains calculated using the unsaturated GEM of the same granular packing at the beginning consolidation $\bar{c} = 0$. Different colors correspond to shear strain ε_{xy}^i distribution in each particle. The black lines represent the direction and magnitude of particle-particle contact forces. (e) Inter-particle force chains calculated of the same granular packing at consolidation ratio $\bar{c} = 0.75$. (f) Inter-particle force chains of the same granular packing at the end of consolidation $\bar{c} = 1$ 65
- 3.8 The evolution of the total stress σ , the stress term related to pore air $(1 - \phi^f)P_a$, the stress term related to pore water $\phi^f P_f + W_{yy}$, and the effective stress σ' as a function of the consolidation ratio \bar{c} . The shaded area represents the standard deviation of the stress/pressure obtained from three different experiments with different configurations. The solid straight line represents the imposed stress. The results are normalized by the external load σ_0 67
- 3.9 The evolution of the normalized excess pore air pressure P_a as a function of the consolidation time \bar{t} . The shaded area represents the standard deviation of the pressure obtained from three different experiments with different configurations. The results are normalized by the external load σ_0 68
- A.1 Evolution of fluid pressure, effective stress, and their summation as a function of time for three different configurations of granular matter. Each symbol represents data gathered at a certain consolidation (time). Experimental results with the shaded region capturing the range of results for various configurations. The evolution of effective stress is calculated directly from the inter-particle forces obtained using GEM. 78

A.2	Scatter plots of force magnitude and contact orientation relative to the direction of load application for experiments 1 (A), 2 (B), and 3(C), showing clear increases in magnitude of force as consolidation evolves, especially in the direction of loading ($\theta = 0$).	79
A.3	Force percentiles and the contact percentage associated with those percentiles for experiments 1-3 (top-to-bottom). The data for each plot represents all the time-series for that experiment. For example, for experiment 3, the forces great than the 20 th percentile are carried by about 80% of the contacts.	80
B.1	An example of LS-DEM simulations (left) with the imported initial configuration from the experiment (right).	81
B.2	The axial stress σ_{yy} vs. the axial strain ε_{yy} curve for obtaining the constrained modulus ($\bar{E} = 4.062 \text{ MPa}$) for one of the configurations explored in experiments.	82

NOMENCLATURE

Abbreviations

XRD	X-ray diffraction
DEM	Discrete element method
DIC	Digital image correlation
DOF	Degree of freedom
FEM	Finite element method
GEM	Granular element method
ML	Mechanoluminescence
ROI	Region of interest
SSCC	Suction stress characteristic curve
XRCT	X-ray computed tomography

Symbols

\mathbb{C}	Material stiffness tensor
$\boldsymbol{\sigma}$	Stress tensor
$\bar{\boldsymbol{\sigma}}$	Average stress tensor
$\boldsymbol{\sigma}'$	Effective stress tensor
\boldsymbol{a}	Acceleration
\boldsymbol{b}	Body force
\boldsymbol{f}^α	Interparticle contact force
\boldsymbol{l}^α	Branch vector
$\hat{\boldsymbol{n}}$	Unit outward normal vector
\boldsymbol{t}	Traction force
\boldsymbol{v}	Velocity
\boldsymbol{x}	Position vector
$\mathbf{1}$	Identity tensor

α	Contact angle
β	Compressibility
γ	Surface tension
ϵ	One-dimensional strain
θ	Filling angle
μ	Coulomb friction coefficient
ν	Dynamic viscosity
ρ	Mass density
σ	One-dimensional stress
σ'	One-dimensional effective stress
ϕ	Porosity
ϕ^s	Solid phase volume fraction
ϕ^f	Fluid phase volume fraction
ϕ^a	Gas phase volume fraction
χ	Effective stress parameter
A	Area of a 2D system
C	Interactive constant
D	Coefficient of pore air permeability
E	Young's modulus
E_s	Constrained modulus
G	Shear modulus
H_f	Average curvature
J	Mass rate of flow
K	Bulk modulus
L	Length
M	Mass
P	Pore pressure

P^*	Equivalent pore pressure
R	Radius
R_g	Ideal gas constant
S	Surface area
S_r	Saturation
T	Temperature
V	Volume
\bar{c}	Consolidation ratio
c_v	Consolidation coefficient
k	Pore water permeability
m	Molecular weight
s	Settlement
t	Time
u	Displacement
w	Capillary bridge neck width

Chapter 1

INTRODUCTION

1.1 Motivation

Granular materials are ubiquitous in nature and are the second-most manipulated material in the industry [1]. The mechanical properties of granular materials are closely connected to various phenomena ranging from land subsidence in geophysics and planetary exploration, rotating drum mixing in the food industry, to biophysical studies of root growth in rocky soil [2–5]. While the mechanical properties of grains can be precisely measured (that of the constituent material), the assembly of grains may possess very distinct properties. With external loads being applied to a granular system, they may show exceedingly complex responses such as strong nonlinearity, loading path dependency, stress-dilatancy, grain breakage, fluidization, and jamming [6–12]. As the underlying key mechanism of all these complex behaviors originates from grain-scale features, a large number of investigations have been undertaken by different groups toward systematic examination and characterization of granular media. For example, several practical models have been reported to unravel the occurrence of jamming transition over a wide range of particle packing density [11, 12], while the effect of particle size is studied as an important factor in granular breakage [13, 14].

However, great difficulties are encountered while trying to unravel the influence of fabric (micro) structure on the constitutive behavior of granular media. Because of the complicated features at grain-scale, the mechanical behavior of granular materials strongly depend on loading conditions. Under different loading conditions, the distribution of interparticle forces (force chains) within the same material may be entirely different, which causes dramatic changes in the mechanical behavior of the granular system. While several numerical studies based on the discrete element simulation (DEM) have been conducted to explore the evolution and influence of fabric within assemblies [15, 16], systematic and quantitative experimental investigations are still lacking in studying the correlation between granular packing fabric, interparticle forces, and mechanical responses of granular material.

Moreover, in the presence of pore fluid and pore gas, the pore fluid also interacts with the grain skeleton in the form of capillary bridges, increasing the complexity

of the effect of fabric on mechanical behavior of granular systems. For example, matric suction is an important variable in soil mechanics. Although the relationship between suction stress and soil water content is well studied for a variety of granular systems [17, 18], the link between the suction stress characteristic curve (SSCC) and granular system fabric is still not well understood.

The difficulties mentioned above largely arise from the lack of proper methodologies and frameworks to experimentally measure and track interparticle forces in complex granular systems. In the past few decade, a variety of experimental methods have emerged to track particle deformation and measure interparticle forces, including photoelasticity [19, 20], X-ray computed tomography (XRCT) [21, 22], and X-ray diffraction (XRD) [23, 24]. However, all these methods have constraints in grain material type, level of saturation, number of particles, or type of force measurement. A combined methodology based on the granular element method (GEM) [25] and digital image correlation (DIC) [26] was proposed by Hurley et al. in 2014, which successfully visualized for the first time interparticle force transmission in opaque granular systems. [27] Since the granular element method was originally designed in dry granular systems, more work is needed to expand it to fully saturated and partially saturated systems to account for the presence of fluid phase.

1.2 Granular Systems

A granular system is a collection of solid macroscopic particles (grains) surrounded by other media such as fluid or gas. As shown in Fig. 1.1 a-c, the particle sizes for different granular systems may differ significantly. Typically, the particle size of granular media is larger than $100 \mu m$. At this scale, the particles are non-Brownian, and interparticle interactions are mainly friction and collision characterized by a loss of energy. Particles with diameters between $1 \mu m$ and $100 \mu m$ are denoted as powder, the behavior and motion of those particles are affected by other interactions such as Van der Waals forces and flow in the substrate [28]. Because of the interparticle friction and energy dissipation with particle motion, granular systems with different materials share some common properties. For instance, all the states of a granular system are metastable, and the sustenance of any motion of a granular system needs external energy. In this case, granular materials are sometimes defined as a state of matter [29].

The continuum behavior of granular systems highly depends on grain size, grain geometry, surface condition, material constitutive relation, packing density, and

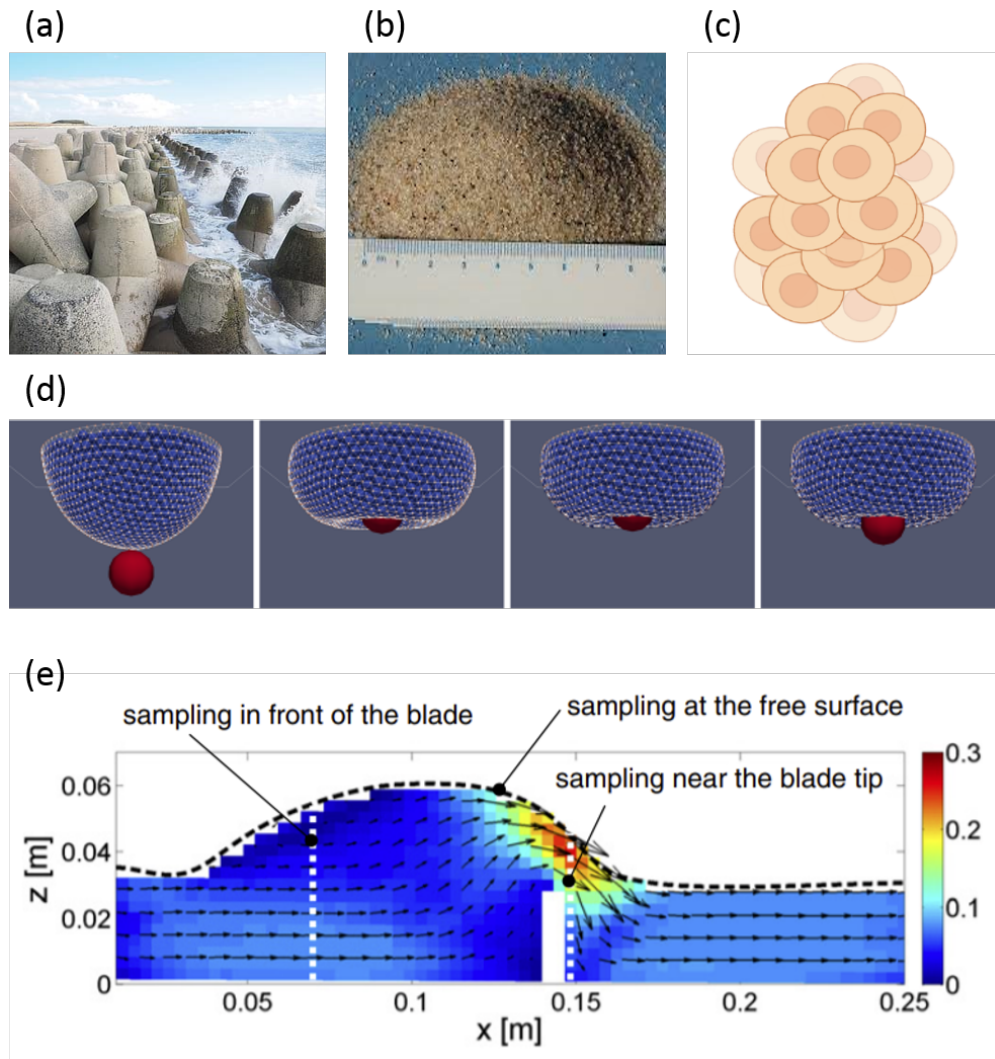


Figure 1.1: Granular materials with different grain sizes, granular jamming, and granular flow. a) Concrete tetrapods in a stone dam can be considered as structured particles with a diameter near 1 m [30]. b) Sand samples with an average grain size near 1 mm [31]. c) Schematic plot of a cell cluster with the diameter of each cell near $10 \mu\text{m}$. d) Schematic of the working principle of a jamming gripper. The red particle resembles the object being held by the jammed particles [32]. e) Numerical simulation of granular flow over a single blade. The short arrows represent the flow direction and different color shows the distribution of flow velocity [33].

configuration [11–16, 34, 35]. If a granular system is densely packed, it is considered a granular solid, which is nearly incompressible with jamming phenomenon dominating the system. On the other hand, when the grains are not densely packed, then the system is denoted as a granular liquid. If the granular system matter is dilute and dynamic, then it is called granular gas and dissipation phenomenon dominates

[28].

Inside a granular packing, a continuous pore structure forms along the grain skeleton. The continuum behavior of a granular system is also affected by the media in the pore space. Similar to porous materials, the media surrounding the granular packing can consist of both fluid (water) and gas (air) phases. The hydrostatic pressure and drag induced by flow could deform the granular skeleton. [36, 37] Depending on the degree of saturation (the fraction of fluid in the pore space), granular systems can be further divided into fully saturated, unsaturated, and dry systems.

Saturated granular media

Saturated granular media are composed of the solid phase and the pore fluid phase. With all the pore space filled with fluid, the continuum behavior of the saturated granular system is determined by the grain skeleton, the pore fluid pressure and flow. In dynamic cases, the fluid flow of saturated granular media can be considered similar to the flow through porous materials governed by Darcy's law [38]. In static cases, the change of hydrostatic pressure of pore fluid would induce deformation of the solid phase [37]. When an external load is applied to the saturated granular system, the load is balanced by stress in the solid skeleton and pore fluid pressure, which is known as Terzaghi's principle [39, 40]. Since the solid phase and fluid phase are usually assumed to be incompressible, the deformation of the granular media would occur only when drainage is allowed at the boundary of the media, which is also denoted as drainage consolidation [41].

Unsaturated granular media

Unsaturated granular media are three-phase granular materials containing solid particles, fluid (water), and gas (air). In most cases, the solid and fluid phases are assumed to be incompressible, while the gas phase is compressible. The continuum behavior of unsaturated granular systems depends on both the characteristics of the three phases and interactions between the phases. The three different types of interaction are solid-fluid, solid-gas, and fluid-gas interactions. These interactions can be static (capillary forces) or dynamic (flow). In static cases, the combined effect of the capillary forces, which relates to the degree of saturation, is directly related to changes in the volume, shear strength, and hydraulic properties of granular media [18]. As the formation of water menisci between neighboring grains produces capillary forces acting on those grains, a micromechanical framework for saturated granular soils was developed to study the hydromechanical behavior of

unsaturated granular materials [42, 43]. In this model, the capillary forces between interparticle contacts, which are assumed to depend on the degree of saturation, were integrated with the same homogenization method as for the mechanical forces. The Love–Weber formula [44] was also applied to represent the capillary forces in the form of tensor-type capillary stress.

1.3 Mechanics

The mechanical study of a granular system focuses on the balance of linear momentum, the balance of angular momentum, and the constitutive relation. The balance of linear momentum determines the translation of the object. For a deforming region Ω with volume V and surface area S , the balance of linear momentum can be written as:

$$\frac{d}{dt} \left(\int_V \rho \mathbf{v} dV \right) = \int_V \rho \mathbf{b} dV + \int_S \mathbf{t} dS \quad (1.1)$$

where ρ is the pointwise mass density in region Ω , \mathbf{v} is the velocity, \mathbf{b} is the body force, \mathbf{t} are the traction forces, and t is time. The balance of linear momentum can also be written in a differential form, which gives the equation of motion at any point in Ω ,

$$\rho \mathbf{a} = \rho \mathbf{b} + \nabla \cdot \boldsymbol{\sigma} \quad (1.2)$$

where $\boldsymbol{\sigma}$ is the stress at the point, and \mathbf{a} is the acceleration.

The balance of angular momentum governs the rotation of the subject. For the deforming region Ω , the balance of angular momentum can be written as follows:

$$\frac{d}{dt} \left(\int_V \mathbf{x} \times \rho \mathbf{v} dV \right) = \int_V \mathbf{x} \times \rho \mathbf{b} dV + \int_S \mathbf{x} \times \mathbf{t} dS \quad (1.3)$$

where \mathbf{x} is the position vector. In continuum mechanics, the balance of angular momentum also corresponds to the symmetry of the stress tensor, $\boldsymbol{\sigma}$.

Aside from the balance of linear and angular momentum, a material constitutive relation is also needed to correlate the stress and strain in the material. For the material used in the investigation of this thesis, one may assume the material of the particles is homogeneous, isotropic, and linearly elastic under small deformation.

Therefore, the constitutive relation (material stiffness matrix) of the material can be determined using two constants, namely Young's modulus and Poisson's ratio.

In the presence of pore fluid and pore gas, the interaction between different phases should also be considered. For granular systems under quasi-static conditions, the curvature fluid-gas interface (meniscus) can be determined with the Young-Laplace equation [45]:

$$\Delta P = -\gamma \nabla \cdot \hat{\mathbf{n}} = -2\gamma H_f \quad (1.4)$$

where $\Delta P = P_a - P_f$ is the pressure difference across the interface (P_a is the pore gas pressure, and P_f is the pore fluid pressure), γ is the surface tension, $\hat{\mathbf{n}}$ is the unit outward normal across the interface, H_f is the average curvature.

Continuum granular mechanics

Starting from the continuum soil mechanics, considerable effort has been made in developing continuum granular mechanics. The continuum granular mechanics models granular media as an effective media of continuous mass instead of discrete particles. Depending on packing density, granular systems may exhibit behavior of a solid or a fluid [28]. Besides, when a large load is applied to granular materials, e.g., shearing, all frictional bonds within the granular media can be broken and the material is fluidized. In this fluidized state, the grain interactions are practically instantaneous inelastic collisions. As the granular system behaves like solid before fluidization happens, this 'rapid flow state' is sometimes denoted as failure (frictional failure) of granular materials [10, 46]. In other works relating to the sustained motion of granular media, the granular media are modeled as compressible viscous (viscoelastic) fluid [47], [48].

Besides the properties of the solid grains, the fluid phase and gas phase in saturated and unsaturated granular media are also widely studied in multiphase continuum mechanics. In the early stages of soil mechanics, Terzaghi introduces an important empirical concept of effective stress for the particular case of saturated soils [40]. As shown in Fig. 1.2, with the soil being treated as continuous material consisting of solid and fluid phases, the effective stress is a combination of both the externally applied load and the internal pore pressure of fluid phase(s). In this case, a multiphase granular medium can be converted to a mechanically equivalent single-phase continuum, which can be described by a unique effective stress. For a

single incompressible fluid phase with pore pressure P_f , the effective stress tensor takes the following form:

$$\boldsymbol{\sigma}' = \boldsymbol{\sigma} - P_f \mathbf{1} \quad (1.5)$$

where $\boldsymbol{\sigma}'$ is the effective stress, $\boldsymbol{\sigma}$ is the external load applied stress and $\mathbf{1}$ is the identity tensor.

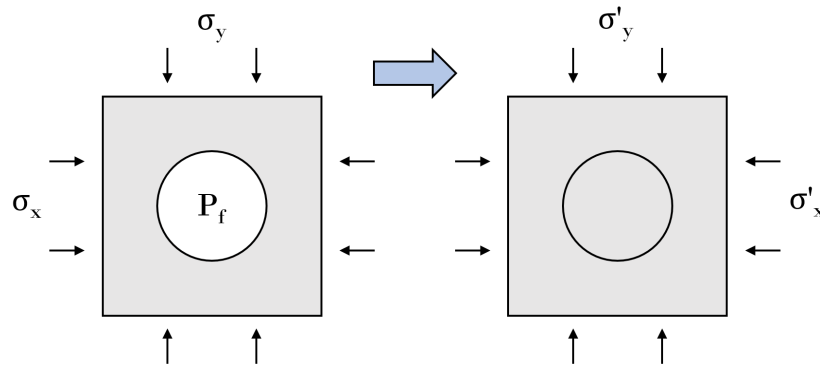


Figure 1.2: A graphical representation of effective stress concept for saturated granular systems. The grey area represents the solid phase, and the white area represents the fluid phase.

After Terzaghi's effective stress was proposed for saturated granular media, other investigations followed to expand the concept of effective stress (Eq. (1.5)) to unsaturated granular media. Among them, a well-known approach is Bishop's effective stress approach [49]. Bishop's early research states that all measurable effects related to stress change in the soil can be described through changes in effective stress. Therefore, for incompressible fluid phases with equivalent pore pressure P_f^* , the effective stress tensor takes the following form:

$$\boldsymbol{\sigma}' = \boldsymbol{\sigma} - P_f^* \mathbf{1} \quad (1.6)$$

where the equivalent pore pressure P_f^* can be considered as that portion of the effective stress resulting from the pressure of all pore fluids. Considering an unsaturated system with solid, water, and air phase, Bishop's effective stress (Eq. (1.5)) can be further written in the form:

$$\boldsymbol{\sigma}' = \boldsymbol{\sigma} - P_a \mathbf{1} + \chi(P_a - P_f) \mathbf{1} \quad (1.7)$$

where P_a is the excess pore air pressure, and χ is the effective stress parameter ranging from 0 (dry system) to 1 (fully saturated). However, the determination of the precise effective stress parameter χ is difficult, and the expression of a single effective stress may not be valid for complex granular behaviors, e.g., plastic compression in soil [50, 51]. As complex phenomena of granular systems cannot be described with a single effective stress variable, a multiple stress variable approach is induced. Theoretical approaches are proposed by Coleman [52] and experimental investigations by Fredlund and Morgenstern validate that any two of three stress state variables (σ , P_a , P_f) can be combined to define the stress state [53].

Discrete granular mechanics

While models have been developed for the stress state of granular media, experimental work is needed to unravel the relationship between stress transfer and grain-scale features as well as interparticle forces. With the development of experimental techniques, e.g., photoelasticity [19, 20] and X-ray diffraction [23, 24], the deformation of the grains in different granular systems can be directly measured or visualized. The corresponding interparticle forces induced by external loads are then calculated using the balance of momentum and material constitutive relations. As a graphical illustration, the visualization of interparticle forces (force chains) by Drescher through the photoelasticity method is shown in Fig. 1.3.

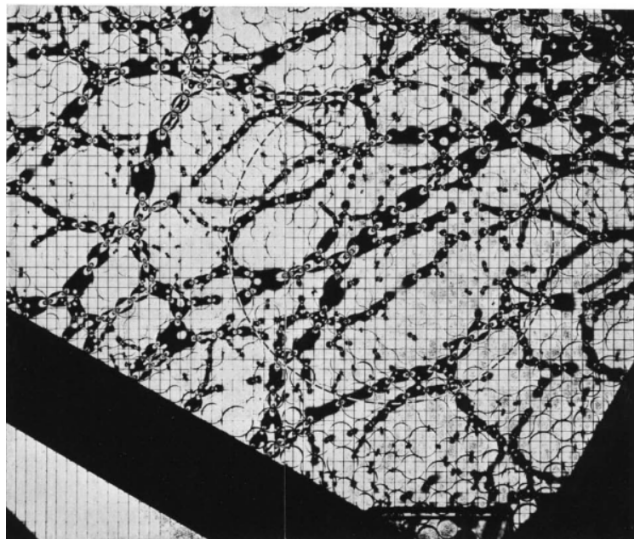


Figure 1.3: Photoelastic picture of a granular assembly highlighting force chains [19].

At the same time, efforts have been made to explore the coupling between different phases in unsaturated granular media. Farmer and Bird combine numerical and experimental approaches to characterize non-axisymmetric capillary bridges between two particles [54]. The shape of capillary bridges formed between a sphere triplet is also studied numerically and compared with experimental data [55]. However, due to increased particle numbers and complex pore structure, the direct calculation of capillary forces and interparticle forces in large granular media remains challenging.

1.4 Numerical Simulations

As a discrete system consisting of solid particles and pore fluid, numerical simulation tools are widely applied to the study of granular media. While the geometry and material properties of the grains can be modeled by various numerical methods, e.g., the level set method [56, 57], the finite element method (FEM) and discrete element method (DEM) are two of the key approaches used in the investigation of solid-fluid coupling and particle interactions.

Finite element analysis

The finite element method (FEM) is a method designed to numerically solve differential equations under certain initial and boundary conditions. To solve the problem, the FEM discretizes a large system into smaller finite elements with simple shapes by the construction of a mesh of nodes. After discretization, any function over the whole domain can be approximated as a linear combination of a series of base functions defined at each node. By introducing the weak formulation of the PDE simulated, the PDE can be simplified to an algebraic equation system. The FEM then approximates a solution by minimizing an associated error function. For an unsaturated system containing the solid phase, fluid phase, and gas phase, FEM may be applied in the study of the capillary forces and fluid meniscus geometry. In a FEM simulation of the coupling of the solid phase and fluid phases, the governing equations of the solid phase are the balance of force and momentum and the material constitutive relation, while the governing equations of the fluid phases are the continuity equation, the Navier-Stokes equations, and the total energy equation [58].

Discrete element analysis

Discrete element method (DEM) is a numerical method for computing the motion of a large number of particles. In contrast to FEM, which focuses on a continuous domain, DEM models each particle as a distinct entity and represents granular

material as an idealized assembly of particles. The overall system behavior is therefore a combined result of individual particle interactions. In a typical 3D DEM simulation, 6 degrees of freedom (DOF) (3 translation DOF and 3 rotation DOF) are considered for each particle within a granular media. The interaction force between two particles is determined by the material constitutive relation of the particles, the geometry of the particles, and the relative position and motion of the centroids of the particles. For a particle system with a given initial position and velocity, Newton's second law is used to calculate the translational and rotational accelerations at each time point, which are then numerically integrated over a time step to update particle velocities and positions [59].

1.5 Experimental Methods

Consisting of multiple phases, the characterization of material properties of granular media involves the use of multiple measurement methods, e.g., uniaxial compression test and rheology. In addition to the measurement of material properties, the measurement of interparticle forces also requires accurate image analysis techniques and corresponding computational methods. In this thesis, the granular element method (GEM) combined with the digital image correlation technique (DIC) is employed to track the deformation of each particle and calculate the interparticle contact forces.

Digital image correlation

The concept of cross-correlation has been used in data analysis for a long time, and it has been employed in digital images since the early 1970s [60, 61]. Digital image correlation (DIC) is an optical method that utilizes tracking and image registration techniques to measure the displacement and strains that occur within a region of interest (ROI) through a set of images [26].

In the application of the DIC, the deformation of a sample (granular system) is first recorded by a series of images, which are then used as inputs to a DIC program. With the grains being selected as ROI in the images, the idea is to obtain a one-to-one correspondence between points in the reference frame (initial undeformed images) and current frame (subsequent deformed images) configurations. DIC does this by taking small subsections (subsets) of the ROI in the reference image and determining their respective locations in the current configuration. To achieve this, DIC relies on finding the maximum of the correlation array between pixel intensity array subsets on the corresponding images, which generates an integer translational

shift between them. It is also possible to estimate shifts to a finer resolution than that of the original images, which is often denoted as "subpixel" registration because the measured translational shift could be smaller than an integer pixel unit. Obtaining the translational shift of each subset, the displacement information through the transformation is found by matching the location of the subset in the current configuration. For small deformations, a linear, first-order transformation is assumed at each point in the ROI. The final result is a grid containing displacement and strain information with respect to the reference configuration, also referred to as Lagrangian displacements/strains. The displacement/strain fields can then either be reduced or interpolated to form a "continuous" displacement/strain field [62].

Granular element method

The granular element method (GEM) provides a general framework to compute the interparticle forces within any granular packing given the particle location, geometry, and particle average stress. As shown in Fig. 1.4, knowing the material constitutive relation of the grains, the 2D particle average stress can be obtained through direct measurement of 2D strain field of each particle using quantitative imaging techniques such as DIC. In quasi-static cases, the interparticle forces are then computed using a series of governing equations: equilibrium of force, equilibrium of moment, equation of particle average stress, and interparticle contact constraints.

The governing equations of the GEM can also be written in matrix form, $\mathbf{K}_{eq}\mathbf{f} = 0$ (balance of forces and moments), $\mathbf{K}_{st}\mathbf{f} = \mathbf{b}_{st}$ (equation of particle average stress), and $\mathbf{B}\mathbf{f} \geq 0$ (Coulomb constraints). Since these three sets of governing equations are over-defined, the inverse problem is solved by considering the following multi-objective optimization problem subject to the Coulomb constraints.

$$\mathbf{f} = \underset{\mathbf{f}}{\operatorname{arg\,min}}(\lambda\|\mathbf{K}_{eq}\mathbf{f}\| - (1 - \lambda)\|\mathbf{K}_{st}\mathbf{f} - \mathbf{b}_{st}\|) \quad (1.8)$$

$$\mathbf{B}\mathbf{f} > 0$$

where parameter $\lambda \in (0, 1)$. The solution of interparticle forces \mathbf{f} is determined by the knee point of the Pareto front. A detailed derivation of the expression of matrix \mathbf{K}_{eq} , \mathbf{K}_{st} , and \mathbf{B} can also be found in the works by Hurley et al. [27], [63].

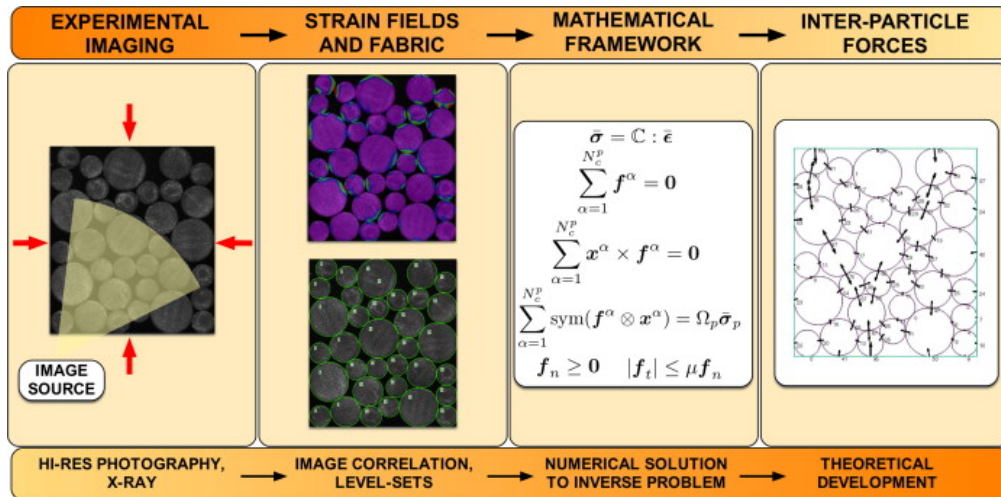


Figure 1.4: The GEM methodology for inferring inter-particle forces. Experimental imaging techniques provide rich data sets for extracting intra-particle strain fields and material fabric. These ingredients are input into a mathematical framework that yields inter-particle forces by solving an inverse problem [27].

1.6 Thesis Outline

The following chapters center on investigations of interparticle force and effective stress measurement in fully saturated and unsaturated granular systems. In each chapter, the theoretical derivation, experimental and numerical methods, and corresponding results are presented and discussed.

In Chapter 2, Terzaghi's effective stress is directly measured for the first time using interparticle forces in fully saturated granular media. The derivation of grain-scale expression of Terzaghi's effective stress is described. The analytic solutions of the pressure field and settlement of a granular system are also calculated using a 1D consolidation model. A corresponding 1D consolidation experiment is then designed to validate the results obtained from theoretical analysis. A hybrid optical-mechanical approach combined with the granular element method (GEM) for extracting particle contact forces is described in detail. The development of force chains and the partition of the total stress between the effective stress and pore fluid pressure are documented. The time evolution along with the magnitude and direction distribution of interparticle forces are further analyzed. A discrete element simulation of the 1D consolidation experiment is also carried out to compare with the experimental results.

In Chapter 3, the stress transfer in granular systems with low saturation is explored. The stress partition equation for unsaturated granular media is derived analytically

from the equilibrium of moments. The classic 1D consolidation model proposed by Fredlund and Hasan [64] is also included. To measure interparticle forces under low saturation conditions, GEM for unsaturated media is developed based on the original GEM and considering capillary forces. The hybrid optical-mechanical method and image analysis techniques necessary for the unsaturated GEM are presented. In order to examine the effect of gravity on the geometry of fluid clusters, 2D capillary bridges are investigated using finite element simulations. Through the 1D consolidation experiment, the interparticle contact forces are measured, and the stress partition equation is experimentally validated.

Finally, Chapter 4 summarized the results of the investigations of interparticle forces and effective stress in saturated and unsaturated granular media. Several possible future research directions are also presented and discussed.

BIBLIOGRAPHY

- [1] P. Richard et al. “Slow relaxation and compaction of granular systems”. In: *Nature Materials* 4.2 (2005), pp. 121–128.
- [2] C.C. Faunt, M. Sneed, and J.T. Traut and Brandt. “Water availability and land subsidence in the Central Valley, California, USA”. In: *Hydrogeology Journal* 24.3 (2016), pp. 675–684.
- [3] Y. Kim, H. Park, and S. Jeong. “Settlement Behavior of Shallow Foundations in Unsaturated Soils under Rainfall”. In: *Sustainability* 9.8 (2017), p. 1417.
- [4] M. Yamamoto, S. Ishihara, and J. Kano. “Evaluation of particle density effect for mixing behavior in a rotating drum mixer by DEM simulation”. In: *Advanced Powder Technology* 27.3 (2016), pp. 864–870.
- [5] A.M. Abdalla, D.R.P. Hettiaratchi, and A.R. Reece. “The mechanics of root growth in granular media”. In: *Journal of Agricultural Engineering Research* 14.3 (1969), pp. 236–248.
- [6] C. Liu and S.R. Nagel. “Sound in a granular material: Disorder and nonlinearity”. In: *Physical Review B* 48.21 (1993), p. 15646.
- [7] P.W. Rowe. “The stress-dilatancy relation for static equilibrium of an assembly of particles in contact”. In: *Proceedings of the Royal Society of London. Series A. Mathematical and Physical Sciences* 269.1339 (1962), pp. 500–527.
- [8] P.W. Rowe. “Theoretical meaning and observed values of deformation parameters for soil”. In: *Stress Strain Behaviour of Soils* (1971), pp. 143–194.
- [9] B.O. Hardin. “Crushing of soil particles”. In: *Journal of Geotechnical Engineering* 111.10 (1985), pp. 1177–1192.
- [10] G. Metcalfe et al. “Granular friction, Coulomb failure, and the fluid-solid transition for horizontally shaken granular materials”. In: *Physical Review E* 65.3 (2002), p. 031302.
- [11] T.S. Majmudar et al. “Jamming transition in granular systems”. In: *Physical Review Letters* 98.5 (2007), p. 058001.
- [12] A.J. Liu and S.R. Nagel. “The jamming transition and the marginally jammed solid”. In: *Annual Review of Condensed Matter Physics* 1.1 (2010), pp. 347–369.
- [13] Y.P. Cheng, M.D. Bolton, and Y. Nakata. “Crushing and plastic deformation of soils simulated using DEM”. In: *Geotechnique* 54.2 (2004), pp. 131–141.
- [14] J.D. Bono and G.R. McDowell. “Investigating the effects of particle shape on normal compression and overconsolidation using DEM”. In: *Granular Matter* 18.3 (2016), p. 55.

- [15] M. Jiang, T. Li, and Z. Shen. “Fabric rates of elliptical particle assembly in monotonic and cyclic simple shear tests: a numerical study”. In: *Granular Matter* 18 (2016), pp. 1–14.
- [16] X. Li, D. Yang, and H.S. Yu. “Macro deformation and micro structure of 3D granular assemblies subjected to rotation of principal stress axes”. In: *Granular Matter* 18 (2016), pp. 1–20.
- [17] N. Lu and D.V. Griffiths. “Profiles of steady-state suction stress in unsaturated soils”. In: *Journal of Geotechnical and Geoenvironmental Engineering* 130.10 (2004), pp. 1063–1076.
- [18] N. Lu and W.J. Likos. “Suction stress characteristic curve for unsaturated soil”. In: *Journal of Geotechnical and Geoenvironmental Engineering* 132.2 (2006), pp. 131–142.
- [19] A. Drescher and G. Jong. “Photoelastic verification of a mechanical model for the flow of a granular material”. In: *Soil Mechanics and Transport in Porous Media: Selected Works of G. de Josselin de Jong* (2006), pp. 28–43.
- [20] D. Howell, R.P. Behringer, and C. Veje. “Stress fluctuations in a 2D granular Couette experiment: a continuous transition”. In: *Physical Review Letters* 82.26 (1999), p. 5241.
- [21] P. Bésuelle et al. “X-ray micro CT for studying strain localization in clay rocks under triaxial compression”. In: *Advances in X-ray Tomography for Geomaterials* (2006), pp. 35–53.
- [22] L. Wang, J.Y. Park, and Y. Fu. “Representation of real particles for DEM simulation using X-ray tomography”. In: *Construction and Building Materials* 21.2 (2007), pp. 338–346.
- [23] H.F. Poulsen. *Three-dimensional X-ray diffraction microscopy: mapping polycrystals and their dynamics*. Vol. 205. Springer Science & Business Media, 2004.
- [24] S.A. Hall et al. “Can intergranular force transmission be identified in sand? First results of spatially-resolved neutron and X-ray diffraction”. In: *Granular Matter* 13 (2011), pp. 251–254.
- [25] J.E. Andrade et al. “Granular element method for computational particle mechanics”. In: *Computer Methods in Applied Mechanics and Engineering* 241 (2012), pp. 262–274.
- [26] H. Schreier, J.J. Orteu, and M.A. Sutton. *Image correlation for shape, motion and deformation measurements: Basic concepts, theory and applications*. Springer, 2009.
- [27] R. Hurley et al. “Extracting inter-particle forces in opaque granular materials: beyond photoelasticity”. In: *Journal of the Mechanics and Physics of Solids* 63 (2014), pp. 154–166.

- [28] J. Duran. *Sands, powders, and grains: An introduction to the physics of granular materials*. Springer Science & Business Media, 2012.
- [29] V. Garzó. *Granular Gaseous Flows*. Springer, 2019.
- [30] *Concrete tetrapods near a beach*. 2017. URL: <https://pixabay.com/photos/wave-breakwater-the-beach-fixing-2867840/>.
- [31] B Busch. #0312 *Quartz sand from race point beach*. 2013. URL: <http://www.buschgeotech.com/sand-photographs.html>.
- [32] H. Götz et al. “Soft particles reinforce robotic grippers: robotic grippers based on granular jamming of soft particles”. In: *Granular Matter* 24 (2022), pp. 1–9.
- [33] S. Radl et al. “Flow and mixing of granular material over a single blade”. In: *Powder Technology* 226 (2012), pp. 199–212.
- [34] P.A. Thompson and G.S. Grest. “Granular flow: Friction and the dilatancy transition”. In: *Physical Review Letters* 67.13 (1991), p. 1751.
- [35] M.R. Kuhn, W. Sun, and Q. Wang. “Stress-induced anisotropy in granular materials: fabric, stiffness, and permeability”. In: *Acta Geotechnica* 10 (2015), pp. 399–419.
- [36] C.W. MacMinn, E.R. Dufresne, and J.S. Wettlaufer. “Fluid-driven deformation of a soft granular material”. In: *Physical Review X* 5.1 (2015), p. 011020.
- [37] Z. Hu, Y. Zhang, and Z. Yang. “Suffusion-induced deformation and microstructural change of granular soils: a coupled CFD–DEM study”. In: *Acta Geotechnica* 14 (2019), pp. 795–814.
- [38] B.A. Bakhmeteff and N.V. Feodoroff. “Flow Through Granular Media”. In: *Journal of Applied Mechanics* 4.3 (1937), A97–A104.
- [39] K. Terzaghi. “Der grundbruch a stauwerken and seine verhiltung”. In: *Die Wasserkraft* 17 (1922), pp. 445–9.
- [40] K. Terzaghi. *Erdbaumechanik auf bodenphysikalischer Grundlage*. F. Deuticke, 1925.
- [41] M.A. Biot. “General theory of three-dimensional consolidation”. In: *Journal of Applied Physics* 12.2 (1941), pp. 155–164.
- [42] C.S. Chang and P.Y. Hicher. “An elasto-plastic model for granular materials with microstructural consideration”. In: *International Journal of Solids and Structures* 42.14 (2005), pp. 4258–4277.
- [43] P.Y. Hicher and C.S. Chang. “A microstructural elastoplastic model for unsaturated granular materials”. In: *International Journal of Solids and Structures* 44.7-8 (2007), pp. 2304–2323.
- [44] A.E.H. Love. *A treatise on the mathematical theory of elasticity*. Cambridge University Press, 1927.

- [45] T. Young. “III. An essay on the cohesion of fluids”. In: *Philosophical Transactions of the Royal Society of London* 95 (1805), pp. 65–87.
- [46] C.S. Campbell. “Rapid granular flows”. In: *Annual Review of Fluid Mechanics* 22.1 (1990), pp. 57–90.
- [47] Y.H. Wu, J.M. Hill, and A. Yu. “A finite element method for granular flow through a frictional boundary”. In: *Communications in Nonlinear Science and Numerical Simulation* 12.4 (2007), pp. 486–495.
- [48] T. Barker et al. “Well-posed continuum equations for granular flow with compressibility and μ (I)-rheology”. In: *Proceedings of the Royal Society A: Mathematical, Physical and Engineering Sciences* 473.2201 (2017), p. 20160846.
- [49] A.W. Bishop. “The principle of effective stress”. In: *Teknisk Ukeblad* 39 (1959), pp. 859–863.
- [50] J.E.B. Jennings and J.B. Burland. “Limitations to the use of effective stresses in partly saturated soils”. In: *Géotechnique* 12.2 (1962), pp. 125–144.
- [51] E.L. Matyas and H.S. Radhakrishna. “Volume change characteristics of partially saturated soils”. In: *Géotechnique* 18.4 (1968), pp. 432–448.
- [52] J.D. Coleman. “Stress strain relations for partly saturated soil”. In: *Correspondence to Geotechnique* 12.4 (1962), pp. 348–350.
- [53] D.G. Fredlund and N.R. Morgenstern. “Stress state variables for unsaturated soils”. In: *Journal of the Geotechnical Engineering Division* 103.5 (1977), pp. 447–466.
- [54] T.P. Farmer and J.C. Bird. “Asymmetric capillary bridges between contacting spheres”. In: *Journal of Colloid and Interface Science* 454 (2015), pp. 192–199.
- [55] M. Miot et al. “Numerical analysis of capillary bridges and coalescence in a triplet of spheres”. In: *Granular Matter* 23.3 (2021), p. 65.
- [56] S. Osher and R.P. Fedkiw. “Level set methods: An overview and some recent results”. In: *Journal of Computational Physics* 169.2 (2001), pp. 463–502.
- [57] R. Kawamoto et al. “All you need is shape: Predicting shear banding in sand with LS-DEM”. In: *Journal of the Mechanics and Physics of Solids* 111 (2018), pp. 375–392.
- [58] J.N. Reddy. *Introduction to the finite element method*. McGraw-Hill Education, 2019.
- [59] J. Ghaboussi and R. Barbosa. “Three-dimensional discrete element method for granular materials”. In: *International Journal for Numerical and Analytical Methods in Geomechanics* 14.7 (1990), pp. 451–472.
- [60] P.E. Anuta. “Spatial registration of multispectral and multitemporal digital imagery using fast Fourier transform techniques”. In: *IEEE Transactions on Geoscience Electronics* 8.4 (1970), pp. 353–368.

- [61] T.J. Keating, P.R. Wolf, and F.L. Scarpace. “An improved method of digital image correlation”. In: *Photogrammetric Engineering and Remote Sensing* 41.8 (1975), pp. 993–1002.
- [62] J. Blaber, B. Adair, and A. Antoniou. “Ncorr: open-source 2D digital image correlation matlab software”. In: *Experimental Mechanics* 55.6 (2015), pp. 1105–1122.
- [63] R.C. Hurley et al. “Quantifying interparticle forces and heterogeneity in 3D granular materials”. In: *Physical Review Letters* 117.9 (2016), p. 098005.
- [64] D.G. Fredlund and J.U. Hasan. “One-dimensional consolidation theory: unsaturated soils”. In: *Canadian Geotechnical Journal* 16.3 (1979), pp. 521–531.

Chapter 2

MEASURING TERZAGHI'S EFFECTIVE STRESS BY
DECODING FORCE TRANSMISSION IN FLUID-SATURATED
GRANULAR MEDIA

- [1] J.E. Andrade, Z. Gu, S. Monfared, K.A. Mac Donald, and G. Ravichandran. "Measuring Terzaghi's effective stress by decoding force transmission in fluid-saturated granular media". In: *Journal of the Mechanics and Physics of Solids* 165 (2022), p. 104912. doi: 10.1016/j.jmps.2022.104912.

ABSTRACT

Force transmission between solid and fluid phases in fluid-saturated granular systems is yet to be fully resolved. This is rooted in our inability to measure inter-particle forces in opaque systems in the presence of fluids. At the same time, the concept of effective stress was introduced by Karl Terzaghi a century ago, but this empirical approach is yet to be linked to grain-scale phenomena experimentally. To this end, we derive an expression for the effective stress based on inter-particle forces and use a hybrid optical-mechanical method to directly measure the evolution of inter-particle forces and effective stress, offering a new perspective on how forces are distributed between solid and fluid phases. While our derivation and measurement of effective stress focus on the limiting case of the Terzaghi stress, the methodology presented herein could be extended to more general situations, such as unsaturated conditions, where the micro-mechanical origin of effective stress remains elusive.

Keywords: *Terzaghi's effective stress; Saturated granular media; Contact forces*

2.1 Introduction

Capturing the mechanical coupling between solids and fluids, trapped in the interstitial spaces, is pivotal for unraveling the complex behavior of a large number of natural and anthropogenic systems ranging from earthquakes to batteries to cells [1–7]. Subsidence, a well-known phenomenon produced by depletion of underground fluids (e.g., water, oil, natural gas) [1], occurs as mass and pressure of the interstitial fluids decrease in geologic formations giving rise to inter-granular stresses driving the deformation process. Hydraulic fracturing is driven by rapid pressure increase of interstitial fluids, exploiting natural or engineered flaws that propagate into fractures within the solid rock formation [2]. In epithelial morphogenesis, cell rearrangement accompanying gastrulation is modulated by the oozing out of fluid filling the (solid) blastocoel as a result of pressure exerted by the invagination process [3]. Lithium-ion batteries undergo significant expansion of their electrode materials (e.g., graphite, silicon) during charging/discharging cycles due to intercalation of lithium ions inducing fractures in the electrode and adversely impacting electrolyte transport [4]. In earthquake nucleation models, the coupling between stresses in the solid and pore fluid pressure is central for explaining observed phenomena such as depth of large earthquakes, flash heating, and fluid-induced seismicity, among others [5–7]. For instance, Fig. 2.1 shows the classic example of consolidation of the Mexico City’s Metropolitan Cathedral, which has settled in excess of 2.4 m as the total stress σ from the weight of the cathedral structure is transferred from the interstitial fluid to the solid skeleton [8]. To this end, the effective behavior of such poromechanical systems across spatiotemporal scales depends intimately on the force transmission and evolution of stress partitioning between solid and fluid phases.

For a partially or fully saturated porous system in mechanical equilibrium, such as those mentioned above, the external load is carried by a combination of induced forces in both the solid domain (volume V_s) and fluid domain (volume V_f). However, the contribution of each phase, as a function of time, in this joint effort of maintaining mechanical equilibrium depends on a variety of factors (e.g., elasticity of the solids, viscosity of fluids, intrinsic permeability, etc.). One of the earliest attempts to explore this was in the 1920s by Karl Terzaghi, who dealt with this question in the context of clay deposits [9], much like those under the cathedral in Fig. 2.1. He introduced the concept of effective stress σ' , and defined it as the portion of the total stress σ that was carried by the solid phase or skeleton i.e.,

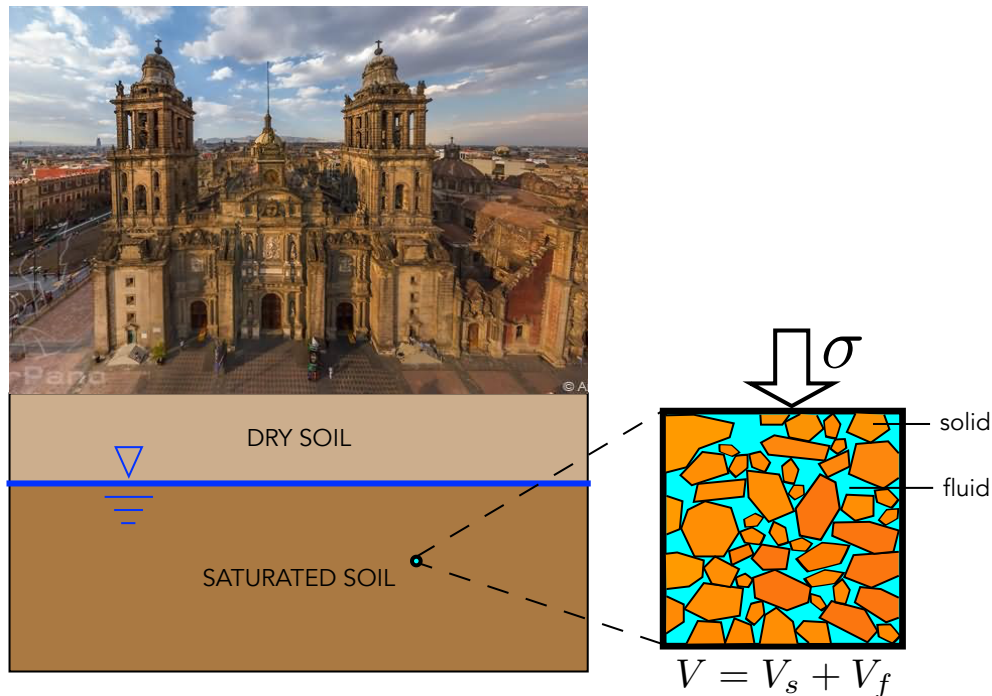


Figure 2.1: The Metropolitan Cathedral in Mexico City furnishes a classic example of consolidation phenomena where the effective stress plays a central role. Since the erection of the cathedral in 1573, the total stress σ from the cathedral's structure has been shifting from the pore fluid pressure P to the effective stress σ' carried by the solid skeleton. Inset shows a schematic of fully saturated granular mixture occupying a total volume V and withstanding a total stress σ which at any given time is split between the solid and the fluid phases occupying volumes V_s and V_f , respectively.

$$\sigma = \sigma' + P\mathbf{1} \quad (2.1)$$

with P being the pore fluid pressure and $\mathbf{1}$ signifying the identity tensor. Terzaghi's definition of effective stress is as powerful as it is simple, and intuitively connected to the balance of forces and empirical models. This gave birth to the field of soil mechanics and formed the basis for what is now known as poromechanics [10]. Over the years, significant progress has been made in capturing the physics of fluid-solid interactions induced by a variety of complex physico-chemical phenomena at the pore scale [10] by appealing to the continuum framework provided by M.A. Biot [11] and the close-to-equilibrium thermodynamic framework of irreversible deformation proposed by O. Coussy [10]. Other efforts rooted in thermodynamics have shed light on the effective stress by showing it to be stress-conjugate to the total strain

[12]. However, the concept of effective stress, at the core of all these advances and outlined applications, remains empirical and rooted in phenomenological models (e.g., the Kelvin-Voigt model) [13] shown in Fig. 2.2D. Simultaneously, significant progress has been made in granular physics, particularly in measuring inter-particle forces in dry materials [14, 15] and fully-saturated photoelastic granular systems [16, 17]. Nonetheless, the physical definition of Terzaghi’s effective stress and the measurement of inter-granular forces in opaque media and in the presence of fluids have remained elusive, hindering direct validation of the effective stress concept. Current methods indirectly *infer* the effective stress σ' by direct measurements of the total stress σ and pore fluid pressure P , and utilizing Eq. (2.1).

Our work hinges on the derivation of the grain-scale nature of Terzaghi’s effective stress and its direct measurement. As such, this work focuses on the limiting case of applicability of the Terzaghi stress to fluid-saturated solid particle mixtures, namely:

- Fully saturated, quasi-static conditions
- Incompressible solid (particles) and fluid constituents
- Solid particles with nonconforming (point) contact.

Notwithstanding these caveats, in this work we aim to answer three related, but separate fundamental questions: 1) What is the physical meaning of the effective stress σ' as defined by Terzaghi; can it be measured directly? 2) How is a macroscopic variable, e.g., σ' , related to grain-scale forces? 3) How do grain-scale forces and stresses evolve with time in fluid-saturated systems? Answering these questions is central to understanding force transmission in fluid-saturated granular systems, its relationship with effective stresses, and ultimately mechanical behavior in a range of applications such as those mentioned above.

2.2 Methods

This section summarizes three key ingredients used to directly measure Terzaghi’s effective stress σ' : i) theoretical derivation of the effective stress as a function of the intergranular forces, ii) a simple 1D consolidation model for validating the experimental setup, and iii) the experimental setup and measurements for computing the effective stress under classic 1D consolidation.

Derivation of effective stress as a function of intergranular forces

Our point of departure from the conventional approach is the well-established volume average of the stress (i.e., $\bar{\boldsymbol{\sigma}} := 1/V \int_V \boldsymbol{\sigma}(\mathbf{x}) dV$) in a fully-saturated granular system of total volume Ω as shown in the inset in Fig. 2.1. The classic additive decomposition of partial stresses states [18]:

$$\bar{\boldsymbol{\sigma}} = \bar{\boldsymbol{\sigma}}^s + \bar{\boldsymbol{\sigma}}^f \quad (2.2)$$

where each partial stress is simply the volume average of the (true) stress field in the corresponding phase occupying a volume V_s for the solid and V_f for the fluid. The additive decomposition of partial stresses is a classic result in poromechanics and does not require any phenomenological or intuitive assumptions [12, 18–20]. Further, assuming constant pore fluid pressure, one can show that $\bar{\boldsymbol{\sigma}}^f = \phi^f P \mathbf{1}$, hence:

$$\bar{\boldsymbol{\sigma}} = \bar{\boldsymbol{\sigma}}^s + \phi^f P \mathbf{1} \quad (2.3)$$

where $\phi^f := V_f/V$ is the volume fraction occupied by the fluid phase, which in the fully-saturated condition coincides with the porosity. By comparing Eq. (2.2) and the definition of effective stress given by Terzaghi in Eq. (2.1), one can obtain a relation between the effective stress and the partial solid stress, i.e., $\boldsymbol{\sigma}' = \bar{\boldsymbol{\sigma}}^s - \phi^s P \mathbf{1}$, where $\phi^s := V_s/V$ is the volume fraction of the solid and $\phi^s + \phi^f = 1$. It is important to note that this latter result is not a grain-scale definition of the effective stress and simply follows by comparison.

In order to find a physical definition of Terzaghi's effective stress $\boldsymbol{\sigma}'$, let us consider a granular medium, such as the one described at the end of the Introduction, with N solid particles, fully saturated and in equilibrium with an incompressible interstitial fluid, as shown in Fig. 2.2A, B. For particle i , conservation of Euler's linear and angular momenta yields:

$$\sum_{\alpha=1}^{N_i^c} \mathbf{f}^\alpha = \mathbf{0} \quad (2.4)$$

$$\sum_{\alpha=1}^{N_i^c} \mathbf{f}^\alpha \times \mathbf{x}^\alpha = \mathbf{0} \quad (2.5)$$

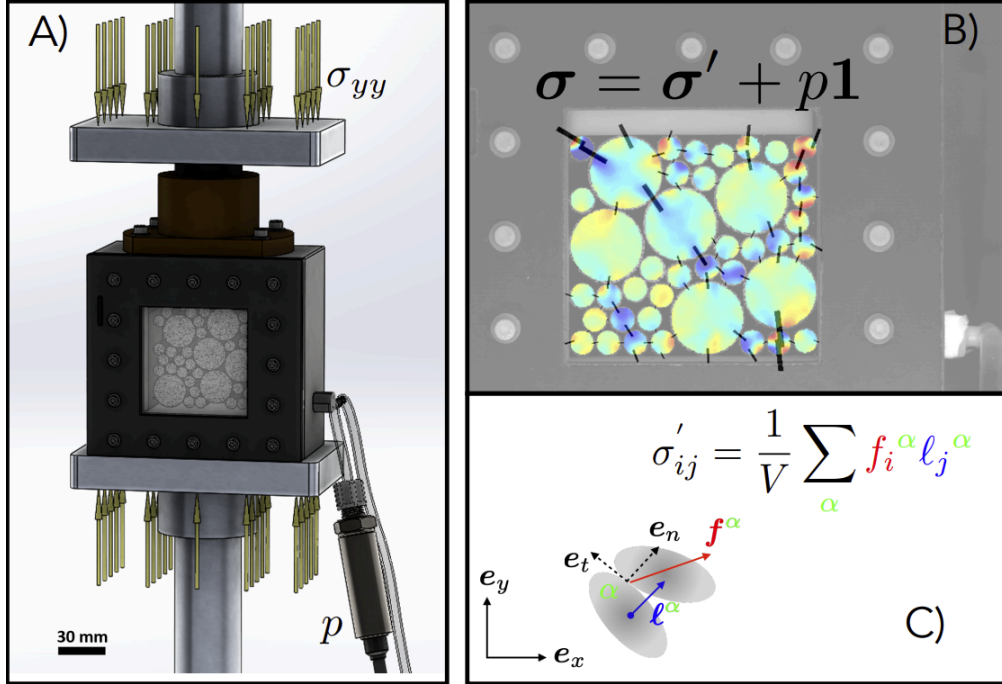


Figure 2.2: Hybrid optical-mechanical approach to establish the relation between effective stress and inter-particle forces. A) The experimental cell (quasi-2D) where a total vertical stress σ_{yy} is imposed. The drainage process is controlled via a valve and the fluid pore pressure P is measured with a pressure sensor located at the bottom right corner of the cell. B) An example of the developed force chains (black lines, whose thickness relates to magnitude and direction is coaxial to inter-particle forces) for a given configuration utilizing the Granular Element Method (GEM) based on strains obtained from Digital Image Correlation (DIC) analysis. This allows measurement of the inter-particle forces in the solid phase and, consequently, effective stress tensor via Eq. (2.15), previously inaccessible in saturated granular systems. C) Theoretical backbone of the framework linking inter-particle forces f^α , at the α -contact point, and branch vector l^α to the effective stress in the solid [21], averaging over a volume V .

where f^α is a contact (external) force at contact point x^α with N_i^c contact points acting on particle i (see Fig. 2.2C). Here we assume that the fluid is in equilibrium at a constant pore pressure P with its surface integral vanishing and not contributing to angular momentum. Similarly, (pointwise) balance of linear momentum in particle i reads:

$$\nabla \cdot \sigma_i(\mathbf{x}) = \mathbf{0} \quad \forall \mathbf{x} \in \Omega_i \quad (2.6)$$

where $\sigma_i(\mathbf{x})$ denotes the stress field in particle i with its domain delineated by Ω_i .

For a fully saturated system, composed of solid (Ω_s) and fluid (Ω_f) domains, the total average stress can be written as follows:

$$\bar{\boldsymbol{\sigma}} := \frac{1}{V} \int_V \boldsymbol{\sigma}(\mathbf{x}) \, dV; \quad \boldsymbol{\sigma}(\mathbf{x}) = \begin{cases} \boldsymbol{\sigma}_f(\mathbf{x}) & \forall \mathbf{x} \in \Omega_f \\ \boldsymbol{\sigma}_s(\mathbf{x}) & \forall \mathbf{x} \in \Omega_s \ (\Omega_i \subset \Omega_s). \end{cases} \quad (2.7)$$

We denote the (true) average stress within the solid and fluid domains as $\bar{\boldsymbol{\sigma}}_s$ and $\bar{\boldsymbol{\sigma}}_f$, respectively, and Eq. (2.7) can be written as (cf. equation (2.2)):

$$\bar{\boldsymbol{\sigma}} = \frac{1}{V} (V_s \bar{\boldsymbol{\sigma}}_s + V_f \bar{\boldsymbol{\sigma}}_f) = \phi^s \bar{\boldsymbol{\sigma}}_s + \phi^f \bar{\boldsymbol{\sigma}}_f = \bar{\boldsymbol{\sigma}}^s + \bar{\boldsymbol{\sigma}}^f \quad (2.8)$$

where V_s and V_f are the volumes of the solid and fluid phases, ϕ^s and ϕ^f are the corresponding volume fractions occupied by the two phases. The multiplication of the volume fraction and the corresponding (true) average stress is known as the partial stress, denoted as $\bar{\boldsymbol{\sigma}}^s$ and $\bar{\boldsymbol{\sigma}}^f$, respectively. In a fluid, it can be shown that $\boldsymbol{\sigma}_f(\mathbf{x}) = P(\mathbf{x})\mathbf{1}$. Also, if pore pressure $P(\mathbf{x}) = P$ (constant), the average stress of the fluid phase is:

$$\bar{\boldsymbol{\sigma}}_f = \frac{1}{V_f} \int_{V_f} P(\mathbf{x})\mathbf{1} \, dV_f = P\mathbf{1}. \quad (2.9)$$

Furthermore, the average stress of the solid phase can be expressed as:

$$\bar{\boldsymbol{\sigma}}_s = \frac{1}{V_s} \sum_{i=1}^N \int_{V_i} \boldsymbol{\sigma}_i(\mathbf{x}) \, dV_i = \frac{1}{V_s} \sum_{i=1}^N V_i \bar{\boldsymbol{\sigma}}_i \quad (2.10)$$

where V_i denotes volume associated with domain Ω_i , $\sum_{i=1}^N V_i = V_s$ and $\bar{\boldsymbol{\sigma}}_i$ represents the volume-average stress of particle i . For a discrete system in equilibrium, employing Eq. (2.6) and the divergence theorem in the expression of $\bar{\boldsymbol{\sigma}}_i$ yields [21]:

$$\begin{aligned} \bar{\boldsymbol{\sigma}}_i &= \frac{1}{V_i} \int_{S_i} \text{sym}(\mathbf{t} \otimes \mathbf{x}) \, dS_i \\ &= \frac{1}{V_i} \left\{ \sum_{\alpha=1}^{N_i^c} \text{sym}(\mathbf{f}^\alpha \otimes \mathbf{x}^\alpha) + \int_{S_i} \hat{\mathbf{n}} \cdot (P(\mathbf{x})\mathbf{1} \otimes \mathbf{x}) \, dS_i \right\} \end{aligned} \quad (2.11)$$

where \mathbf{t} is the traction at point \mathbf{x} , with $\mathbf{x} \in S_i$, and $P(\mathbf{x})$ is the pore fluid pressure acting on the surface S_i , whose point-wise normal vector is $\hat{\mathbf{n}}(\mathbf{x})$. The symbol ‘sym’

signifies the symmetric operator. We have also utilized the standard assumption that forces \mathbf{f}^α are applied pointwise at location \mathbf{x}^α , see Fig. 2.2C. Again, given a constant pore pressure $p(\mathbf{x})$, employing the divergence theorem into the fluid pressure term, the average stress $\bar{\boldsymbol{\sigma}}_i$ can be further written as:

$$\bar{\boldsymbol{\sigma}}_i = \frac{1}{V_i} \sum_{\alpha=1}^{N_i^c} \text{sym}(\mathbf{f}^\alpha \otimes \mathbf{x}^\alpha) + P\mathbf{1}. \quad (2.12)$$

Substituting equation Eq. (2.12) into (2.10), and then Eq. (2.9) and (2.10) into Eq. (2.8) leads to a new expression of the total average stress $\bar{\boldsymbol{\sigma}}$:

$$\bar{\boldsymbol{\sigma}} = \frac{1}{V} \sum_{\alpha=1}^{N^c} \text{sym}(\mathbf{f}^\alpha \otimes \boldsymbol{\ell}^\alpha) + (\phi^s + \phi^f)P\mathbf{1}. \quad (2.13)$$

where N^c is the number of contacts in the entire domain and $\boldsymbol{\ell}^\alpha$ is the branch vector connecting the centroid of the particles in contact at contact point α , as shown in Fig. 2.2C. Furthermore, $\Omega = \Omega_s \cup \Omega_f$ ($\Omega_s \cap \Omega_f = \emptyset$) constitutes the entire domain of the mixture. Additionally, partition of unity holds such that $\phi^s + \phi^f = 1$. Finally, the total average stress becomes:

$$\bar{\boldsymbol{\sigma}} = \frac{1}{V} \sum_{\alpha=1}^{N^c} \text{sym}(\mathbf{f}^\alpha \otimes \boldsymbol{\ell}^\alpha) + P\mathbf{1}. \quad (2.14)$$

Thus, the partial solid stress for a granular medium can be expressed as $\bar{\boldsymbol{\sigma}}^s = 1/V \sum_{\alpha} \mathbf{f}^\alpha \otimes \boldsymbol{\ell}^\alpha + \phi^s P\mathbf{1}$, where, as shown in Fig. 2.2, the inter-particle forces \mathbf{f}^α and branch vectors $\boldsymbol{\ell}^\alpha$ are defined at contact point α , and summed over the entire volume V . Notice there is a contribution to the partial solid stress stemming from the pore fluid pressure and scaled by the solid volume fraction $\phi^s := V_s/V$. Finally, Eq. (2.2) with the help of Eq. (2.14) can be written as:

$$\bar{\boldsymbol{\sigma}} = \underbrace{1/V \sum_{\alpha=1}^{N^c} \text{sym}(\mathbf{f}^\alpha \otimes \boldsymbol{\ell}^\alpha)}_{\bar{\boldsymbol{\sigma}}'} + P\mathbf{1} = \boldsymbol{\sigma}' + P\mathbf{1} \quad (2.15)$$

We recognize the term $\bar{\boldsymbol{\sigma}}'$ as the *drained* stress expression obtained by [21] and shown schematically in Fig. 2.2C. Also, comparing Eq. (2.15) with the Terzaghi

expression in Eq. (2.1) we can see that they are form-identical and that the effective stress

$$\boldsymbol{\sigma}' := \frac{1}{V} \sum_{\alpha=1}^{N^c} \text{sym}(\mathbf{f}^\alpha \otimes \boldsymbol{\ell}^\alpha) \quad (2.16)$$

has a clear linkage to grain-scale properties such as forces and branch vectors; an intuitive, but heretofore unproven result. For example, previous discrete element models for fluid-saturated granular media use Eq. (2.16) as the expression for effective stress [22, 23], without derivation. We exploit this linkage to measure the forces at the grain-scale in saturated granular media and thereby measure the effective stress directly for the first time, in the context of 1D consolidation, whose analytical solution is well-known.

Remark 1 *It is important to note that the expression obtained in Eq. (2.16) is form-identical to the expression obtained for the Cauchy stress for dry (drained) granular systems and derived in previous seminal contributions [21, 24]. Hence the idea of granular forces contributing to macroscopic stress is not new. However, our work adds to the previous body of work by looking into fluid saturated systems. All previous work has either focused on formal derivations of Cauchy stress for dry systems or have applied the Cauchy stress as the effective stress without justification. Notwithstanding these formalisms, the main contribution of the current work is the use of Eq. (2.16) to measure the effective stresses directly.*

Remark 2 *The assumption of constant pore pressure P is compatible with the fluid being in equilibrium. However, in the classic 1D consolidation problem shown in the next section, the pressure is homogeneous for most of the domain (cf. Eq (2.17)), except near the drainage boundary where the pressure profile drops. In the experiments described herein, the drainage valve near the bottom is not fully open, allowing for measurable, non-zero pore pressures and a quasi-homogeneous pressure profile. Therefore, the actual conditions of the experiment are somewhat in between fully homogeneous pressures and those observed in the consolidation problem. This is one possible source of error in the results shown in Fig. 2.4A, especially early on in the consolidation process when pore pressure carries the lion share of the total stress.*

Analytical solution of one-dimensional consolidation

The analytical solution corresponding to Terzaghi's one-dimensional consolidation problem [9] is well known and can be obtained by considering a porous system composed of isotropic, linear poroelastic solid and for the asymptotic case that corresponds to incompressible solids and fluids. To this end, one can solve for pressure and displacement fields. We utilize the analytical solution to validate our experimental data. The physical parameters controlling the 1D consolidation problem are the consolidation coefficient c_v and constrained modulus E_s .

Furthermore, the results can be written in dimensionless form ($\bar{t} = c_v t / (4L^2)$, $\bar{y} = y/L$):

$$P(\bar{y}, \bar{t}) = \sigma_{yy} \sum_{n \in \{2k+1 | k \in \mathbb{N}\}} \frac{4}{n\pi} \sin\left(\frac{n\pi}{2}\bar{y}\right) \exp\left(- (n\pi)^2 \bar{t}\right) \quad (2.17)$$

$$u(\bar{y}, \bar{t}) = -\frac{\sigma_{yy}}{E_s} \sum_{n \in \{2k+1 | k \in \mathbb{N}\}} \frac{8L}{(n\pi)^2} \left[\cos\left(\frac{n\pi}{2}\bar{y}\right) - 1 \right] \left[\exp(- (n\pi)^2 \bar{t}) - 1 \right]. \quad (2.18)$$

Finally, the settlement can be obtained from the displacements as follows:

$$s(\bar{t}) = \frac{1}{L} u(\bar{y} = 1, \bar{t}) = \frac{\sigma_{yy}}{E_s} \sum_{n \in \{2k+1 | k \in \mathbb{N}\}} \frac{8}{(n\pi)^2} \left[\exp(- (n\pi)^2 \bar{t}) - 1 \right] \quad (2.19)$$

where $\sum_{n \in \{2k+1 | k \in \mathbb{N}\}} \frac{8}{n^2 \pi^2} = 1$.

Here, the consolidation coefficient c_v satisfies $c_v = kE_s/\nu$, k is the permeability of the skeleton, ν is the dynamic viscosity of the interstitial fluid, and $E_s = K + 4G/3$ is the constrained modulus, K and G are the bulk and shear moduli of the (dry) skeleton, respectively. In this work, we obtained the constrained modulus E_s by discrete element modeling of the drained system (see Appendix B), and independently by taking the ratio of the total stress to the total strain observed in the experiments (cf., Fig. 2.4C), with E_s ranging from about 3.3-4.0 MPa; we fitted the consolidation coefficient since we did not have the true permeability of the system. As shown in Fig. 2.4, we used $E_s = 3.49$ MPa and $c_v = 304 \times 10^{-6}$ m²/s to fit experimental values.

Remark 3 *The dimensionless pressure in Eq. (2.17) and the settlement expression in Eq. (2.19) furnish analytical validation for the experimental results provided in*

the next section. As can be seen, the constrained modulus E affects the amount of maximum settlement and the coefficient of consolidation c_v scales the dimensionless time axis. Hence, at any point along the domain $y \in (0, L]$, the pressure evolution in time can be plotted using Eq. (2.17).

Experimental setup for fully saturated consolidation experiments

In this section, we describe the experimental device we developed to i) physically model the 1D consolidation problem solved in the previous section, ii) validate the experimental setup by comparing our measurements with those obtained analytically, and iii) measure interparticle forces that enable us to directly measure effective stress using Eq. (2.15). The experimental set up shown in Fig. 2.3A consists of a servo-hydraulic loading frame (MTS material test system, Model 358.10), load transducer (Model 11019), a CCD camera (Nikon AF Nikkor 50mm.), a fiber optic illuminator (Cole-Parmer, Model 41500-50) with a diffuser, a pressure sensor (OMEGA PX309-015GV), a valve (Push-to-Connect PVC On/Off valve, 1/4" OD tube) and a container that can hold a fully saturated and pressurized granular packing.

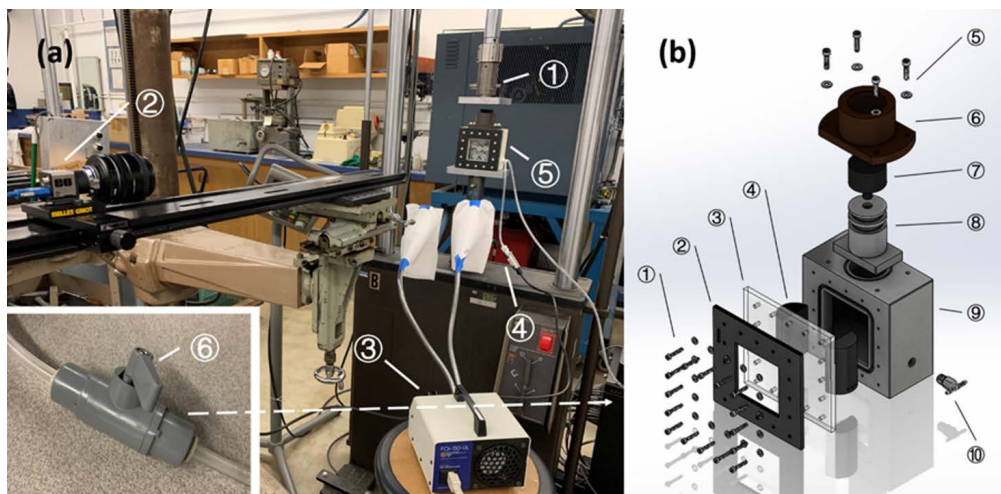


Figure 2.3: (a) Experimental setup: 1. Loading frame, 2. Camera, 3. Fiber optic illuminator, 4. Pressure sensor, 5. Container, 6. Valve (not shown in the large picture, shown in the inset). (b) Exploded view of the container: 1. #6-32 screws and washers, 2. Window bracket, 3. Transparent window, 4. Sidewalls, 5. #10-32 screws and washers, 6. Piston chamber, 7. Piston cap, 8. Piston, 9. Box, 10. Branch tube fitting.

The container, as shown in Fig. 2.3B, includes a box, a transparent window, a window bracket, two sidewalls, a piston, a piston cap, a piston chamber, and a branch tube

fitting. Since the shape of the box is complex and difficult to machine, the box, the window bracket as well as the sidewalls were 3D printed using a Stratasys Connex3 Objet350 printer. The box was made of VeroWhitePlus, while the window bracket and sidewalls were made of VeroBlackPlus. Additionally, the piston, the piston cap and the piston chamber were machined out of delrin and delrin acetal AF resin rods. A polycarbonate plate was used as the transparent window to enable optical imaging. Chemical-resistant Viton fluoroelastomer O-Rings were utilized to seal the whole setup and nylon socket head screws were used to hold all the parts together. To facilitate free drainage, a chemical-resistant barbed tube fitting was placed on the side of the box.

To study various configurations at the grain-scale, two types of multipurpose neoprene rubber rods were employed. These rod-shaped particles are assumed to be linear elastic and incompressible, i.e., Poisson's ratio ≈ 0.5 . The material used for the large particles (diameter = 20 mm, length = 25.4 mm) has a Young's modulus of 55 MPa, and the material used for the small particles (diameter = 7 mm, length = 25.4 mm) has a Young's modulus of 21.5 MPa, which we independently measured. Additionally, for these materials, the reported Coulomb friction coefficient is $\mu = 0.6$ [25]. The granular packings used in the experiments contain 6 large particles and 34 or 35 small particles. To achieve an appropriate grayscale speckle pattern for Digital Image Correlation (DIC) analysis, white multi-surface paint was used to generate speckle patterns on the black rubber particles.

2.3 Results

As illustrated in Fig. 2.2, we use a hybrid optical-mechanical approach to measure inter-particle forces and, via Eq. (2.16), the effective stress. To validate our approach, we reproduce the classic consolidation problem (Fig. 2.2A). This entails application of a constant stress σ_{yy} in the vertical direction, which is partitioned between the fluid pressure P and the effective stress σ'_{yy} carried by the solid [9]. In the classic consolidation problem, the time evolution of the pore fluid pressure p is modeled as a parabolic partial differential equation (cf., Section 2.2). The effective stress is typically inferred as $\sigma'_{yy} = \sigma_{yy} - P$, never directly measured experimentally—varying from zero at the beginning to the total stress at the end of the consolidation process. This indirect estimation of the effective stress is a consequence of the lack of a physical definition of effective stress and the inability to measure inter-particle forces in the presence of fluids. Here, we independently measure the fluid pressure and the effective stress evolutions in time and demonstrate that they account for the

total applied stress, as postulated by Terzaghi and formalized in Eq. (2.16). With this unprecedented access to local information at the grain-scale, we are able to explain how inter-particle forces are distributed in the presence of fluids and what controls the evolution of effective stress, questions that cannot be addressed using the current approaches.

To measure the inter-particle forces, we rely on the granular element method (GEM) [25] developed by the authors in the context of dry granular matter. We measure the strain in each rod-shaped particle using digital image correlation (DIC) [26]. The transparent wall in the apparatus (Fig. 2.2) allows us to employ simple optical methods to measure planar deformation, which is input into GEM to deduce the inter-particle forces. Other techniques of measuring average strains (e.g., x-ray diffraction, confocal microscopy) in the particles could also be employed [27, 28]. Thus, the effective stress and its evolution as a function of time is measured directly from inter-particle forces obtained from GEM. The volume V of the cell is important and it needs to be large enough such that the effective stress matches the imposed external stress [29] (see Discussion section). Additionally, the apparatus (Fig. 2.2) is equipped with a pressure sensor, located at the drainage orifice (Fig. 2.3A), to measure the fluid pressure as a function of time while the total stress is held constant by externally applied servo-controlled load. The measured pressure is assumed representative of the entire cell, which is a good assumption under quasi-static conditions. In addition, the pore pressure is analytically evaluated using Eq. (2.17). A drainage valve on the side of the apparatus allows for slow fluid transport and pressure diffusion leading to the consolidation process. This in turn provides direct access to the physics of force sharing between the fluid and solid phases, which controls the problem.

Figure 2.4A depicts the results obtained from the quasi-2D consolidation experiments that were conducted using the apparatus in Fig. 2.2A. The top figure shows the evolution of stresses and the pressure for three representative experiments with different granular configurations. They are plotted as a function of the consolidation ratio \bar{c} , defined as the ratio between the current deformation over the total deformation resulting from the consolidation process. One can observe that the total stress $\bar{\sigma}_{yy}$, the sum of the contributions of the fluid pore pressure \bar{P} and the effective stress $\bar{\sigma}'_{yy}$, is approximately constant (as prescribed at the top boundary). This result serves as validation of our approach since the effective stress is measured using Eq. (2.16), and independent of the pore pressure \bar{p} measurement. Initially,

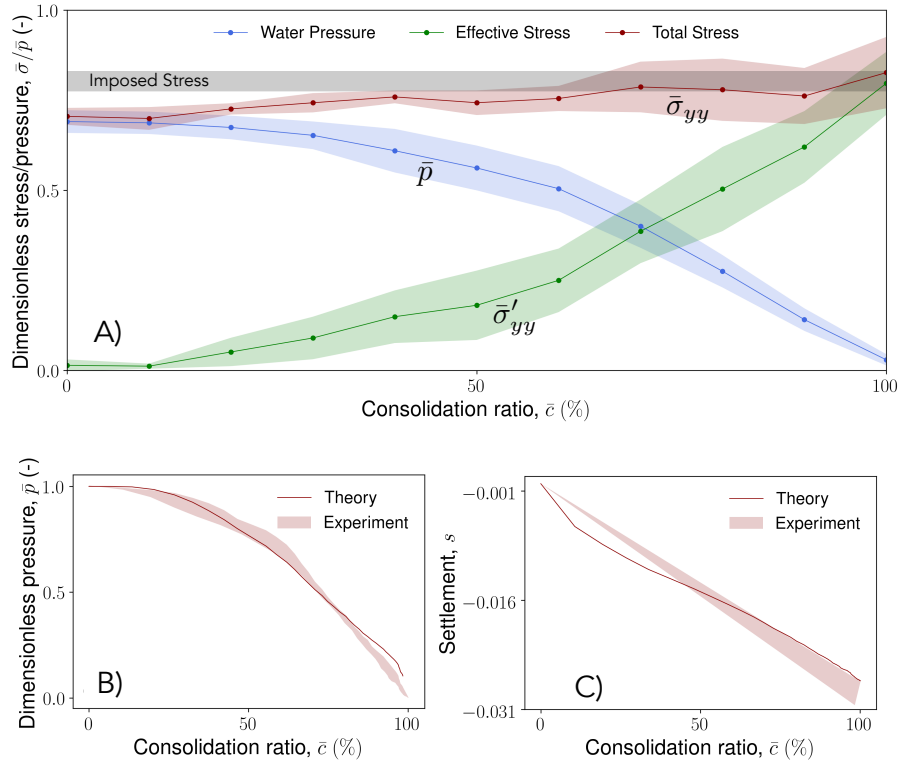


Figure 2.4: Experimental results with the shaded region capturing the range of results for various granular configurations. A) Evolution of total vertical stress $\bar{\sigma}_{yy}$, fluid pressure \bar{p} , and effective vertical stress $\bar{\sigma}'_{yy}$ as a function of consolidation ratio \bar{c} . In contrast to previous studies, the evolution of effective stresses is measured directly from the inter-particle forces (see Eq. (2.16) and Fig. 2.2). Shaded region of imposed stress represents standard deviation from desired stress level. B), C) Comparison between the measured pore pressure \bar{p} and the settlement s , respectively, with their counterparts of the analytical solution (Eq.(2.17) and (2.19)) as a function of the consolidation ratio \bar{c} ($E_s = 3.49$ MPa and $c_v = 304 \times 10^{-6}$ m²/s). Results serve as validation of the effective stress measurements and the experimental setup: in A) the total stress is approximately constant and additively decomposed between effective stress (measured) and pore pressure (measured); in B) the evolution of pore pressure \bar{P} measured at the bottom of the specimen corresponds to the pore pressure evaluated using Eq. (2.17); in C) the evolution of settlement measured in the specimens matches the settlement evaluated using Eq. (2.19).

as theoretically expected, the pore fluid carries the majority of the load. As the consolidation proceeds, the pore fluid pressure decreases and the effective stress increases, a manifestation of increase in inter-particle forces. A time lapse of the experiment (see Movie S1) highlights the evolution of inter-particle forces. When the consolidation process is around 75% complete, the effective stress and pore pressures appear to share load equally. At the end of the consolidation, the fluid pressure is entirely dissipated, and the effective stress of the solid carries the total external load. At this point, the system is completely drained, and pore pressure does not affect the mechanical response.

Remark 4 *It is important to note that the early portion of the total stress $\bar{\sigma}_{yy}$ measured in the experiments and reported in Fig. 2.4A shows a gap or difference with respect to the imposed stress. This difference is mostly present in the early portion of the consolidation process (close to $\bar{c} = 0\%$) when the pore pressure \bar{p} dominates the total stress. This error is likely due to the pressure sensor being located near the entrance of the drainage valve, which would naturally induce lower pressures necessary for (slow) fluid flow. The error decreases passed $\bar{c} = 50\%$ as the pore pressure \bar{p} drops and the effective stress $\bar{\sigma}'_{yy}$ starts to dominate the response.*

The consolidation problem serves as a validation exercise for our newly derived expression for effective stress (Eq. (2.16)). This is achieved by comparing the evolution of both the pore pressure \bar{P} and the settlement s against the well-known analytical solutions for consolidation (Eq. (2.17) and (2.19)). Figure 2.4B shows comparisons between the fluid pressure measured in the experiments and the analytical solution furnished by Eq. (2.17). As noted earlier, the analytical solution for pore pressure depends on the coefficient of consolidation, which here is calibrated to capture the flow rate of the experiments. Similarly, in Fig. 2.4C, the settlement s for the granular assembly in the experiment is compared to the analytical solution furnished by Eq. (2.19). Also, the maximum settlement (at $\bar{c} = 100\%$) is controlled by the constrained modulus E_s . As shown in Fig. 2.4, the consolidation coefficient c_v and the constrained elastic modulus E_s yield values that are well within those reported in the literature [30]. Thus, our approach to measure inter-particle forces is validated with well-known analytical solutions of the consolidation problem. This enables us to make a direct link between the evolution of inter-particle forces and effective stresses at the core of many poromechanical systems. It is important to note that while our results explicitly link the effective stress model developed by Terzaghi to

grain-scale phenomena, our approach does not rely on phenomenological assumptions, and holds for general cases beyond the consolidation example presented here (e.g., 3D loading).

2.4 Discussion

We now turn our attention to the following question: how are forces distributed in the particles—over time—in the presence of fluids? We use our physics-based model to decode the mechanism controlling evolution of forces in the presence of fluids, in particular the case of a fully saturated granular medium. Taking the time evolution of the theoretical expression for the total stress in Eq. (2.15), the time evolution of the effective stress is seen as a combination of the time evolutions of the inter-particle forces and the branch vectors enabling such contacts i.e., $\dot{\sigma}' = 1/V \sum_{\alpha} (\dot{f}^{\alpha} \otimes \ell^{\alpha} + f^{\alpha} \otimes \dot{\ell}^{\alpha})$. In a geometrically frustrated system, i.e., one where grains are not allowed to reconfigure, like the one shown in Fig. 2.2, the branch vectors do not evolve significantly since the particles are geometrically constrained and unable to rearrange. Therefore, in such a system, the evolution of the effective stress is dominated by the evolution of inter-particle forces such that

$$\dot{\sigma}' \approx \frac{1}{V} \sum_{\alpha} \dot{f}^{\alpha} \otimes \ell^{\alpha}. \quad (2.20)$$

With a constant total stress, the reduction in pore pressure must be directly matched by a corresponding increase in effective stress (i.e., $\dot{P} = -\dot{\sigma}'_{yy} \approx -1/V \sum_{\alpha} \dot{f}_y^{\alpha} \ell_y^{\alpha}$). As shown in Fig. 2.5A, the pore pressure evolution is countered by the evolution of the vertical effective stress. This in turn relies on the evolution of horizontal and vertical force chains carried by contacts with largest components in those preferred directions. We conjecture that the orientation of the branch vectors acts as a catalyst in the evolution of inter-granular energy density, since contacts with existing components in the vertical direction can do more work for a given increment of force. It is important to note that neither phenomenology nor analogs with drained systems can provide insights into the question of force distribution. The former can only provide the current effective stress by inference or via constrained moduli and the latter can only explain force distribution in dry systems. The effect of interstitial fluids is to control the rate of evolution in fluid-saturated systems, thereby affecting the force distribution, including under equivalent effective stresses. Even in dry systems, the same macroscopic stress may result in a different force distribution. This is only exacerbated in diffusion-controlled fluid-saturated systems.

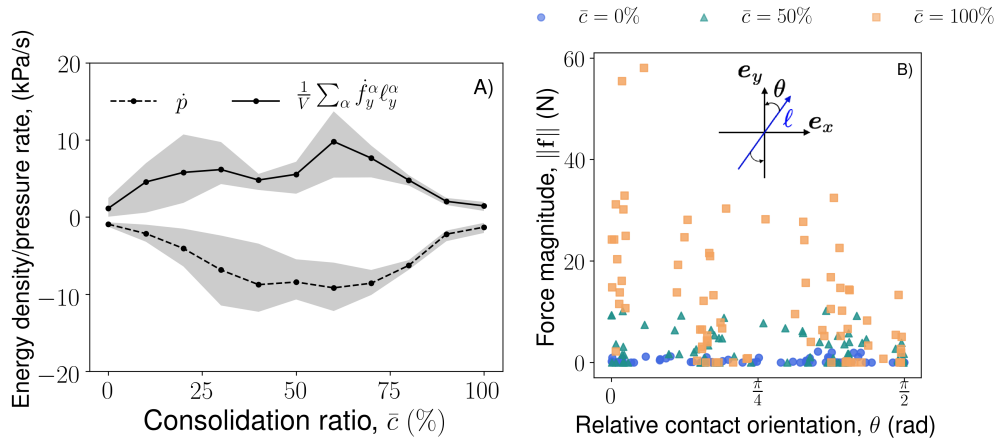


Figure 2.5: Mechanism controlling the evolution of forces and effective stress with time (consolidation) in a fully saturated granular system. A) Evolution of pore pressure countered by the work rate done by the vertical forces in three different experiments. B) Scatter plot of force magnitude and contact orientation relative to the direction of load application, showing clear increases in magnitude of force as consolidation evolves, especially in the direction of loading ($\theta = 0$).

Figure 2.5B shows a scatter plot of relative contact orientations and the force magnitudes associated with them for one of the experiments conducted in our study. Representative of the other experiments, this plot suggests that, initially, the distribution of force magnitudes is fairly uniform along available branch vectors. As the energy density rate associated with the inter-particle forces peaks (Fig. 2.5A), the distribution of forces displays an increase in magnitude in the direction of vertically aligned branch vectors (Fig. 2.5B). This supports our conjecture that branch vectors play the role of catalysts in the evolution of inter-granular energy density. By the end of the consolidation process, the forces reach peak magnitude, with strong directionality along the branch vectors that point along the direction of macroscopic load application. Remarkably, about 5% of particle contacts are responsible for 95th (p95) percentile of force distribution during the experiment (Fig. A.3). These contacts are clearly biased towards the vertical direction as the pore pressure diffusion shifts the load-carrying burden from the fluid phase onto the solid phase.

Two issues come to mind that have important implications for the results presented herein. First, volume averaging equations require a representative unit cell of large enough volume V such that one can properly define continuum variables such as the effective stress σ' . Clearly, results would vary slightly with different sizes of

V . In this study, we do not analyze in depth the effects of V , rather we use the notion that internal stress calculated using volume averaging, are equal to external applied stresses when the volume V is appropriate [29, 31]. In this particular case, the effective stress values at the end of consolidation perfectly match the external stress applied at the boundary, and all other continuum results (e.g., pore pressure P and settlement s) match the continuum theoretical results (see Fig. 2.4). Second, the effect of fluid-saturation in the inter-granular force distribution and evolution should be addressed. It is tempting to extrapolate that, since the effective stress is related to the inter-granular contact forces just like in the fully drained case, hence the force distribution should be the same regardless of the fluid for a given level of effective stress. While tempting, this is not necessarily the case, as seen in Eq. (2.20), since the time evolution of effective stress is controlled by the time evolution of the pore pressure such that $\dot{\sigma}'_{yy} \sim -\dot{P}$ (see Fig. 2.5A) and, therefore, the fluid pressure diffusion affects the time evolution of the inter-granular forces; the latter being path-dependent.

The linkage of effective stress and the force measurements in the presence of fluids allows us to reconstruct the evolution of effective stress, pore fluid pressure, and total stress—independently—for the first time since the concept of effective stress was introduced a century ago. Specifically, we focused our efforts on validating our approach against the limiting case that corresponds to Terzaghi’s definition of effective stress. However, our hybrid approach is versatile and can be further developed to explore complex poromechanical systems, unraveling the intimate coupling between inter-particle forces and solid stresses in the presence of fluids. For example, inter-cellular forces could be directly measured using a similar hybrid approach, with different computational and experimental ingredients, to complement the existing models for capturing cell behavior [32, 33]. Furthermore, in a departure from continuum roots, a recent discrete formulation of poroelasticity enables direct access to Biot pore pressure coupling coefficients [34], which drive diffusion in deformable solids due to inter-particle forces. Thus, poroelastic diffusion can be considered as a design parameter for tissue engineering and drug delivery applications. This hybrid framework also offers a path to directly probe capillary pressures in wet, disordered granular systems utilizing for example a recent computational framework that can account for the formation, growth, and coalescence of liquid clusters while properly mapping the spatial distribution of capillary forces [35]. Such capability can provide tools in granular physics to robustly define effective stress in partially saturated porous media [36]. So far, most models have relied on validating only the kinemat-

ics given the dearth of experimental measurement of forces. Our results open the door for simultaneously accessing kinematics (deformation) and kinetics (forces) in poromechanical systems, which can facilitate the formulation of predictive models that capture the underlying physics of these complex systems.

BIBLIOGRAPHY

- [1] C.C. Faunt et al. “Water availability and land subsidence in the Central Valley, California, USA”. In: *Hydrogeology Journal* 24.3 (2016), pp. 675–684.
- [2] M.B. Smith and C. Montgomery. *Hydraulic fracturing*. Crc Press, 2015.
- [3] G. Odell et al. “A mechanical model for epithelial morphogenesis”. In: *Journal of Mathematical Biology* 9.3 (1980), pp. 291–295.
- [4] J. Christensen. “Modeling diffusion-induced stress in Li-ion cells with porous electrodes”. In: *Journal of the Electrochemical Society* 157.3 (2010), A366.
- [5] J. Jiang and N. Lapusta. “Deeper penetration of large earthquakes on seismically quiescent faults”. In: *Science* 352.6291 (2016), pp. 1293–1297.
- [6] J.R. Rice, J.W. Rudnicki, and J.D. Platt. “Stability and localization of rapid shear in fluid-saturated fault gouge: 1. Linearized stability analysis”. In: *Journal of Geophysical Research: Solid Earth* 119.5 (2014), pp. 4311–4333.
- [7] F. Cappa et al. “Stabilization of fault slip by fluid injection in the laboratory and in situ”. In: *Science Advances* 5.3 (2019), eaau4065.
- [8] E.O. Shelley, E.T. Gonzalez, and E.S. Villa. “Options for correcting differential settlements in Mexico City’s Metropolitan Cathedral”. In: *14th International Conference on Soil Mechanics and Foundation Engineering (Hamburg)*. 1997.
- [9] K. Terzaghi. *Erdbaumechanik auf bodenphysikalischer grundlage*. Leipzig u. Wien, F. Deuticke, 1925.
- [10] O. Coussy. *Poromechanics*. John Wiley & Sons, 2004.
- [11] M.A. Biot. “General theory of three-dimensional consolidation”. In: *Journal of Applied Physics* 12.2 (1941), pp. 155–164.
- [12] R.I. Borja. “Cam-Clay plasticity. Part V: A mathematical framework for three-phase deformation and strain localization analyses of partially saturated porous media”. In: *Computed Methods in Applied Mechanics and Engineering* 193 (2004), pp. 5301–5338.
- [13] J.C. Simo and T.J.R. Hughes. *Computational inelasticity*. Vol. 7. Springer Science & Business Media, 2006.
- [14] T.S. Majmudar and R.P. Behringer. “Contact force measurements and stress-induced anisotropy in granular materials”. In: *Nature* 435.7045 (2005), pp. 1079–1082.
- [15] K.E. Daniels, J.E. Kollmer, and J.G. Puckett. “Photoelastic force measurements in granular materials”. In: *Review of Scientific Instruments* 88.5 (2017), p. 051808.

- [16] C.R. Ladd and J.E. Reber. “The effect of a liquid phase on force distribution during deformation in a granular system”. In: *Journal of Geophysical Research: Solid Earth* 125 (2020), e2020JB019771.
- [17] N. Mahabadi and J. Jang. “The impact of fluid flow on force chains in granular media”. In: *Applied Physics Letters* 110 (2017), p. 041907.
- [18] J.E. Andrade and R. Borja. “Modeling deformation banding in dense and loose fluid-saturated sands”. In: *Finite Elements in Analysis and Design* 43 (2007), pp. 361–383.
- [19] R.J. Atkin and R.E. Craine. “Continuum theories of mixture: Basic theory and historical development”. In: *Quarterly Journal of Mechanics and Applied Mathematics* 29 (1976), pp. 209–244.
- [20] J.H. Prevost. “Mechanics of continuous porous media”. In: *International Journal of Engineering Science* 18 (1980), pp. 787–800.
- [21] J. Christoffersen, M.M. Mehrabadi, and S. Nemat-Nasser. “A micromechanical description of granular material behavior”. In: *Journal of Applied Mechanics* 48 (1981), pp. 339–344.
- [22] S.A. Galindo-Torres, X. Zhang, and K. Krabbenhoft. “Micromechanics of liquefaction in granular materials”. In: *Physical Review Applied* 10 (2018), p. 064017.
- [23] M.R. Kuhn and A. Daouadji. “Simulation of undrained quasi-saturated soil with pore pressure measurements using a discrete element (DEM) algorithm”. In: *Soils and Foundations* 60 (2020), pp. 1097–1111.
- [24] L. Rothenburg and A.P.S. Salvadurai. “A micromechanical definition of the Cauchy stress tensor for particulate media”. In: *Mechanics of Structured Media*. Ed. by APS Salvadurai. 1981, pp. 469–486.
- [25] R. Hurley et al. “Extracting inter-particle forces in opaque granular materials: beyond photoelasticity”. In: *Journal of the Mechanics and Physics of Solids* 63 (2014), pp. 154–166.
- [26] M.A. Sutton, J.J. Orteu, and H. Schreier. *Image correlation for shape, motion and deformation measurements: Basic concepts, theory and applications*. Springer Science & Business Media, 2009.
- [27] K. Mac Donald and G. Ravichandran. “Confocal microscopy and digital volume correlation methods for intergranular force transmission experiments”. In: *Experimental Techniques* 43 (2019), pp. 457–468.
- [28] R.C. Hurley et al. “Quantifying interparticle forces and heterogeneity in 3D granular materials”. In: *Physical Review Letters* 117 (2016), p. 098005.
- [29] T.I. Zohdi and P. Wriggers. *An introduction to computational micromechanics*. Springer, 2005.

- [30] R.D. Holtz, W.D. Kovacs, and T.C. Sheahan. *An introduction to geotechnical engineering*. Vol. 733. Prentice-Hall Englewood Cliffs, NJ, 1981.
- [31] J.E. Andrade et al. “Granular element method for computational particle mechanics”. In: *Computer Methods in Applied Mechanics and Engineering* 241–244 (2012), pp. 262–274.
- [32] J. Notbohm et al. “Three-dimensional analysis of the effect of epidermal growth factor on cell-cell adhesion in epithelial cell clusters”. In: *Biophysical Journal* 102.6 (2012), pp. 1323–1330.
- [33] R. Sunyer et al. “Collective cell durotaxis emerges from long-range intercellular force transmission”. In: *Science* 353.6304 (2016), pp. 1157–1161.
- [34] S. Monfared et al. “Mesoscale poroelasticity of heterogeneous media”. In: *Journal of Nanomechanics and Micromechanics* 7.4 (2017), p. 04017016.
- [35] S. Monfared et al. “Effect of confinement on capillary phase transition in granular aggregates”. In: *Physical Review Letters* 125.25 (2020), p. 255501.
- [36] N. Lu. “Unsaturated soil mechanics: fundamental challenges, breakthroughs, and opportunities”. In: *Journal of Geotechnical and Geoenvironmental Engineering* 146.5 (2020), p. 02520001.

*Chapter 3***INTERPARTICLE FORCES AND EFFECTIVE STRESS IN
UNSATURATED GRANULAR MEDIA**

- [1] Z. Gu, J.E. Andrade, and G. Ravichandran. “Interparticle forces and effective stress in unsaturated granular media”. Under preparation. 2023.

ABSTRACT

Measuring and characterizing inter-particle contact forces in unsaturated granular systems remains a challenge. This is due to the complex nature of unsaturated material with the presence of both fluid and gas phases, in addition to the solid phase. Despite a lot of efforts, the correlation between effective stress and grain-scale forces remains unclear. On this account, an expression for the partition of stresses between the three media as a function of grain-scale forces is derived. Capillary bridges, which are integral parts of the system are simulated numerically using 2D finite element analysis (FEM) to further understand the influence of gravity on pore fluid clusters under low saturation condition. Finally, a hybrid optical-mechanical method combined with the granular element method (GEM) is developed to extract inter-particle forces and determine the stress partitioning in a classic 1D consolidation experiment. The theoretical derivation and experimental validation could facilitate unraveling the mechanics and physics behind the intricate constitutive behaviors of unsaturated granular systems.

Keywords: *Unsaturated granular media; Contact forces; Effective stress; Hybrid optical-mechanical experiments*

3.1 Introduction

Composed of solid, fluid, and gas (air in most cases), unsaturated soil exists ubiquitously in nature and covers broad areas of the earth's surface [1–3]. The mechanical behavior of unsaturated soil (such as strength and deformation) during consolidation gives rise to multiple physicommechanical phenomena in granular mechanics, geophysics, and construction industry [4–6]. For example, the Leaning Tower of Pisa, shown in Fig. 3.1, is famous for its near four-degree lean that happened during construction. As the weight of the 14,500-ton tower transferred through the complex soil structure underneath, consolidation occurred in different strata. Because of the sea sedimentation on the north side of the tower and excess pore pressure on the south side, uneven consolidation behavior took place, especially in the unsaturated soil layer (capillary fringe), which led to the uneven sediment of the tower's foundation [7, 8].

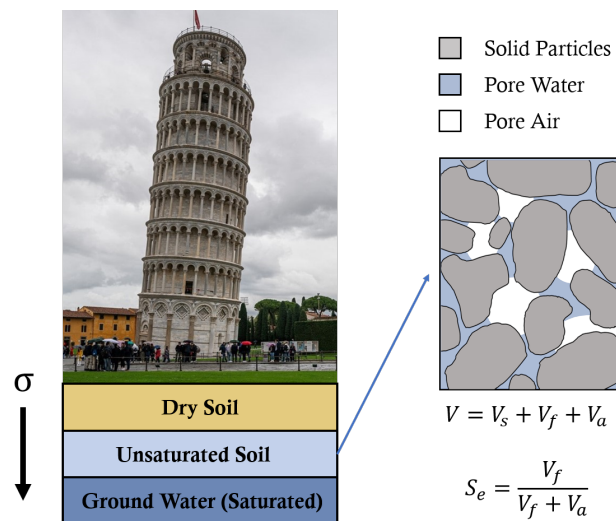


Figure 3.1: The Leaning Tower of Pisa is a world-famous tourist attraction due to its severe tilt caused by uneven settling of the building's foundation. As the weight of the tower transfers through the soil beneath it, consolidation occurs in different soil layers. The schematic of unsaturated granular soil of a total volume V and saturation S_r is shown on the right. Different from dry soil and saturated soil, the unsaturated soil layer contains both pore water (V_f) and pore air (V_a), increasing the complexity of force and stress transmission during the consolidation process.

Since proposed by Karl Terzaghi in 1920s, the concept of effective stress gives a good empirical description of stress distribution in dry or fully saturated granular soil [9]. In such systems, the effective stress is the difference between total stress

and pore fluid pressure. In the past several decades, much research has been carried out to expand the concept of effective stress to unsaturated granular systems. While a proposed form of effective stress due to Bishop provides a methodology for studying isotropic unsaturated systems at the macro-scale [10], additional efforts are still needed in the determination of the coefficient of effective stress in different systems. Fredlund et al. also put forth a popular two-stress state approach to theoretically solve the consolidation process and the effective stress. Their research provided combinations of two stress variables that can be used to define the behavior of unsaturated soil [11, 12]. However, the two governing continuity equations of consolidation introduced by Fredlund are highly nonlinear with parameters incorporating soil material properties that are hard to evaluate. It has also been shown by others that more stress state variables are needed to describe complex constitutive behaviors of unsaturated systems [13, 14]. Additionally, a thermodynamic framework has been established by Lu et al. to derive the closed-form equation for effective stress [15]. However, in their derivation, the influence of the surface tension and residual fluid layer is neglected or simplified.

In recent decades, due to the rapid development of technology and imaging techniques, several experimental works have been carried out to decipher force transmission at grain-scale. Photoelastic materials have been widely employed in the visualization of particle contact forces [16, 17]. However, the use of photoelasticity is mostly limited to transparent systems made with birefringent particles. While X-ray computed tomography (XRCT) and X-ray diffraction (XRD) can be used in tracking the movement and deformation of large numbers of particles [18–20], it is difficult for the XRCT method to evaluate shear deformation within these particles and XRD often fails to capture all Bragg peaks. Furthermore, although mechano-luminescent (ML) material makes it possible to directly visualize the magnitude of inter-particle forces [21], it could not differentiate between the normal and tangential contact forces. As a way of overcoming these obstacles, a hybrid optical-mechanical process combined with the granular element method (GEM) was originally developed by Andrade et al. [22] and modified by Hurley et al. [23] to measure particle interactions in dry granular packing. This novel GEM approach has successfully extracted intergranular forces in opaque grain systems under different loading conditions. The subsequent research work by Andrade et al. further expands the use of GEM to saturated granular packing and reveals the physical correlation between intergranular forces and Terzaghi's effective stress [24].

However, despite all the theoretical and experimental studies mentioned above, the force transmission and grain-scale expression of effective stresses in unsaturated granular packing are not yet fully understood. This is mostly attributed to the coexistence of three different phases, solid, liquid, and gas. The fluid-gas interface (contractile skin) is sometimes suggested and defined as the fourth phase [25]. In the state of mechanical equilibrium, the external load applied to a partially saturated granular system is carried by a combination of forces and pressures in the solid skeleton (V_s), pore fluid (V_f), and pore gas (V_a). The additional forces induced by pore pressure variance and fluid-gas surface tension to the particles make the mechanical behavior of an unsaturated granular system extremely complex [26]. The presence of interfaces between different phases as well as multiphase flows also significantly increases the difficulty of imaging and pore fluid/gas tracking.

The goal of this investigation here is to mathematically derive and experimentally validate the correlation between the intergranular forces and the effective stress in unsaturated granular systems at grain-scale. In section 2, the mathematical derivation of the stress partition equation, the numerical analysis of a 2D capillary bridge, and the governing equations of unsaturated GEM, and the classical 1D consolidation model for unsaturated media are presented. In section 3, the experimental setup and image analysis techniques of the hybrid optical-mechanical method to validate the stress partition equation are described. The results and analysis of a 1D consolidation experiment are described in section 4 and the conclusions for the study are presented in section 5.

3.2 Theory and Analysis

The following section discusses the four necessary components to directly measure the inter-particle force chains and effective stress in unsaturated granular media: *i*) derivation of the stress partition equation and effective stress in an unsaturated grain system, *ii*) 2D numerical simulation of a capillary bridge between solid disks, *iii*) the governing equations of the unsaturated GEM, and *iv*) the theory of 1D consolidation.

Effective stress in partially saturated systems

To derive the physical expression of the effective stress in partially saturated systems, this work focuses on granular packings with the following three assumptions: *i*) low saturation ($S_r \ll 1$) with quasi-static state, *ii*) incompressible solid (particles) and fluid constituents, and *iii*) cohesionless solid grains with point contacts. For a

partially granular system with a total volume of V , similar to the stress decomposition of saturated systems [22], the additive decomposition of partial stresses gives the average stress of the entire granular packing:

$$\bar{\sigma} = \bar{\sigma}^s + \bar{\sigma}^f + \bar{\sigma}^a \quad (3.1)$$

where each partial stress ($\bar{\sigma}^s$, $\bar{\sigma}^f$, $\bar{\sigma}^a$) is the volume average of the stress field in the corresponding phase occupying a volume V_s for the solid (s), V_f for the fluid (f), and V_a for the gas (air) phase (a). In an unsaturated system with low saturation $S_r = V_f/(V_f + V_a) \ll 1$, we further assume the space of pore gas is connected and a constant pore gas pressure P_a throughout the whole system. Equation (3.1) then becomes:

$$\bar{\sigma} = \bar{\sigma}^s + \bar{\sigma}^f + \phi^a P_a \mathbf{1} \quad (3.2)$$

where $\phi^a := V_a/V$ is the volume fraction occupied by the gas phase. Consider a low saturation granular system consisting of N solid particles and M pore fluid clusters. For a given particle i shown in Fig. 3.2, the conservation of linear and angular momentum yields:

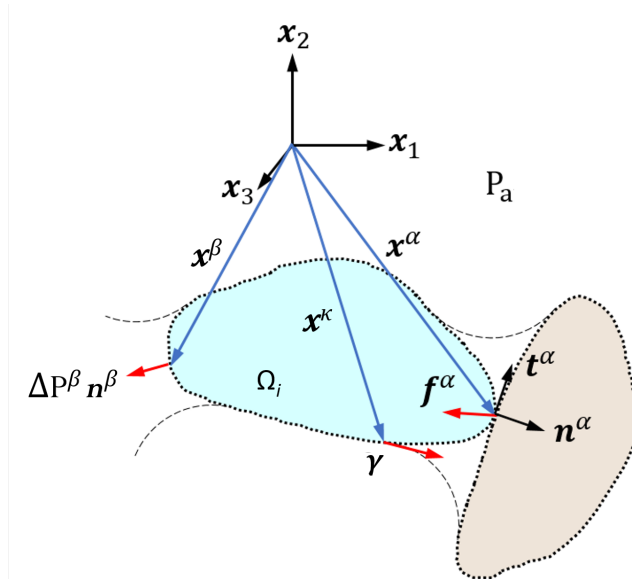


Figure 3.2: Schematic plot of forces acting on a solid grain i in a partially saturated granular packing.

$$\sum_{\alpha=1}^{N_i^s} \mathbf{f}^\alpha + \sum_{\beta=1}^{N_i^f} \left(\int_{S_i^\beta} \Delta P^\beta \hat{\mathbf{n}} dS + \int_{L_i^\beta} \boldsymbol{\gamma}^\beta dL \right) = \mathbf{0} \quad (3.3)$$

$$\sum_{\alpha=1}^{N_i^s} \mathbf{x}^\alpha \times \mathbf{f}^\alpha + \sum_{\beta=1}^{N_i^f} \left(\int_{S_i^\beta} \mathbf{x}^\beta \times \Delta P^\beta \hat{\mathbf{n}} dS + \int_{L_i^\beta} \mathbf{x}^\beta \times \boldsymbol{\gamma}^\beta dL \right) = \mathbf{0} \quad (3.4)$$

$$\Delta P^\beta = P_a - P_f^\beta$$

where \mathbf{f}^α is a contact force at particle-particle and particle-boundary contact point \mathbf{x}^α with N_i^s being the total number of particle-particle contact points acting on particle i . ΔP^β represent the pressure difference between pore gas P_a and pore fluid P_f^β at solid-fluid contact surface S_β with N_i^f being the total number of solid-fluid contact surfaces acting on particle i . $\hat{\mathbf{n}}$ is the point-wise normal unit vector at point \mathbf{x}^β on the solid-fluid contact surface S_β . While $\boldsymbol{\gamma}^\beta$ represents the surface tension acting on the solid particle at point \mathbf{x}^β on contour L_β of the solid-fluid contact surface S_β . Here we assume that the gas and fluid are in a quasistatic state and the pressure variance within each fluid cluster is negligible.

In the case of quasistatic states, pointwise linear momentum balance prevails within a solid particle i .

$$\nabla \cdot \boldsymbol{\sigma}_i(\mathbf{x}) = 0 \quad \forall \mathbf{x} \in \Omega_i \quad (3.5)$$

where $\boldsymbol{\sigma}_i(\mathbf{x})$ is the stress field at point \mathbf{x} in the domain Ω_i of particle i . Based on Eq. (3.2), the total average stress of a partially saturated system, composed of solid, fluid, and air domains, can be written as:

$$\bar{\boldsymbol{\sigma}} = \frac{1}{V} \int_V \boldsymbol{\sigma}(\mathbf{x}) dV = \phi^s \bar{\boldsymbol{\sigma}}_s + \phi^f \bar{\boldsymbol{\sigma}}_f + \phi^a P_a \mathbf{1} \quad (3.6)$$

where $\phi^s := V_s/V$, $\phi^f := V_f/V$, and $\phi^a := V_a/V$ are volume fraction of solid, fluid, and gas phases respectively. The average stress of the solid phase and fluid phase can be further expressed separately as:

$$\bar{\boldsymbol{\sigma}}_s = \frac{1}{V_s} \sum_{i=1}^N V_i \bar{\boldsymbol{\sigma}}_i \quad (3.7)$$

$$\bar{\boldsymbol{\sigma}}_f = \frac{1}{V_f} \sum_{j=1}^M V_j \bar{P}_j \mathbf{1} = \frac{1}{V_f} \sum_{j=1}^M V_j P_j \mathbf{1} \quad (3.8)$$

$$\sum_{i=1}^N V_i = V_s \quad \sum_{j=1}^M V_j = V_f$$

where V_i denotes volume associated with solid domain Ω_i , V_j denotes volume associated with fluid domain ω_j . The sum of volumes of all solid particles/fluid clusters is the volume of the solid phase/fluid phase.

Further considering the expression of solid particle average stress $\bar{\boldsymbol{\sigma}}_i$, combining it with Eq. (3.5) and applying the divergence theorem,

$$\begin{aligned} \bar{\boldsymbol{\sigma}}_i &= \frac{1}{V_i} \int_{S_i} \text{sym}(\mathbf{t} \otimes \mathbf{x}) dS \\ &= \frac{1}{V_i} \sum_{\alpha=1}^{N_i^s} \text{sym}(\mathbf{f}^\alpha \otimes \mathbf{x}^\alpha) - \frac{1}{V_i} \sum_{\beta=1}^{N_i^f} \left\{ \int_{L_i^\beta} \text{sym}(\boldsymbol{\gamma}^\beta \otimes \mathbf{x}^\beta) dL \right. \\ &\quad \left. + \int_{S_i^\beta} \Delta P^\beta \text{sym}(\hat{\mathbf{n}} \otimes \mathbf{x}^\beta) dS \right\} + P_a \mathbf{1} \end{aligned} \quad (3.9)$$

where \mathbf{t} is the traction at any point $\mathbf{x} \in S_i$, \mathbf{x}^α is a vector from an arbitrarily chosen origin to the contact point α , and \otimes is the dyadic product. To further simplify this expression, it is assumed that the grains have good roundness. The solid-fluid contact area S_β is relatively small and can be considered as a spherical surface with a radius R^β . By substituting Eq. (3.9) into Eq. (3.7), and Eqs. (3.7) and (3.8) into Eq. (3.6) the average total stress can be expressed as:

$$\begin{aligned} \bar{\boldsymbol{\sigma}} &= \frac{1}{V} \sum_{\alpha=1}^{N^s} \text{sym}(\mathbf{f}^\alpha \otimes \mathbf{l}^\alpha) + P_a \mathbf{1} - \frac{1}{V} \sum_{j=1}^M V_j (P_a - P_f^j) \mathbf{1} \\ &\quad - \frac{1}{V} \sum_{\beta=1}^{N^f} \Delta P^\beta \int_{S_\beta} R^\beta \hat{\mathbf{n}} \otimes \hat{\mathbf{n}} dS_\beta - \frac{1}{V} \sum_{\beta=1}^{N^f} \int_{L_\beta} R^\beta \text{sym}(\boldsymbol{\gamma}^\beta \otimes \hat{\mathbf{n}}) dL_\beta \end{aligned} \quad (3.10)$$

where N^s is the number of particle-particle contacts in the entire domain, and N^f is the number of solid-fluid contact surfaces in the entire domain. P_f^j is the pore fluid pressure in the fluid domain ω_j . \mathbf{l}^α is the branch vector connecting two centroids of the particles contacting at point α , and R^β are the radii of curvatures of the corresponding solid-fluid contact areas.

In Eq. (3.10), the first term in the expression of $\bar{\sigma}$ corresponds to the Love formula and agrees with the form reported by Christoffersen et al. [27, 28]. It is denoted as the effective stress σ' as it represents the behavior of the solid phase and is related to inter-particle force chains. While the second term in Eq. (3.10) is the contribution of pore gas pressure, the third, fourth, and fifth terms are due to the presence of both fluid and gas phases. The third term corresponds to the presence of the fluid domain. Additionally, the fourth and fifth terms represent the stress induced by fluid-gas pressure difference and surface energy separately. In systems with low saturation, Eq. (3.10) represents stress transfer in granular packing with capillary bridges between solid particles.

A further comparison between Eq. (3.10) and Bishop's effective stress can be carried out. For a three-phase system consisting of solid, fluid, and gas, the Bishop's effective stress states that:

$$\sigma'_B = \bar{\sigma} - P_a \mathbf{1} + \chi(P_a \mathbf{1} - \bar{\sigma}_f) \quad (3.11)$$

where σ'_B is Bishop's single effective stress, and χ is the effective stress parameter [10]. Note that one should not directly combine Eq. (3.10) with Eq. (3.11) (assuming $\sigma' = \sigma'_B$) as the definition of the effective stress may be different in different frameworks. Further recall that Bishop's empirical expression is directly based on Terzaghi's principle and the effective stress parameter χ should range from 0 to 1, with $\chi = 0$ refers to dry systems and $\chi = 1$ refers to fully saturated systems. Therefore, the stress partition equation Eq. (3.10) can be rewritten as:

$$\begin{aligned}
\bar{\boldsymbol{\sigma}} &= \frac{1}{V} \sum_{\alpha=1}^{N^s} \text{sym}(\mathbf{f}^\alpha \otimes \mathbf{l}^\alpha) + \frac{1}{V} \sum_{j=1}^M V_j P_f^j \mathbf{1} \\
&+ \frac{1}{V} \sum_{\beta=1}^{N^f} P_f^\beta \int_{S_\beta} R^\beta \hat{\mathbf{n}} \otimes \hat{\mathbf{n}} dS_\beta - \frac{1}{V} \sum_{\beta=1}^{N^f} \int_{L_\beta} R^\beta \text{sym}(\boldsymbol{\gamma}^\beta \otimes \hat{\mathbf{n}}) dL_\beta \\
&+ (1 - \phi^f - \frac{1}{V} \sum_{\beta=1}^{N^f} \int_{S_\beta} R^\beta \hat{\mathbf{n}} \otimes \hat{\mathbf{n}} dS_\beta) P_a \mathbf{1}
\end{aligned} \tag{3.12}$$

For $\chi = 1$, Eq. (3.12) should not depend on pore gas pressure P_a . Therefore, the parameter χ and the Bishop's effective stress $\boldsymbol{\sigma}'_B$ can be derived as the following expressions:

$$\begin{aligned}
\chi \mathbf{1} &= \phi^f \mathbf{1} + \frac{1}{V} \sum_{\beta=1}^{N^f} \int_{S_\beta} R^\beta \hat{\mathbf{n}} \otimes \hat{\mathbf{n}} dS_\beta = S_r \phi \mathbf{1} + \frac{1}{V} \sum_{\beta=1}^{N^f} \int_{S_\beta} R^\beta \hat{\mathbf{n}} \otimes \hat{\mathbf{n}} dS_\beta \\
\boldsymbol{\sigma}'_B &= \frac{1}{V} \sum_{\alpha=1}^{N^s} \text{sym}(\mathbf{f}^\alpha \otimes \mathbf{l}^\alpha) - \frac{1}{V} \sum_{\beta=1}^{N^f} \int_{L_\beta} R^\beta \text{sym}(\boldsymbol{\gamma}^\beta \otimes \hat{\mathbf{n}}) dL_\beta
\end{aligned} \tag{3.13}$$

where ϕ is the porosity. Note that, although this expression is deduced under the assumption of low saturation, an equation with a similar form can also be obtained by segmenting the solid-fluid contact area such that the small contact assumption is valid for each segment. It can be derived from Eq. (3.13) that $\chi = 0$ when $\phi^f = 0$ and $\chi = 1$ when $\phi^f = 1 - \phi^s$, which is consistent with Bishop's definition of the effective stress parameter. From Eq. (3.13), the effective stress parameter and the Bishop's effective stress depend on both the saturation and the fabric of the granular system, which illustrates the intrinsic non-linearity of the parameter χ as a function of saturation S_r . Although the matrix $\hat{\mathbf{n}} \otimes \hat{\mathbf{n}}$ is positive definite, it is not generally true that the χ is a monotonic function of saturation S_r , since the solid-fluid contact area may decrease as the result of particle rearrangement, fluid vaporization, vapor condensation, etc., even if the fluid content increases. This also gives rise to questions concerning the uniqueness of the effective stress parameter χ as a function of S_r [29, 30].

For a granular system with large particle number N and randomly distributed solid-fluid contacts, it can be shown that the expression of parameter χ (Eq. (3.13)) can also be written as:

$$\chi = \phi^f + \frac{1}{3V} \sum_{\beta=1}^{N^f} \int_{S_\beta} R^\beta dS_\beta. \quad (3.14)$$

Therefore, with the stress partition equation Eq. (3.10), the grain-scale expression of the effective stress parameter and the Bishop's effective stress at low saturation are successfully derived. Note that for the fully saturated case, Eq. (3.10) reduces to Terzaghi's classic expression at the grain-scale [24],

$$\bar{\sigma} = \frac{1}{V} \sum_{\alpha=1}^{N^s} \text{sym}(f^\alpha \otimes l^\alpha) + P_f \mathbf{1} = \sigma' + P_f \mathbf{1} \quad (3.15)$$

where P_f is the pore water pressure in fully saturated media.

Numerical simulation of 2D capillary bridges

The calculation of inter-particle contact forces using Eq. (3.3), Eq. (3.4), and Eq. (3.9) requires tracking the shape and pressure P_f^j of pore fluid. In a partially saturated granular system, the geometrical shape of pore fluid depends on the pore structure, saturation, gravity, surface energy of the contact surfaces of different phases, etc [31, 32]. The complex shape of fluid clusters increases the difficulty of observation and tracking of unsaturated granular packing at the grain-scale. However, in the case of large particles and low saturation $S_r \ll 1$, pore fluid would form capillary bridges between solid grains in order to minimize its surface energy. For solid particles with high roundness and smooth surfaces, these capillary bridges can be assumed to be axisymmetric.

The shape of the 2D capillary bridge (fluid cluster j) between two disks can be described using the well-known Young-Laplace equation [33],

$$\Delta P = -\gamma \nabla \cdot \hat{\mathbf{n}} = -2\gamma H_f \quad (3.16)$$

where ΔP is the pressure difference across the interface ($\Delta P = P_a - P_f^j$), γ is the surface tension, $\hat{\mathbf{n}}$ is the unit outward normal of the surface, H_f is the mean curvature of the surface ($H_f = 1/2R$ for 2D capillary bridges, R is the radius of curvature).

As shown in Fig. 3.2a, a drop of water from a capillary bridge between two rigid disks. In the absence of gravity, knowing the material properties, geometry, and separation distance of the disks, the lateral width w of the capillary bridge can

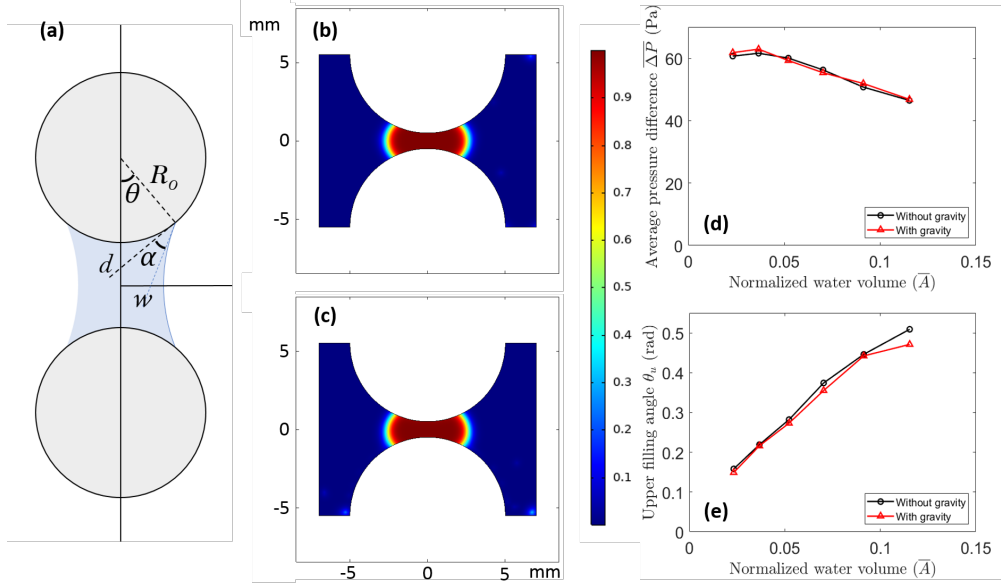


Figure 3.3: 2D finite element simulation (FEM) of capillary bridges between two disks. (a) Schematic of a 2D capillary bridge between two disks. (b) FEM simulation result of the geometry of a static capillary bridge in the absence of gravity. The colormap represents the area fraction of water (red for the water phase, blue for the air phase). (c) FEM simulation result of the geometry of a static capillary bridge in the presence of gravity. (d) The average pressure difference $\Delta\bar{P} = P_a - \bar{P}_f^j$ with and without the influence of gravity as a function of normalized water volume \bar{A} . (e) The filling angle of the upper disk θ_u with and without the influence of gravity as a function of normalized water volume \bar{A} .

be determined knowing the filling angle θ , the contact angle α , and the water-air pressure difference ΔP .

$$w = R_0 \sin\theta + \frac{\gamma}{\Delta P} \{ \sin(\theta + \alpha) - 1 \} \quad (3.17)$$

where R_0 is the radius of the solid disk. The capillary area A (or volume V for 3D), can be written as the following equation:

$$A = 2 \sin\theta (R_0 + d) R_0 - \left(\frac{1}{2} \sin 2\theta + \theta \right) R_0^2 + \left\{ \frac{1}{4} \sin(\theta + \alpha) - \frac{\pi}{2} + \theta + \alpha \right\} \left(\frac{\gamma}{\Delta P} \right)^2 \quad (3.18)$$

The capillary force is then represented by the sum of the axial surface tension and hydrostatic force at the neck of the capillary bridge,

$$F = 2w\Delta P + 2\gamma = 2R_0\sin\theta\Delta P + 2\sin(\theta + \alpha)\gamma. \quad (3.19)$$

While the analytical solution of a static capillary bridge is relatively concise in the absence of gravity, finite element simulation (FEM) is needed to solve the shape of a static capillary bridge in the presence of gravity. The FEM analysis is carried out using the separated multiphase flow models of COMSOL Multiphysics simulation tool [34]. The solid disks with radius $R_0 = 5\text{mm}$ are treated as walls with no-slip boundary conditions. During the formation of the capillary bridge, the water cluster will wet the wall with a constant contact angle. Fig. 3.3b and Fig. 3.3c display two of the FEM simulation results for a static bridge with initial filling angle $\theta_0 = 30^\circ$ and a contact angle $\alpha = 70^\circ$ with and without the influence of gravity. While the menisci contours of the capillary bridge in the absence of gravity have constant curvature, the contours distort slightly under gravity, as expected. To further analyze the effect of gravity on the shape and hydrostatic pressure of capillary bridges, the average pressure difference $\bar{\Delta P}$ and the filling angle of the upper disk θ_u are plotted separately in Fig. 3.3d and 3.3e as a function of the normalized water volume \bar{A} . The results indicate that for a small water cluster with volume $A \ll A_0 = \pi R_0^2$ (Area of the disk) forms a capillary bridge in a narrow gap between two disks, the surface distortion and pressure variation caused by gravity can be neglected.

Granular element method for partially saturated granular media

The granular element method (GEM) was originally developed for determining inter-particle forces in dry granular media [22, 23] and was also has been used to analyze fully saturated media [24]. Knowing the geometry of water clusters under low saturation condition, the granular element method for partially saturated systems is developed based on Eqs. (3.3), (3.4), and (3.9). While the GEM for dry and fully saturated granular media is already well-developed, modifications are needed in the presence of both pore fluid and pore gas. In quasi-static state, the 2D balance of forces, Eq. (3.3) and moments, Eq. (3.4) can be represented in matrix form:

$$\mathbf{K}_{eq}\mathbf{f} = \mathbf{b}_{eq} \quad (3.20)$$

$$\mathbf{K}_{eq} = \begin{matrix} & & p & & q & & \\ & & & & & & \\ & & & & & & \\ i & \begin{bmatrix} \ddots & \mathbf{0} & \dots & \mathbf{0} & \dots \\ \mathbf{0} & \mathbf{K}_{eq}^p & \mathbf{0} & \mathbf{K}_{eq}^q & \mathbf{0} \\ \vdots & \mathbf{0} & \ddots & \mathbf{0} & \vdots \\ \mathbf{0} & -\mathbf{K}_{eq}^p & \mathbf{0} & \mathbf{0} & \mathbf{0} \\ \vdots & \mathbf{0} & \vdots & \mathbf{0} & \ddots \end{bmatrix} & & & \\ j & & & & & & \\ & & & & & & \end{matrix} \quad \mathbf{K}_{eq}^p = \begin{bmatrix} 1 & 0 \\ 0 & 1 \\ -x_2^p & x_1^p \end{bmatrix}$$

$$\mathbf{f}^p = \begin{pmatrix} f_1^p \\ f_2^p \end{pmatrix} \quad \mathbf{b}_{eq}^p = \begin{pmatrix} -\sum_{\beta=1}^{N_i^f} (\int_{S_i^\beta} \Delta P^\beta \hat{\mathbf{n}} dS + \int_{L_i^\beta} \boldsymbol{\gamma}^\beta dL) \\ -\sum_{\beta=1}^{N_i^f} (\int_{S_i^\beta} \Delta P^\beta \|\mathbf{x}^\beta \times \hat{\mathbf{n}}\| dS + \int_{L_i^\beta} \|\mathbf{x}^\beta \times \boldsymbol{\gamma}^\beta\| dL) \end{pmatrix}$$

where i and j represent particles, p and q represent particle–particle and particle–boundary contacts separately. Matrix \mathbf{K}_{eq} has $3N$ rows and N^s columns, contact force vector \mathbf{f} has $2N$ rows, and vector \mathbf{b}_{eq} has $3N$ rows. Assuming the solid-fluid contact region S_i^β is small in the low saturation condition, \mathbf{b}_{eq}^p becomes the following term:

$$\mathbf{b}_{eq}^p = \begin{pmatrix} -\sum_{\beta=1}^{N_i^f} (\Delta P^\beta S_i^\beta + \gamma \sin \alpha L_i^\beta) \bar{\mathbf{n}} \\ -\sum_{\beta=1}^{N_i^f} (\Delta P^\beta S_i^\beta + \gamma \sin \alpha L_i^\beta) \|\bar{\mathbf{x}}^\beta \times \bar{\mathbf{n}}\| \end{pmatrix} \quad (3.21)$$

where $\bar{\mathbf{n}}$ is the average normal vector of the solid-fluid contact surface S_i^β (contact line for 2D), $\bar{\mathbf{x}}^\beta$ is a vector from the origin to the center of S_i^β and α is the solid-fluid contact angle.

The expression of average Cauchy stress for particles in equilibrium (Eq. (3.9)) also has a corresponding matrix form:

$$\mathbf{K}_{st} \mathbf{f} = \mathbf{b}_{st} \quad (3.22)$$

$$\mathbf{K}_{st} = \begin{matrix} & & p & & q & & \\ & & & & & & \\ & & & & & & \\ i & \begin{bmatrix} \ddots & \mathbf{0} & \dots & \mathbf{0} & \dots \\ \mathbf{0} & \mathbf{K}_{st}^p & \mathbf{0} & \mathbf{K}_{st}^q & \mathbf{0} \\ \vdots & \mathbf{0} & \ddots & \mathbf{0} & \vdots \\ \mathbf{0} & -\mathbf{K}_{st}^p & \mathbf{0} & \mathbf{0} & \mathbf{0} \\ \vdots & \mathbf{0} & \vdots & \mathbf{0} & \ddots \end{bmatrix} & & & & \\ j & & & & & & \\ & & & & & & \end{matrix} \quad \mathbf{K}_{st}^p = \begin{bmatrix} x_1^p & 0 \\ 0 & x_2^p \\ x_2^p & x_1^p \end{bmatrix}$$

$$\mathbf{f}^p = \begin{pmatrix} f_1^p \\ f_2^p \end{pmatrix} \quad \mathbf{b}_{st}^p = \begin{pmatrix} \Omega_i \bar{\sigma}_{11}^i + \sum_{\beta=1}^{N_i^f} (\Delta P^\beta S_i^\beta + \gamma \sin \alpha L_i^\beta) \bar{n}_1 \bar{x}_1^\beta - \Omega_i P_a \\ \Omega_i \bar{\sigma}_{22}^i + \sum_{\beta=1}^{N_i^f} (\Delta P^\beta S_i^\beta + \gamma \sin \alpha L_i^\beta) \bar{n}_2 \bar{x}_2^\beta - \Omega_i P_a \\ 2\Omega_i \bar{\sigma}_{12}^i + \sum_{\beta=1}^{N_i^f} (\Delta P^\beta S_i^\beta + \gamma \sin \alpha L_i^\beta) (\bar{n}_2 \bar{x}_1^\beta + \bar{n}_1 \bar{x}_2^\beta) \end{pmatrix}$$

where Ω_i is the area of the 2D particle i . Similar to matrix \mathbf{K}_{eq} , the matrix \mathbf{K}_{st} has $3N$ rows and N^s columns and vector \mathbf{b}_{st} has $3N$ rows. Besides the equations of equilibrium and average Cauchy stress, the contact forces of cohesionless granular materials are also governed by the Coulomb friction law:

$$\begin{aligned} -\mathbf{n}^p \mathbf{f}^p &\geq 0 \\ -(\mathbf{n}^p + \frac{1}{\mu} \mathbf{t}^p) \mathbf{f}^p &\geq 0 \\ -(\mathbf{n}^p - \frac{1}{\mu} \mathbf{t}^p) \mathbf{f}^p &\geq 0 \end{aligned} \quad (3.23)$$

where \mathbf{n}^p and \mathbf{t}^p represent normal and tangential unit vectors at the contact point p for a particular particle Ω_i . μ is the Coulomb friction coefficient. Similarly, Eq. (3.23) can also be written in a corresponding matrix form:

$$\mathbf{B}\mathbf{f} \geq \mathbf{0} \quad (3.24)$$

$$\mathbf{B} = \begin{matrix} & \begin{matrix} p & p & & q & q \end{matrix} \\ \begin{matrix} p \\ \vdots \\ q \\ p \\ \vdots \\ q \\ p \\ \vdots \\ q \end{matrix} & \left[\begin{array}{cccccc} -n_1^p & -n_2^p & 0 & 0 & 0 \\ 0 & 0 & \ddots & 0 & 0 \\ 0 & 0 & 0 & -n_1^q & -n_2^q \\ -n_1^p - \frac{1}{\mu}t_1^p & -n_2^p - \frac{1}{\mu}t_2^p & 0 & 0 & 0 \\ 0 & 0 & \ddots & 0 & 0 \\ 0 & 0 & 0 & -n_1^q + \frac{1}{\mu}t_1^q & -n_2^q + \frac{1}{\mu}t_2^q \\ -n_1^p - \frac{1}{\mu}t_1^p & -n_2^p - \frac{1}{\mu}t_2^p & 0 & 0 & 0 \\ 0 & 0 & \ddots & 0 & 0 \\ 0 & 0 & 0 & -n_1^q + \frac{1}{\mu}t_1^q & -n_2^q + \frac{1}{\mu}t_2^q \end{array} \right] \end{matrix} \quad \mathbf{f} = \begin{pmatrix} f_1^p \\ f_2^p \\ \vdots \\ f_1^q \\ f_2^q \end{pmatrix}$$

Equations (3.20)-(3.22), and constraints Eq. (3.24) are the three sets of governing equations for the unsaturated GEM. Using these equations to solve solid contact force \mathbf{f} requires measurement of the entries in matrix \mathbf{K}_{eq} , \mathbf{K}_{st} , \mathbf{B} , as well as vectors \mathbf{b}_{eq} and \mathbf{b}_{st} . The contact locations and normal and tangent vectors at each contact point (or average normal vectors at each contact surface) can be determined by tracking the solid particles and fluid clusters. The average stress within each particle can be determined using the strain field in the particle. The pore gas pressure can be measured and the pore fluid pressure of the fluid clusters is calculated using the Young-Laplace equation (Eq. 3.16).

Theory of the classic 1D consolidation

Based on Terzaghi's theory for saturated soils, several research works carried out by Fredlund and others have provided a practical framework for unsaturated soil consolidation [11, 12]. In this section, a 1D consolidation model first developed by Fredlund and Hasan [12] is introduced. The three essential assumptions of the consolidation model are: *i*) the air phase is continuous; *ii*) the temperature, the coefficients of permeability of water and air, and the bulk moduli remain constant during the transient processes, and *iii*) the effects of air diffusing through water and water vapor movement are ignored.

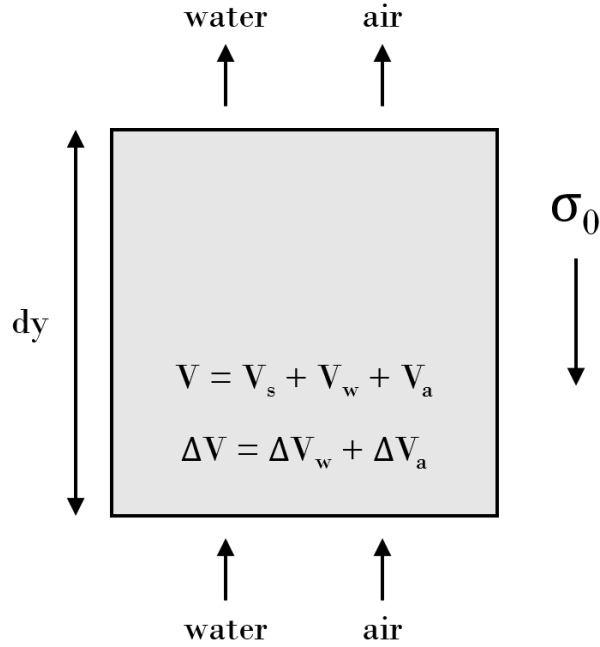


Figure 3.4: Schematic of a soil element with volume V and length dy under 1D consolidation.

Dissipation of excess pore water and pore air pressure will occur when an external load σ_0 is applied to an unsaturated soil in the y direction. During this process, the governing equations of the consolidation process are the continuity of the water and air phases. For a soil element of volume V shown in Fig. 3.4, if the solid grains are incompressible, the volume change ΔV of the soil element can be written as:

$$\Delta V = \Delta V_w + \Delta V_a \quad (3.25)$$

$$dV_w = V\{\beta_1^w d(\sigma_0 - P_a) + \beta_2^w d(P_a - P_w)\} \quad (3.26)$$

$$dV_a = V\{\beta_1^a d(\sigma_0 - P_a) + \beta_2^a d(P_a - P_w)\} \quad (3.27)$$

where V_w and V_a are the volume change of the water/air phase respectively. β_1^w and β_1^a are the compressibility of the water/air phase when $P_a = P_w$, β_2^w and β_2^a are the compressibility of the water/air phase when $\sigma_0 = P_a$.

First, the flow of water in the granular system can be described using Darcy's law:

$$v_w = -\frac{k}{\nu} \frac{\partial P_w}{\partial y} \quad (3.28)$$

where v_w is the velocity of water, k is the permeability of water, ν is the dynamic viscosity of water, and y is distance in the consolidation direction. Therefore, combining Eq. (3.26) with Eq. (3.28), the net water flux in the soil element is:

$$\frac{\partial}{\partial t} \left(\frac{V_w}{V} \right) = \frac{\partial}{\partial t} \{ \beta_1^w (\sigma_0 - P_a) + \beta_2^w (P_a - P_w) \} = -\frac{k}{\nu} \frac{\partial^2 P_w}{\partial y^2}. \quad (3.29)$$

In the case of a constant external load σ_0 , Eq. (3.29) can be further simplified. The continuity equation of water can be written as a partial differential equation:

$$\begin{aligned} \frac{\partial P_w}{\partial t} &= -C^w \frac{\partial P_a}{\partial t} + c_v^w \frac{\partial^2 P_w}{\partial y^2} \\ C^w &= \frac{\beta_1^w}{\beta_2^w} - 1 \\ c_v^w &= \frac{k}{\nu \beta_2^w} \end{aligned} \quad (3.30)$$

where C^w is the interactive constant of the water phase, and c_v^w is the coefficient of consolidation of the water phase.

Similarly, for the air phase treated as an ideal gas, the flow of air is controlled by Fick's law in the following form:

$$J_a = -D \frac{\partial P_a}{\partial y} \quad (3.31)$$

where J_a is the mass rate of the airflow, and D is the coefficient related to permeability. The net airflow through the soil element V can then be derived as:

$$\frac{\partial}{\partial t} \left(\frac{V_a}{V} \right) = \frac{\partial}{\partial t} \{ \beta_1^a (\sigma_0 - P_a) + \beta_2^a (P_a - P_w) \} = \frac{\partial}{\partial t} \left(\frac{M_a}{\rho V} \right) \quad (3.32)$$

for an ideal gas, the density ρ is a function of absolute pore air pressure $P_a + P$, where P is the atmospheric air pressure.

$$\rho = \frac{M_a}{V_a} = \frac{m_a (P_a + P)}{R_g T} \quad (3.33)$$

where R_g is the ideal gas constant, T is the temperature, and m_a is the molecular weight of the air phase. The pore air mass M_a in element soil V can also be represented by the density of air ρ , the degree of saturation S_r , and the porosity ϕ :

$$M_a = \rho V_a = (1 - S_r)\phi\rho V. \quad (3.34)$$

With Eqs. (3.31), (3.33), and (3.34), Eq(3.32) can be rewritten as:

$$\begin{aligned} \frac{\partial}{\partial t}\left(\frac{V_a}{V}\right) &= \frac{\partial}{\partial t}\{\beta_1^a(\sigma_0 - P_a) + \beta_2^a(P_a - P_w)\} \\ &= -\frac{DR_gT}{m_a(P_a + P)}\frac{\partial^2 P_a}{\partial y^2} + \frac{(1 - S_r)\phi}{P_a + P}\frac{\partial P_a}{\partial t}. \end{aligned} \quad (3.35)$$

The partial differential form of Eq. (3.35) can then be written as follow:

$$\begin{aligned} \frac{\partial P_a}{\partial t} &= -C^a\frac{\partial P_w}{\partial t} + c_v^a\frac{\partial^2 P_a}{\partial y^2} \\ C^a &= \frac{(P_a + P)\beta_2^a}{(P_a + P)(\beta_1^a - \beta_2^a) + (1 - S_r)\phi} \\ c_v^a &= \frac{DR_gT}{m_a\{(P_a + P)(\beta_1^a - \beta_2^a) + (1 - S_r)\phi\}} \end{aligned} \quad (3.36)$$

where C^a is the interactive constant of the air phase, and c_v^a is the coefficient of consolidation of the air phase. The excess pore water pressure and excess pore air pressure can be calculated by numerically solving the two PDEs Eqs. (3.30) and (3.36) simultaneously.

3.3 Experiments

For the experimental study of a complex granular system containing solid, liquid, and air phases, a hybrid optical-mechanical approach capable of dealing with solid-liquid-air coupling is needed. In this section, the experimental device developed to measure inter-particle forces to directly measure effective stress under classic 1D consolidation using Eq. (3.10) is described.

Experimental setup

The experimental setup shown in Fig. 3.5a-e consists of a balancing weight as dead load, two CCD cameras (Nikon AF Nikkor 50mm (10 frames/s) and Tokina AT-X 100mm (10 frames/s)), a fiber optic illuminator (Cole-Parmer, Model 41500-50) with homemade diffuser, a pressure sensor (OMEGA PX309-015GV), a custom made valve (using PVC soft plastic tubing and 52100 alloy steel balls) for depressurization, and a container to hold a partially saturated and pressurized granular

packing.

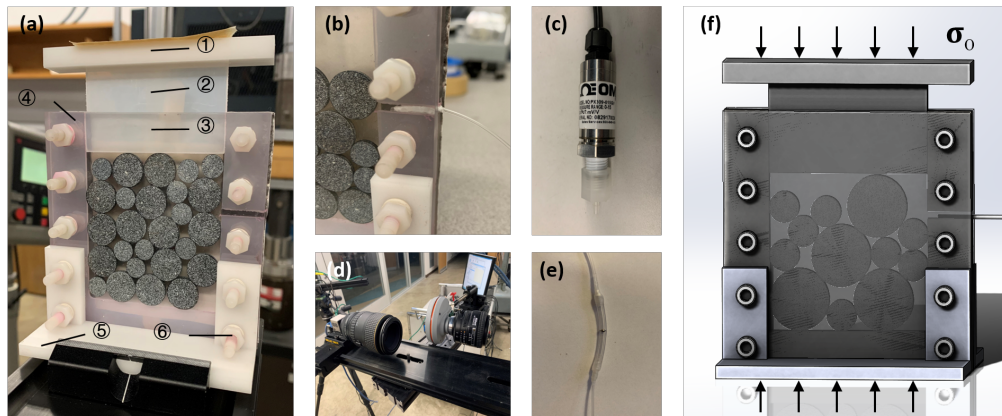


Figure 3.5: The experimental setup to validate the stress partition equation Eq. (3.10). (a) The container for partially saturated granular packing: 1. piston cap, 2. piston, 3. transparent window, 4. U-shaped sidewall, 5. support, 6. nylon screws, washers, and hex nuts. (b) EVA plastic tubing fixed in the gap on the side wall for pressurization and depressurization. (c) Pressure sensor to measure the pore air pressure. (d) CCD cameras to track the deformation of the grain skeleton and the geometry of pore water clusters. (e) Custom made valve for the depressurization process. (f) A simple illustration of the 1D consolidation experiment during which an external load σ_0 is applied to the granular system through the piston. The pore air depressurization is controlled with a custom made valve, while a pressure sensor is used to measure pore air pressure in real-time.

The container, as shown in Fig. 3.5a, includes two transparent windows, a U-shaped sidewall, a piston, a piston cap, and two supports. Polycarbonate plates (100mm x 100mm x 6.35mm) were used as transparent windows to facilitate optical imaging. The inner surface of the two windows was coated with hydrophobic ceramic spray to prevent pore water from infiltrating into the gap between the particles and the window. The side wall was machined out of white UHMW polyethylene plates. The piston, the piston cap, and the supports were made of Delrin. Additionally, nylon socket head screws were used to hold all the parts together. In order to seal the experiment setup during pressurization, grease and sealing tapes were applied to the piston and side walls.

The schematic of the one-dimensional consolidation experiment is depicted in Fig. 3.5f. While particles are confined in the container, a dead load σ_0 is applied through the piston to the granular system, resulting in an excess pore air pressure. During the consolidation process, the start of the depressurization of the pore air phase is

controlled by the custom made valve (Fig. 3.5e). The pore air pressure is measured by the pressure sensor (Fig. 3.5c) that connects to the container using an EVA plastic tubing (Fig. 3.5b). In addition, the deformation of the particles and geometry of the fluid clusters are tracked using CCD cameras (Fig. 3.5d). The particle strain field is therefore computed using digital image correlation analysis (DIC), and the pore fluid pressure is calculated using the Young-Laplace equation (Eq. 3.16), which will be discussed in the following section.

The particles of the granular packings studied in the experiments consist of soft neoprene rubber disks with two different sizes (Fig. 3.5a). These disk-shaped particles are assumed to be linear elastic and incompressible (Poisson's ratio ≈ 0.5) with Young's modulus E measured to be 0.8 MPa. Additionally, the Coulomb friction coefficient was determined to be $\mu \approx 0.4$ after wetting. The water contact angle α of both large and small particles is measured to be around 70° . The granular packings used in the experiments contain 12-13 large particles (diameter = 15 mm, thickness = 1.5 mm) and 10-12 small particles (diameter = 9.5 mm, thickness = 1.5 mm). To create an appropriate grayscale pattern for DIC analysis [35], white multi-surface paint was sprayed on all the rubber disks to generate speckle patterns. DIC analysis was performed using the xyz code [36].

Tracking and analysis of fluid clusters

The fluid used in the experiment is water stained with carmine red dye. After the particles are placed in the container, the dyed water is slowly injected into the granular packing using a syringe and a flexible thin needle. The position and geometry of the water clusters at each time point are recorded with a color CCD camera (Nikon AF Nikkor 50mm). The precise geometry and contour of the water clusters are further extracted using a Matlab color threshold program. The image data from the two cameras are combined by pairing the four corners of the imaging area. While the position and geometry of the solid disks are determined by DIC, the solid-water contact surfaces on a particle can be found by choosing a proper distance threshold R^* ($R_0 < R^* < 1.05R_0$, R_0 is the radius of the solid disk). As shown in Fig. 3.6, for a solid particle i , if the distance between the centroid of i and any point on the contour of water cluster j is smaller than the threshold R^* , then the particle i is considered to be in contact with water cluster j . All the points on the contour of water cluster j that fall in this threshold form the solid-water contact surface S_i^β . Therefore, the corresponding filling angle θ_i^β as well as the average normal vector \bar{n} can be easily computed using Matlab. Similarly, the boundary-water contact

surfaces can be determined by choosing another boundary distance threshold R_b^* ($0 < R_b^* < 0.08R_0$).

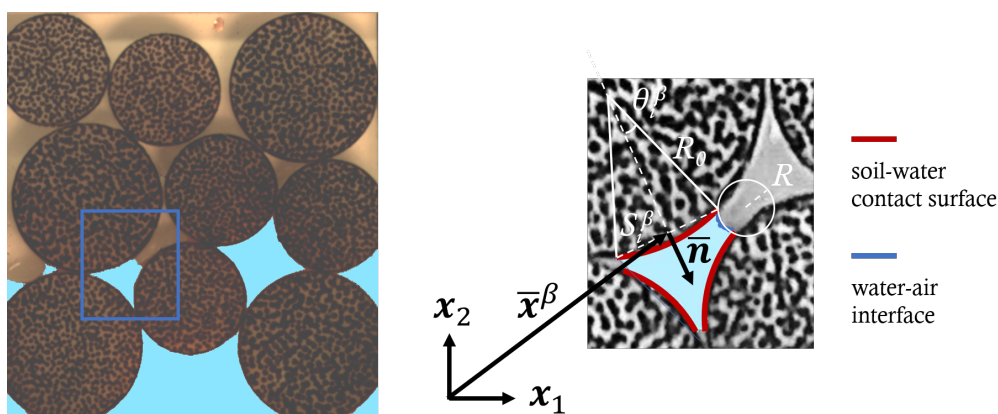


Figure 3.6: Schematic of finding the average curvature H_f , average normal vector \bar{n} , and fluid-gas pressure difference ΔP^β at a fluid-gas contact surface of fluid cluster ω_j .

After finding the solid-water contact surfaces, the water-air interfaces of the water cluster j are segments on its contour that do not belong to a solid-water contact surface or a boundary-water contact surface. While there may be multiple water-air interfaces on water cluster j that could be used to calculate the pressure difference ΔP^β , for the precision of computation, only the longest contour segment (largest distance between the two endpoints) is utilized here. The two endpoints of the segment as well as the point on the contour segment that is closest to the midpoint of the two endpoints are chosen. The radius of curvature R is then calculated by fitting a circle using these three points. Finally, the water surface tension γ is assumed to be constant throughout the experiments, and the pressure difference ΔP^β is calculated using the Young-Laplace equation (Eq. (3.16)).

3.4 Results and Discussion

In order to investigate the partition of applied stress among different phases (solid, fluid, gas) (Eq. (10)), classic 1D consolidation experiments were carried out using the hybrid optical-mechanical experimental setup described in section 3. Similar to the derivation in section 3.2, with the assumption of small solid-water contact surface under low saturation condition, Eq. (3.10) for 2D granular system under 1D consolidation can be further simplified:

$$\sigma = \sigma' + (1 - \phi^f)P_a + \phi^f \bar{P}_f + W_{yy} \quad (3.37)$$

$$W_{yy} = -\frac{1}{\Omega} \sum_{\beta=1}^{N^f} R^\beta (\gamma \sin \alpha L_\beta + \Delta P^\beta S_\beta) (\bar{\mathbf{n}} \otimes \bar{\mathbf{n}})_{yy}$$

where \bar{P}_f is the average pore water pressure. At the beginning of consolidation, a granular packing is confined in the container (Figure 3.6f), and as mentioned in section 3.3, a dead load corresponding to a nominal applied stress, $\sigma_0 = 4.4$ kPa is applied to the piston in the vertical direction and is balanced by the pore air, $(1 - \phi^f)P_a$ and pore water $\phi^f \bar{P}_f + W_{yy}$, and the effective stress, σ' . During the 1D consolidation process, the air phase gradually depressurizes (the pore water pressure decrease at the same time), the external load gradually shifts to the granular skeleton, and the effective stress, σ' , increases. At the point of full consolidation, the applied load is entirely transferred through the solid phase ($\sigma' \approx \sigma_0$ for low saturation systems $\phi^f \ll 1$). Utilizing the optical-mechanical approach, the inter-particle forces are tracked using GEM (direct measurement of σ') and the geometry as well as pore pressure of the water clusters at each time point, which are the components of four terms on the right hand side of Eq. (3.37). Therefore, the total stress σ can be computed employing the stress partition equation at grain-scale at any time point throughout the consolidation process.

The granular element method (GEM) for partially saturated granular packing in section 3.2 is used to calculate the inter-particle contact forces. In the consolidation process, the images of the granular system are captured using the CCD cameras. Matlab-based codes are used to analyze the image data and track the location and geometry of solid disks as well as the water clusters. While in-plane (2D) strain distribution within each particle is computed using digital image correlation (DIC), the average stresses are then calculated knowing the constitutive relation of the material of the particles. Using the method described in section 3.3, the hydrostatic pressure of each pore water cluster is calculated with the Young-Laplace equation (Eq. (3.16)). Neglecting gravity, the menisci of the water-air interfaces are assumed to have constant curvatures, which can be computed by fitting circular arcs to the points on the interfaces. The water-air surface tension is considered to be constant with $\gamma = 72$ mN/m. Finally, for 2D disk-shaped particles, the average normal vector at a solid-water interface is the unit vector perpendicular to the chord corresponding to the contact arc of the solid particle and water cluster. Thus, the solid-solid contact

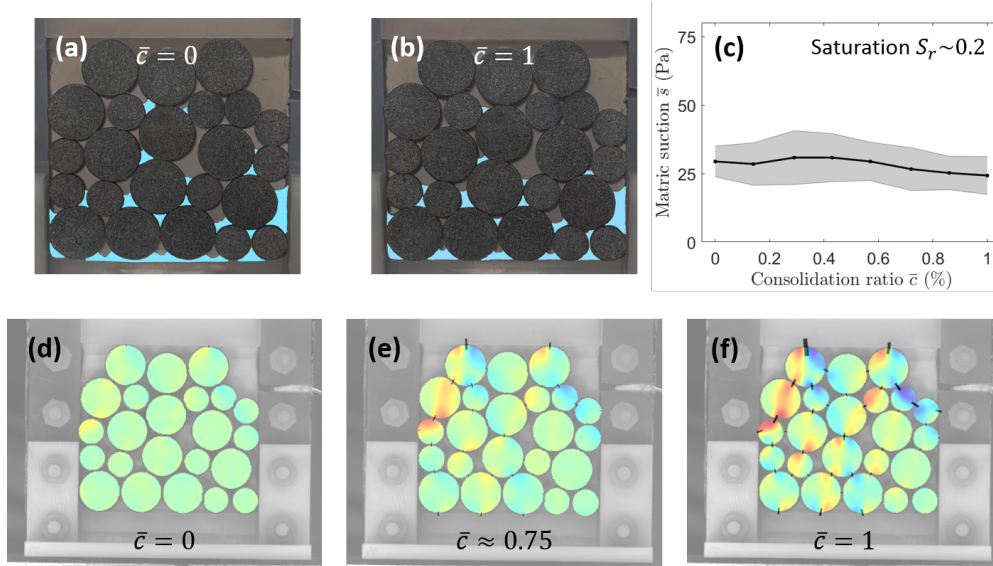


Figure 3.7: The position and geometry of water clusters, matric suction, and force chains measured in 1D consolidation experiments. (a) Water clusters (blue regions) tracked with CCD camera and the color threshold program of a granular packing at the beginning of the consolidation process, $\bar{c} = 0$, where \bar{c} is the consolidation ratio. (b) Water clusters of the same granular packing at the end of the consolidation process, $\bar{c} = 1$. (c) Average matric suction \bar{s} as a function of the consolidation ratio \bar{c} . The result is calculated from three different configurations with an average saturation S_r near 0.2. (d) Inter-particle force chains calculated using the unsaturated GEM of the same granular packing at the beginning consolidation $\bar{c} = 0$. Different colors correspond to shear strain ε_{xy}^i distribution in each particle. The black lines represent the direction and magnitude of particle-particle contact forces. (e) Inter-particle force chains calculated of the same granular packing at consolidation ratio $\bar{c} = 0.75$. (f) Inter-particle force chains of the same granular packing at the end of consolidation $\bar{c} = 1$.

forces \mathbf{f} are measured by solving for the least square solution that best satisfies Eqs. (3.20)-(3.22), and constraints Eq. (3.24).

The distribution of the water clusters in a granular system before and after consolidation is shown in Fig. 3.7a and b. Note that the consolidation ratio \bar{c} is the ratio between the current deformation over the total deformation after the consolidation process. The contours of the water clusters are captured, and the geometry of the water clusters as well as the saturation does not change significantly after the consolidation. The average saturation of three different granular systems is near 0.2. One thing to be observed in Figs. 3.7a and b is that the saturation (or water fraction) is not constant throughout the granular packing. Due to the effect of gravity and vaporization, the top layer of the granular system would have extremely low

saturation ($S_r \sim 0$), while the bottom layer may be considered near fully saturated ($S_r \sim 1$). However, the behavior of the granular system is still governed by the thick middle layer, which has a low saturation $S_r < 0.2$. Figure 3.7c shows the average matric suction calculated from the geometry (contours) of the water clusters in three different configurations at different consolidation ratios. The matric suction is around 30 Pa throughout the consolidation process. This is consistent with the SSCC curve, as the saturation is constant for small deformation in the absence of water flow. The development of the interparticle forces in a granular system through the 1D consolidation process is depicted in Figs. 3.7d-f. The distribution of in-plane shear strain ε_{xy}^i is shown on each particle i , while solid lines show how the external load is transferred to the walls of the container through the granular skeleton. It is clearly shown that as the pore air is depressurized, the stresses and contact forces within the granular skeleton increase.

The results of 1D consolidation experiments are shown in Fig. 3.8. The data from three different particle configurations (saturation S_r near 0.2 for different configurations) are plotted as a function of the consolidation ratio \bar{c} . The total stress σ , stress related to pore air $(1 - \phi^f)P_a$ and pore water $(\phi^f \bar{P}_f + W_{yy})$, as well as the effective stress σ' (Eq. (3.37)) are normalized by the external load σ_0 . It is clear that as the consolidation ratio increases, the excess pore air pressure and excess pore water pressure decrease as a result of depressurization. At the beginning of the consolidation process, the imposed stress (grey straight line in Fig. 3.8), which is defined as total stress excluding the stress due to the friction of the piston, is carried by the pore water and pore air. Stress starts to transfer through the solid skeleton as the consolidation gradually progresses. The solid phase shares half the load with a saturation ratio of around 78%. Eventually, at the end of the consolidation process, the granular system is fully depressurized and almost all the imposed stress is balanced by inter-particle contact forces through the solid network. Throughout the consolidation process, the total stress σ is nearly constant and in good agreement with the total (imposed) stress as suggested by the stress partition equation, Eqs. (3.10) and (3.34).

An important thing to note in Fig. 3.8 is that the total stress σ is slightly smaller than the imposed stress for the consolidation ratio \bar{c} less than 80%. This is most likely due to the thin PVC tube, which connects the container, the valve, and the pressure sensor, used for depressurization. According to the experimental data and classic 1D consolidation model [12], the rate of deformation is large when the

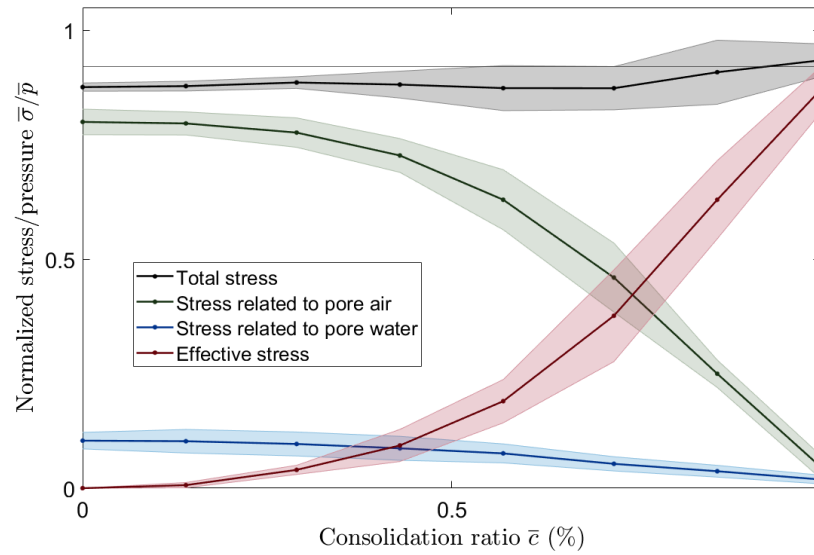


Figure 3.8: The evolution of the total stress σ , the stress term related to pore air $(1 - \phi^f)P_a$, the stress term related to pore water $\phi^f P_f + W_{yy}$, and the effective stress σ' as a function of the consolidation ratio \bar{c} . The shaded area represents the standard deviation of the stress/pressure obtained from three different experiments with different configurations. The solid straight line represents the imposed stress. The results are normalized by the external load σ_0 .

consolidation ratio is small. Although the granular packing inside the container can be assumed to be at quasi-static state, the large displacement rate would generate considerable airflow inside the thin tube. Due to the resistance of the tube airflow, there would be a pressure drop between the container and the pressure sensor. It is also noted that the effective stress σ' remains zero for a low consolidation ratio. This is partly because of the lightweight particles used in the experiments. In the presence of capillary bridges, the particles may form loose assemblies without direct contact with the majority of nearby particles [37]. Therefore, relatively small displacements in the early consolidation stage are allowed to occur without inducing particle-particle contact forces. Finally, although the total stress σ obtained 1D consolidation experiment is consistent with the stress partition equation, Eq. (3.10), in a macro-scale granular system with low saturation, the mechanical behavior of the granular media is mainly determined by the mechanical behavior of the gas and solid phase. Future research at a smaller scale is needed to better illustrate the effect of pressure difference and surface tension (term W_{yy} in Eq. (3.37)) on the mechanical behavior of granular packing.

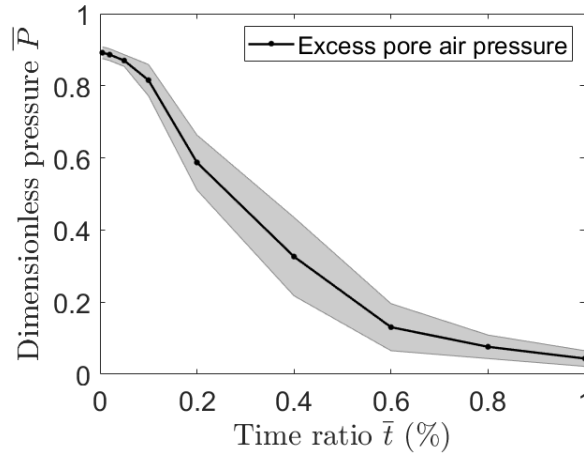


Figure 3.9: The evolution of the normalized excess pore air pressure P_a as a function of the consolidation time \bar{t} . The shaded area represents the standard deviation of the pressure obtained from three different experiments with different configurations. The results are normalized by the external load σ_0 .

In light of the 1D consolidation model developed by Fredlund and Hansan [12], the dependence of excess pore air pressure on consolidation time is considered and plotted in Fig. 3.9. The excess pore air pressure P_a is normalized by the external load σ_0 , and the time ratio \bar{t} is the ratio between the current time over the total time for the consolidation process. When the 1D consolidation begins, the valve is opened, and the excess pore air pressure drops fast. As the consolidation progresses, the pressure difference between the absolute pore air pressure ($P_a + P$) and the atmospheric pressure P decreases, causing the speed of depressurization to decrease as well. The pore air pressure is almost equal to atmospheric pressure at the end of consolidation as the external load σ_0 is shifted to the solid skeleton. It needs to be pointed out that the determination of the interactive constants and the coefficients of consolidation in Eqs. (3.30) and (3.36) in granular systems used in the experiments is difficult, which greatly increases the difficulty of a direct comparison between experimental data and the numerical solution of the 1D consolidation model presented in section 3.2. However, the time dependence found in Fig. 3.9 is consistent with that proposed in Fredlund and Hansan's model.

3.5 Conclusion

The stress partition of the total (applied) stress between various phases (solid, fluid, gas) in an unsaturated granular packing has been investigated. The overall contribution to stress in various phases has been linked to local quantities at grain-

scale, including inter-particle contact forces, interface energy, and capillary pressure. Analytical expressions have been derived, presented for the various components of stress, and also compared with Bishop's effective stress and Terzaghi's effective stress (section 3.2). In parallel, a hybrid optical-mechanical method based on DIC and GEM was developed to extract inter-particle forces in granular systems with low saturation. A method for imaging and computing the shape of water clusters was introduced. The hybrid optical-mechanical method was employed for the first time to directly measure how an external load imposed on the partially saturated granular system is shared between different phases in classic 1D consolidation. Through the 1D consolidation experiment, the stress partition equation (Eq. (3.10)) has been validated.

The effective stress of unsaturated granular systems obtained from the stress partition equation takes the same form as that of saturated systems [24]. However, unlike saturated systems, the pore pressure variance and surface tension induced by liquid clusters affect the particle contact forces and hence the effective stress under certain loading conditions. Different from many previous theoretical derivations [1], [10], [15], the stress partition equation Eq. (3.10) does not assume a uniform pore fluid pressure and is valid in the residual state. Besides, directly connected to grain-scale forces and pore pressures, the stress partition equation does not require the usage of an effective stress coefficient [10], an effective saturation [15], and parameters related to material properties in the two stress state method [12], which could be hard to evaluate. While the stress partition equation is under the assumption of low saturation, the equation reduces to Terzaghi's stress partition equation (Eq. (3.15)) in fully saturated cases [24].

Arising from the balance of moments and constraint relations, the unsaturated GEM provides a practical approach to quantify contact forces using the configuration and stress distribution in an unsaturated medium. As the experimental work in this article focuses on 2D granular systems under 1D consolidation at a low saturation ($S_r \sim 0.2$), the unsaturated GEM (section 3.2) methodology could also be applied to 3D unsaturated granular systems. In the case of 3D granular media, the particle average strain, as well as water cluster geometry, could be precisely measured through the digital volume correlation (DVC) and confocal microscopy, or XRCT and x-ray diffraction [17, 38]. Aside from the increase of dimension, the unsaturated GEM, consisting of both the granular kinetics and solid-fluid coupling, could also pave a new way for the experimental study of solid-fluid interactions of dynamic

capillary assemblies [39, 40]. In addition, works on asymmetric and multi-particle capillary bridges under gravity offer more insight into complex pore fluid geometry and capillary forces [41, 42]. These results could be applied to further analyze and simplify the expression of the governing matrix equations Eqs. (3.20)-(3.23) of complex unsaturated granular systems under a wide range of saturation S_r (for example, $S_r > 0.2$).

BIBLIOGRAPHY

- [1] D.G. Fredlund and H. Rahardjo. *Soil mechanics for unsaturated soils*. Wiley, 1993.
- [2] J.A. Izbicki, J. Radyk, and R.L. Michel. “Water movement through a thick unsaturated zone underlying an intermittent stream in the western Mojave Desert, southern California, USA”. In: *Journal of Hydrology* 238.3 (2000), pp. 194–217.
- [3] B.A. Ashtiani, R.E. Volker, and D.A. Lockington. “Tidal effects on groundwater dynamics in unconfined aquifers”. In: *Hydrological Processes* 15 (2001), pp. 655–669.
- [4] H.F. Zhao and L.M. Zhang. “Instability of saturated and unsaturated coarse granular soils”. In: *Journal of Geotechnical and Geoenvironmental Engineering* 140 (2014), pp. 25–35.
- [5] E. Cokca, O. Erol, and F. Armangil. “Effects of compaction moisture content on the shear strength of an unsaturated clay”. In: *Geotechnical and Geological Engineering* 22 (2004), pp. 285–297.
- [6] Y. Kim, H. Park, and S. Jeong. “Settlement Behavior of Shallow Foundations in Unsaturated Soils under Rainfall”. In: *Sustainability* 9.8 (2017), p. 1417.
- [7] M.B. Jamiolkowski. “The leaning tower of Pisa: end of an Odyssey”. In: *Proc. 15th ICSMGE, Istanbul, 2001* 4 (2001), pp. 2979–2996.
- [8] D.L. Presti, M. Jamiolkowski, and M. Pepe. “Geotechnical characterization of the subsoil of Pisa Tower”. In: *Characterisation and Engineering Properties of Natural Soils* 2 (2003), pp. 909–946.
- [9] K. Terzaghi. *Erdbaumechanik auf bodenphysikalischer Grundlage*. F. Deuticke, 1925.
- [10] A.W. Bishop. “The principle of effective stress”. In: *Teknisk Ukeblad* 39 (1959), pp. 859–863.
- [11] D.G. Fredlund and N.R. Morgenstern. “Stress state variables for unsaturated soils”. In: *Journal of the Geotechnical Engineering Division* 103.5 (1977), pp. 447–466.
- [12] D.G. Fredlund and J.U. Hasan. “One-dimensional consolidation theory: unsaturated soils”. In: *Canadian Geotechnical Journal* 16.3 (1979), pp. 521–531.
- [13] S.J. Wheeler and V. Sivakumar. “An elasto-plastic critical state framework for unsaturated soil”. In: *Géotechnique* 45.1 (1995), pp. 35–53.

- [14] D. Gallipoli, S.J. Wheeler, and M. Karstunen. “Modelling the variation of degree of saturation in a deformable unsaturated soil”. In: *Géotechnique* 53.1 (2003), pp. 105–112.
- [15] N. Lu, J.W. Godt, and D.T. Wu. “A closed-form equation for effective stress in unsaturated soil”. In: *Water Resources Research* 46.5 (2010).
- [16] A. Drescher and G. Jong. “Photoelastic verification of a mechanical model for the flow of a granular material”. In: *Soil Mechanics and Transport in Porous Media: Selected Works of G. de Josselin de Jong* (2006), pp. 28–43.
- [17] C. Liu et al. “Force fluctuations in bead packs”. In: *Science* 269.5223 (1995), pp. 513–515.
- [18] M. Saadatfar et al. “Mapping forces in a 3D elastic assembly of grains”. In: *Journal of the Mechanics and Physics of Solids* 60.1 (2012), pp. 55–66.
- [19] H.F. Poulsen. *Three-dimensional X-ray diffraction microscopy: mapping polycrystals and their dynamics*. Vol. 205. Springer Science & Business Media, 2004.
- [20] S.A. Hall et al. “Can intergranular force transmission be identified in sand? First results of spatially-resolved neutron and X-ray diffraction”. In: *Granular Matter* 13 (2011), pp. 251–254.
- [21] A. Kondo et al. “Visualization and measurement of load transmission in granular assemblies using mechanoluminescent-coated particles”. In: *Granular Matter* 21 (2019), pp. 1–12.
- [22] J.E. Andrade and R.I. Borja. “Modeling deformation banding in dense and loose fluid-saturated sands”. In: *Finite Elements in Analysis and Design* 43.5 (2007), pp. 361–383.
- [23] R. Hurley et al. “Extracting inter-particle forces in opaque granular materials: beyond photoelasticity”. In: *Journal of the Mechanics and Physics of Solids* 63 (2014), pp. 154–166.
- [24] J.E. Andrade et al. “Measuring Terzaghi’s effective stress by decoding force transmission in fluid-saturated granular media”. In: *Journal of the Mechanics and Physics of Solids* 165 (2022), p. 104912.
- [25] J.T. Davies. *Interfacial phenomena*. Elsevier, 2012.
- [26] G.T. Houlsby. “The work input to an unsaturated granular material”. In: *Géotechnique* 47.1 (1997), pp. 193–196.
- [27] A.E.H. Love. *A treatise on the mathematical theory of elasticity*. Cambridge University Press, 1927.
- [28] J. Christoffersen, M.M. Mehrabadi, and S. Nemat-Nasser. “A micromechanical description of granular material behavior”. In: *Journal of Applied Mechanics* 48 (1981), pp. 339–344.

- [29] B.A. Schrefler. “The finite element method in soil consolidation”. PhD thesis. University College of Swansea, 1984.
- [30] G.D. Aitchison. “Relationships of moisture stress and effective stress functions in unsaturated soils”. In: *Golden Jubilee of the International Society for Soil Mechanics and Foundation Engineering: Commemorative Volume*. Engineers Australia, 1985, pp. 20–25.
- [31] M.E.D. Urso, C.J. Lawrence, and M.J. Adams. “Pendular, funicular, and capillary bridges: results for two dimensions”. In: *Journal of Colloid and Interface Science* 220.1 (1999), pp. 42–56.
- [32] Y. Wang, S. Michielsen, and H.J. Lee. “Symmetric and asymmetric capillary bridges between a rough surface and a parallel surface”. In: *Langmuir* 29.35 (2013), pp. 11028–11037.
- [33] T. Young. “III. An essay on the cohesion of fluids”. In: *Philosophical Transactions of the Royal Society of London* 95 (1805), pp. 65–87.
- [34] COMSOL Multiphysics. “Introduction to COMSOL multiphysics®”. In: *COMSOL Multiphysics, Burlington, MA, accessed Feb 9 (1998)*, p. 2018.
- [35] H. Schreier, J.J. Orteu, and M.A. Sutton. *Image correlation for shape, motion and deformation measurements: Basic concepts, theory and applications*. Springer, 2009.
- [36] J. Blaber, B. Adair, and A. Antoniou. “Ncorr: open-source 2D digital image correlation matlab software”. In: *Experimental Mechanics* 55.6 (2015), pp. 1105–1122.
- [37] H. Louati, D. Oulahna, and A. de Ryck. “Apparent friction and cohesion of a partially wet granular material in steady-state shear”. In: *Powder Technology* 278 (2015), pp. 65–71.
- [38] R.C. Hurley et al. “Quantifying interparticle forces and heterogeneity in 3D granular materials”. In: *Physical Review Letters* 117.9 (2016), p. 098005.
- [39] K. Washino et al. “Normal viscous force of pendular liquid bridge between two relatively moving particles”. In: *Journal of Colloid and Interface Science* 494 (2017), pp. 255–265.
- [40] O. Pitois, P. Moucheront, and X. Chateau. “Liquid bridge between two moving spheres: an experimental study of viscosity effects”. In: *Journal of Colloid and Interface Science* 231.1 (2000), pp. 26–31.
- [41] T.P. Farmer and J.C. Bird. “Asymmetric capillary bridges between contacting spheres”. In: *Journal of Colloid and Interface Science* 454 (2015), pp. 192–199.
- [42] M. Miot et al. “Numerical analysis of capillary bridges and coalescence in a triplet of spheres”. In: *Granular Matter* 23.3 (2021), p. 65.

*Chapter 4***SUMMARY AND FUTURE WORK****4.1 Summary**

The thesis focused on unraveling the link between interparticle contact forces at grain-scale and the stress transfer at the macroscopic or continuum scale. The interparticle forces are directly measured, and effective stresses are determined in saturated and unsaturated granular systems. The grain-scale expressions of the stress in different media (solid, fluid, gas) are derived for both systems. Hybrid optical-mechanical approaches are developed for experimental validation of the theoretical results through classic 1D consolidation experiments.

In Chapter 2, the well-known Terzaghi's effective stress for fully saturated systems under consolidation is explored. Combining the additive decomposition of total stress with the equilibrium of moments, Terzaghi's effective stress can be represented using grain-scale properties (forces and branch vectors). Based on GEM, a hybrid optical-mechanical method is applied to measure interparticle forces in 1D consolidation of saturated 2D granular media. The 1D consolidation process is carried out with three different particle configurations. Through these experiments, the effective stress is calculated using measured inter-particle forces, and the summation of the effective stress and pore water pressure balanced the external stress applied to the granular systems. The grain-scale expression of Terzaghi's effective stress is thus validated for the first time. The settlement and pore water pressure measured through the experiments also compares well with those obtained from the 1D consolidation model.

In Chapter 3, the partition of stress is explored in more complex unsaturated granular systems. Under the assumption of low saturation ($S_r \ll 1$), the grain-scale expression of the stress partition equation is derived by applying the stress decomposition as well as the force and moment equilibrium. The influence of gravity on the geometry and pore pressure difference of the water capillary bridges are studied using 2D finite element method. The granular element method is also modified and the capillary forces are considered in the governing equations of GEM. The corresponding hybrid optical-mechanical approach is developed for 1D consolidation experiments. The values of the terms in the stress partition equation are computed

using grain-scale properties, and the grain-scale expression of the stress partition equation is validated through three separate experiments. Finally, the time variance of pore air pressure is considered and is in good agreement with the 1D consolidation model for unsaturated granular media.

4.2 Future Work

The methodology and results of the studies presented in this thesis suggest several new research directions. Some of these research areas are described in the following.

The effect of granular fabric on stress transfer

In Chapter 2, the contact force magnitude at different stages of the 1D consolidation process is plotted based on the corresponding branch vectors. The result shows that, as consolidation progress, the magnitudes of interparticle contact forces are larger at contact points (and corresponding particle) with branch vectors in the direction of the externally applied load. This relationship between magnitudes of the interparticle forces and branch vector orientations also indicates that the major share of elastic energy and solid skeleton stress transfer through the contact points with branch vectors parallel to the external load. While the three types of fabric vectors commonly used are particle orientation, contact normal, and branch vector [1, 2], GEM is capable of tracking and measuring particle deformation and motion in opaque systems with complex particle shapes [3]. Also, GEM can measure interparticle forces and compute the stress transfer through the grain skeleton. Therefore, GEM has the potential to probe the link between the grain-scale fabric and the constitutive behavior of the whole system.

Matric suction and stress partition of granular systems with different saturation

As mentioned in Chapter 3, the GEM for unsaturated granular systems is derived based on the assumption of low saturation ($S_r \sim 0.2$). Under this assumption, the pore air is connected with uniform pressure P_a , and the pressure variance with each pore fluid cluster can be neglected. For saturation level within the residue zone of the granular system, the water clusters can be further considered as toroidal-shaped capillary bridges [4]. While the pressure difference between pore water and pore air can be calculated by employing the Young-Laplace equation, the maximum suction stress of the granular system can be studied. Similarly, for systems with high saturation levels ($S_r \sim 1$), the pore water is connected, and the pore water pressure gradient is determined by gravity. In this case, the pressure within each pore air

domain (air bubble) is assumed to be constant. Besides, the mechanical influence of pore water pressure on a particle is the buoyancy acting on the particle. With the pressure difference between pore water and pore air calculated using the Young-Laplace equation, the governing equations of GEM can be written in a relatively concise form. Therefore, the stress partition and matric suction can be calculated for the near-saturated cases. However, things are much more complicated in the transition zone (say, $0.2 < S_r < 0.8$). In the transition zone, the distribution of pore water and pore air as well as the geometry of water-air interfaces can be exceedingly complex, making previous assumptions no longer valid. Extensive studies and research are needed to combine the governing equations of GEM on shape characterization of water meniscus in complex granular media [4–6].

Stress transfer in 3D granular systems

The theoretical framework GEM described in both Chapters 2 and 3 can be extended to 3D granular systems with arbitrary configuration. By employing the digital volume correlation (DVC) method [7], 3D GEM can be applied in the study of various mechanical phenomena ranging from point load to frictional failure. As GEM does not require specific grain material or particle shape, it can overcome the limitations of photoelasticity and X-ray tomography. Combined with confocal microscopy and other imaging techniques, GEM can be further applied to investigate interparticle forces and stress transfer of soft materials and even biomaterials at microscale, with due consideration for stress relaxation time and water vaporization, which need to be carefully considered and controlled.

BIBLIOGRAPHY

- [1] M.M. Mehrabadi, S. Nemat-Nasser, and M. Oda. “On statistical description of stress and fabric in granular materials”. In: *International Journal for Numerical and Analytical Methods in Geomechanics* 6.1 (1982), pp. 95–108.
- [2] S. Zhao et al. “Particle shape effects on fabric of granular random packing”. In: *Powder Technology* 310 (2017), pp. 175–186.
- [3] K.W. Lim, K. Krabbenhoft, and J.E. Andrade. “On the contact treatment of non-convex particles in the granular element method”. In: *Computational Particle Mechanics* 1 (2014), pp. 257–275.
- [4] J.A. Gili and E.E. Alonso. “Microstructural deformation mechanisms of unsaturated granular soils”. In: *International Journal for Numerical and Analytical Methods in Geomechanics* 26.5 (2002), pp. 433–468.
- [5] C.D. Willett et al. “Capillary bridges between two spherical bodies”. In: *Langmuir* 16.24 (2000), pp. 9396–9405.
- [6] S.D.N. Lourenço et al. “Formation and evolution of water menisci in unsaturated granular media”. In: *Géotechnique* 62.3 (2012), pp. 193–199.
- [7] B.K. Bay. “Methods and applications of digital volume correlation”. In: *The Journal of Strain Analysis for Engineering Design* 43.8 (2008), pp. 745–760.

Appendix A

RESULTS FOR SATURATED GRANULAR MEDIA

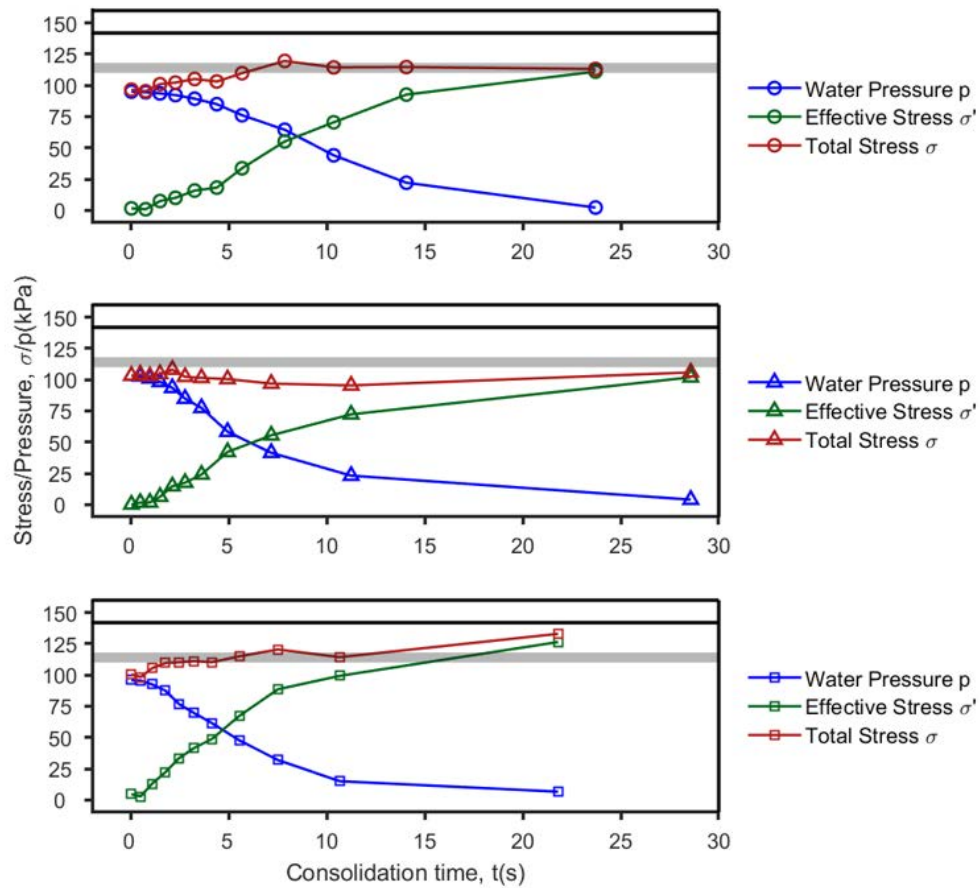


Figure A.1: Evolution of fluid pressure, effective stress, and their summation as a function of time for three different configurations of granular matter. Each symbol represents data gathered at a certain consolidation (time). Experimental results with the shaded region capturing the range of results for various configurations. The evolution of effective stress is calculated directly from the inter-particle forces obtained using GEM.

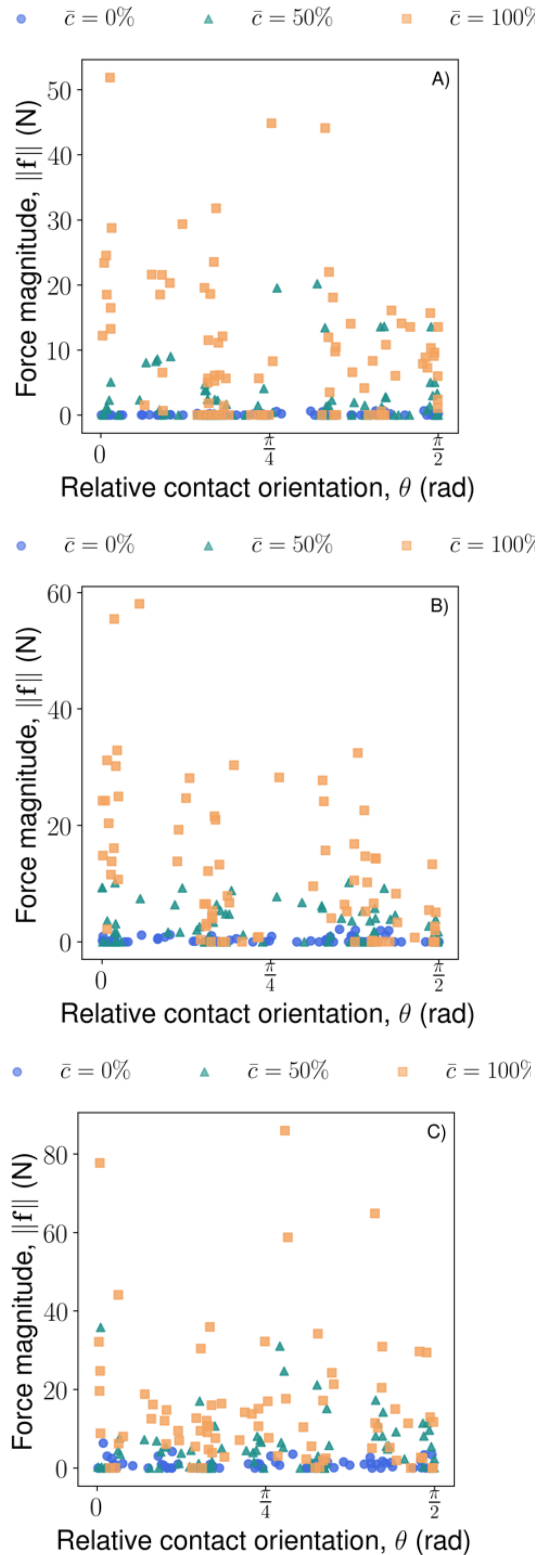


Figure A.2: Scatter plots of force magnitude and contact orientation relative to the direction of load application for experiments 1 (A), 2 (B), and 3(C), showing clear increases in magnitude of force as consolidation evolves, especially in the direction of loading ($\theta = 0$).

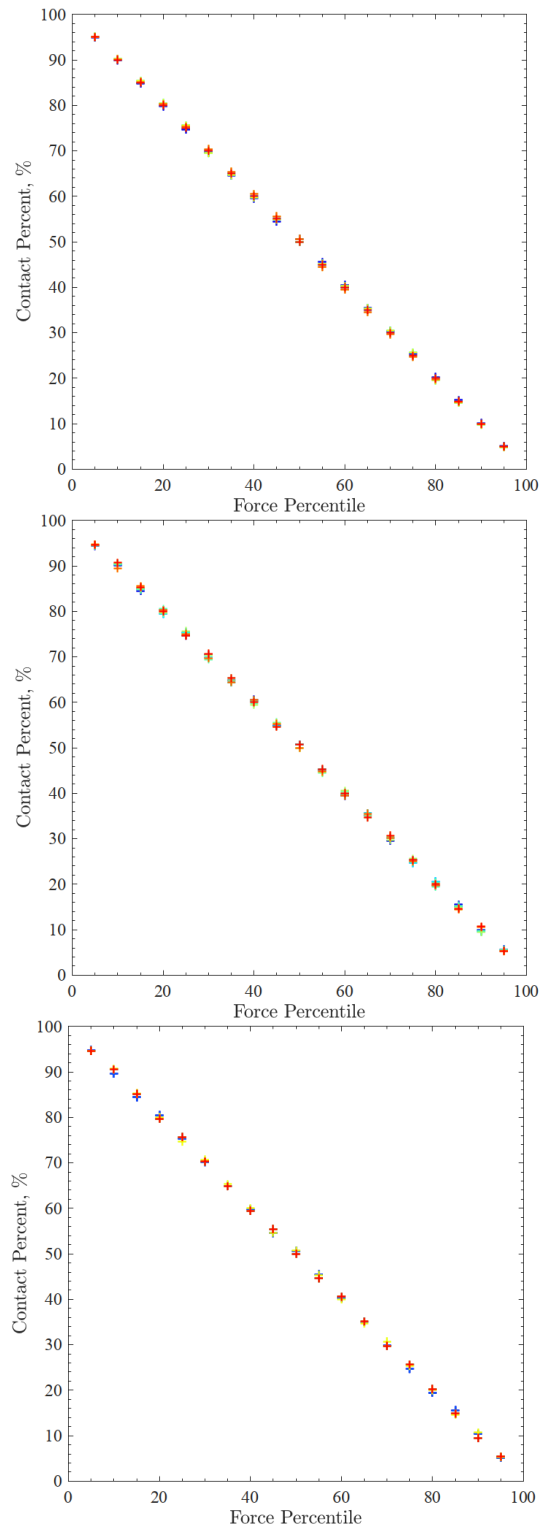


Figure A.3: Force percentiles and the contact percentage associated with those percentiles for experiments 1-3 (top-to-bottom). The data for each plot represents all the time-series for that experiment. For example, for experiment 3, the forces great than the 20th percentile are carried by about 80% of the contacts.

*Appendix B***EFFECTIVE MODULUS OF GRANULAR ASSEMBLY USING
DISCRETE ELEMENT SIMULATION**

We compared the fitted constrained Young's modulus for the drained solid skeleton with results from simulations. We built a computational model based on a variant of Discrete Element Method (DEM) that can capture arbitrarily shaped particles via their level sets – called Level Set Discrete Element Method (LS-DEM). The full description of LS-DEM can be found here ([ref to Kawamoto et al., JMPS 2016]). For our simulations, we directly imported the initial configuration for one of the packings as shown in Figure B.1 and applied a uniaxial displacement to the packing constrained by the box to determine its constrained modulus. The results are in good agreement with the values obtained from the experimental data. The simulations were run with coefficient of friction $\mu = 0.6$, density $\rho = 1250 \text{ kg m}^{-3}$, normal stiffness $k_n = 20,000 \text{ N/m}$, shear stiffness $k_s = 9,000 \text{ N/m}$ and total strain of 10 percent in the vertical directions while applying a no displacement boundary condition laterally. The application of the vertical strain is done in 5,000 time steps to ensure a quasi-static loading. The obtained constrained modulus is $\bar{E} = 4.061 \text{ MPa}$ which is in good agreement with those obtained from our hybrid experimental-mechanical setup.

Figure B.1: An example of LS-DEM simulations (left) with the imported initial configuration from the experiment (right).

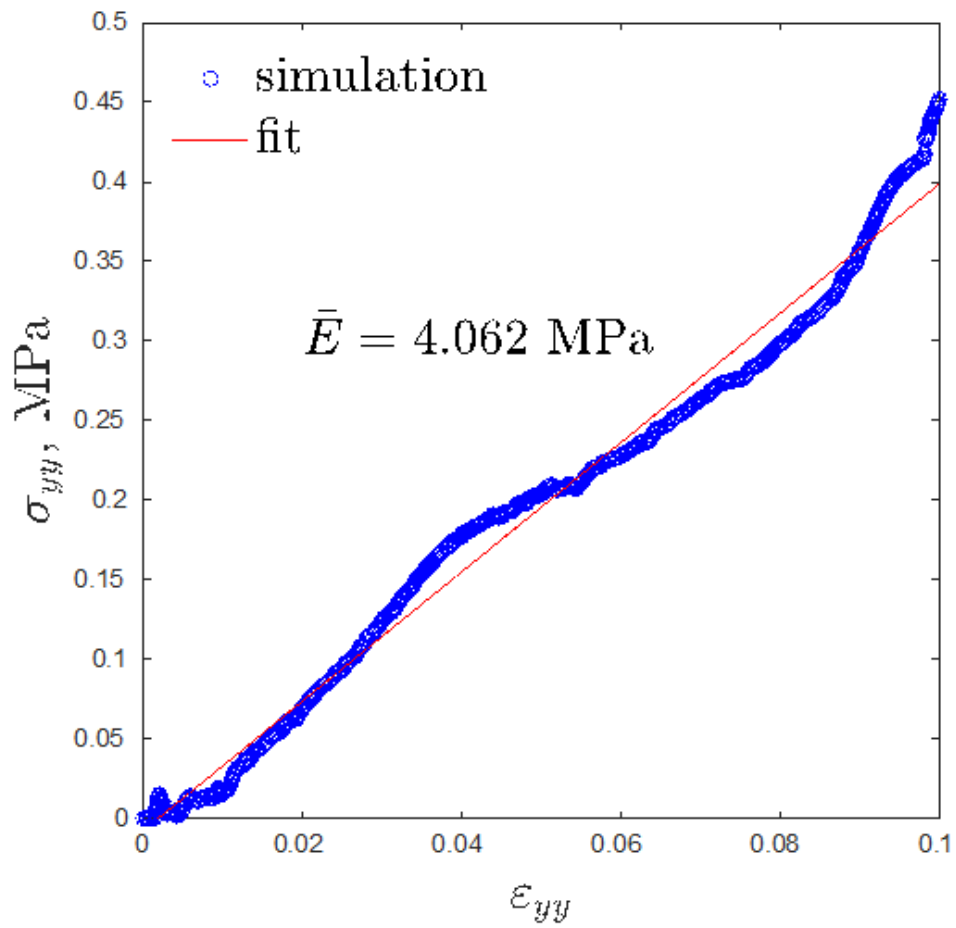


Figure B.2: The axial stress σ_{yy} vs. the axial strain ϵ_{yy} curve for obtaining the constrained modulus ($\bar{E} = 4.062 \text{ MPa}$) for one of the configurations explored in experiments.